THE UNIVERSITY OF QUEENSLAND

AUSTRALIA

Newborn EEG connectivity analysis using time-frequency signal processing techniques

Amir Omidvarnia

Bachelor of Science (Biomedical Engineering),

Master of Science (Biomedical Engineering)

A thesis submitted for the degree of Doctor of Philosophy at

The University of Queensland in 2014

School of Medicine

Abstract

Scalp electroencephalography (EEG) monitoring in early life is providing vital assistance to clinical management during diagnosis and treatment of developing brain disorders. It is also a useful tool for predicting long-term neurological outcomes of perinatal injuries. Continuous evolution of cerebral structures during early brain maturation imposes salient changes in the temporal morphology of newborn EEG patterns. Therefore, dealing with neonatal EEG signals is technically very challenging. The current dominant approach to newborn EEG assessment is based on visual inspection of EEG recordings by an expert. This process is highly subjective and also, very time-consuming. More importantly, it requires a high level of expertise for appropriate interpretation. On the other hand, neonatal intensive care units (NICUs) in most countries do not have ready access to high-level EEG expertise. The development of automatic newborn EEG analysis systems is therefore vital to improve international newborn health.

This dissertation is focused on developing scalp EEG connectivity analysis methods for objective monitoring of newborn EEG signals. Three important characteristics of the signals are taken into consideration for the proposed methodologies: time-varying behavior, directional relationships between channels and frequency-specific fluctuations of amplitudes. It leads to a more comprehensive insight into the scalp-level electrical interactions between different cortical areas of the newborn brain in time and/or frequency domains. Two types of newborn brain abnormalities including seizures and intra-ventricular hemorrhage (IVH) and their impact on scalp EEG connectivity are investigated. Also, neonatal electric resting state networks (eRSNs) are characterized using EEG recordings of healthy fullterms, healthy preterms and preemies with IVH as well as a set of newborn functional magnetic resonance imaging (fMRI) datasets.

The first contribution of this research is a new time-frequency based approach for estimating the generalized phase synchrony (GePS) among multichannel newborn EEG signals using the linear relationships between their instantaneous frequency laws. Since the underlying signals are usually multicomponent, a decomposition method like multi-channel empirical mode decomposition is used to simultaneously decompose the multi-channel signals into their intrinsic mode functions (IMFs). The results confirm that the GePS value within EEG channels increases significantly during ictal periods. A statistically consistent phase coupling is also observed within the non-seizure segments supporting the concept of constant inter-hemispheric connectivity in the newborn brain during inter-ictal periods.

The second contribution is a time–frequency method for measuring directional interactions over time and frequency from scalp-recorded newborn EEG signals in a way that is less affected by volume conduction and amplitude scaling. The time-varying generalized partial directed coherence method is modified, by orthogonalization of the strictly causal multivariate autoregressive model coefficients, to minimize the effect of mutual sources. The novel measure, generalized orthogonalized PDC (gOPDC), is tested first using two simulated models with feature dimensions relevant to EEG activities. The method is then used for assessing event-related directional information flow from flash-evoked responses in neonatal EEG. For testing statistical significance of the findings, a thresholding procedure driven by baseline periods in the same EEG activity is followed. The results suggest that the gOPDC is able to remove common components akin to

volume conduction effect in the scalp EEG, [1] handles the potential challenge with different amplitude scaling within multichannel signals, and [1] can detect directed information flow within a sub-second time scale in nonstationary multichannel EEG datasets.

The third contribution is a novel RSN analysis framework for studying the presence of long-range spatial correlations in spontaneous brain activity of newborn cortex using scalp EEG recordings. The spatial correlations of EEG signal are found to follow a robust bimodality: during high amplitudes (high mode), the brain exhibits strong widespread correlations that disappear during low amplitudes (low mode). Moreover, a clear spatial structure with frontal and parieto-occipital sub-networks appears only towards term age. No temporal bimodality is observed in the fMRI recordings under the proposed analysis paradigm, suggesting that early EEG activity and fMRI signal reflect different mechanisms of spatial coordination. The results suggest that the early developing human brain exhibits intermittent long-range spatial connections that likely provide the endogenous guidance for early activity-dependent growth of brain networks.

In summary, the techniques proposed in this dissertation contribute to the field of digital signal processing with applications to newborn EEG connectivity analysis and computer-assisted neonatal brain abnormality assessment.

Declaration by author

This thesis is composed of my original work and contains no material previously published or written by another person except where due reference has been made in the text. I have clearly stated the contribution by others to jointly-authored works that I have included in my thesis.

I have also clearly stated the contribution of others to my thesis as a whole, including statistical assistance, survey design, data analysis, significant technical procedures, professional editorial advice, and any other original research work used or reported in my thesis. The content of my thesis is the result of work I have carried out since the commencement of my research higher degree candidature and does not include a substantial part of work that has been submitted to qualify for the award of any other degree or diploma in any university or other tertiary institution. I have clearly stated which parts of my thesis, if any, have been submitted to qualify for another award.

I acknowledge that an electronic copy of my thesis must be lodged with the University Library and, subject to the General Award Rules of The University of Queensland, immediately made available for research and study in accordance with the Copyright Act 1968.

I acknowledge that copyright of all material contained in my thesis resides with the copyright holder(s) of that material. Where appropriate I have obtained copyright permission from the copyright holder to reproduce material in this thesis.

Amir Hossein Omidvarnia

Brisbane, December 2013

Publications during candidature

Peer-reviewed Journal Articles

[1] **A. Omidvarnia**, G. Azemi, B. Boashash, J. O. Toole, P. Colditz, and S. Vanhatalo, "Measuring time-varying information flow in scalp EEG signals: orthogonalized partial directed coherence," ***IEEE Transactions on Biomedical Engineering***, 2013 [Epub ahead of print].

[2] **A. Omidvarnia**, P. Fransson, M. Metsäranta, and S. Vanhatalo, "Functional Bimodality in the Brain Networks of Preterm and Term Human Newborns," ***Cerebral Cortex***, 2013 [Epub ahead of print].

[3] **A. Omidvarnia**, G. Azemi, P. B. Colditz, and B. Boashash, "A time–frequency based approach for generalized phase synchrony assessment in nonstationary multivariate signals," ***Digital Signal Processing***, vol. 23, no. 3, pp. 780-790, 2013.

[4] **A. Omidvarnia**, G. Azemi, J. M. O. Toole, and B. Boashash, "Robust estimation of highly-varying nonlinear instantaneous frequency of monocomponent signals using a lower-order complex-time distribution," ***Signal Processing***, vol. 93, no. 11, pp. 3251-3260, 2013.

Conference Articles

[1] **A. Omidvarnia**, B. Boashash, G. Azemi, P. Colditz, and V. Vanhatalo, "Generalised phase synchrony within multivariate signals: an emerging concept in time-frequency analysis," in IEEE 37th International Conference on Acoustics, Speech, and Signal Processing Kyoto, Japan, 2012.

[2] **A. Omidvarnia**, M. Mesbah, M. S. Khlif, J. M. O'Toole, P. Colditz, and B. Boashash, "Kalman filter-based time-varying cortical connectivity analysis of newborn EEG" in IEEE 33th Annual International Conference of Engineering in Medicine and Biology Society (EMBS) Boston, US, 2011, pp. 1423-1426.

[3] **A. Omidvarnia**, G. Azemi, B. Boashash, J. M. O' Toole, P. Colditz, and S. Vanhatalo, "Orthogonalized Partial Directed Coherence for Functional Connectivity Analysis of Newborn EEG," ICONIP 2012, Part II, LNCS 7664, pp. 683–691, 2012.

[4] **A. Omidvarnia**, S. Vanhatalo, M. Mesbah, G. Azemi, P. Colditz, and B. Boashash, "Generalized Mean Phase Coherence for Asynchrony Abnormality Detection in Multichannel Newborn EEG," in IEEE 11th International Conference on Information Sciences, Signal Processing and their Applications (ISSPA), Montreal, Canada, 2012, pp. 274-279.

[5] **A. Omidvarnia**, M. Mesbah, J. M. O'Toole, P. Colditz, and B. Boashash, "Analysis of the time-varying cortical neural connectivity in the newborn EEG: A time-frequency approach," in 7th International Workshop on Systems, Signal Processing and their Applications (WOSSPA), Algeria, 2011, pp. 179-182.

Conference Abstract

[1] **A. Omidvarnia**, P. Fransson, M. Metsäranta, P. Colditz, and S. Vanhatalo, "Bimodal networking in the newborn brain," in the 22nd Annual Meeting of the Australian Society for Psychophysiology (ASP2012), Sydney, Australia, 2012 (winner of the Brain Sciences UNSW Award for the student abstract presentation).

Publications included in this thesis

Peer-reviewed Journal Articles

[1] **A. Omidvarnia**, G. Azemi, B. Boashash, J. O. Toole, P. Colditz, and S. Vanhatalo, "Measuring time-varying information flow in scalp EEG signals: orthogonalized partial directed coherence," ***IEEE Transactions on Biomedical Engineering***, 2013 [Epub ahead of print].

- Incorporated in Chapter 3.

Contributor	**Statement of contribution**
Amir Omidvarnia	- contributed to the concept and design of study, - performed the literature survey and analysis, - implemented the codes, - wrote the first drafts, - contributed to editing the manuscript.
Ghasem Azemi	- contributed to the concept, design of study and analysis, - significantly contributed to editing the manuscript.
Boualem Boashash	- provided digital signal processing insight, - reviewed the concept and methodology, - contributed to editing the manuscript.
John M. O' Toole	- contributed to the concept and design of study, - contributed to editing the manuscript.
Paul Colditz	- contributed to the concept, - contributed to editing the manuscript.
Sampsa Vanhatalo	- contributed to the concept, design of study and analysis, - significantly contributed to editing the manuscript.

[2] **A. Omidvarnia**, P. Fransson, M. Metsäranta, and S. Vanhatalo, "Functional Bimodality in the Brain Networks of Preterm and Term Human Newborns," ***Cerebral Cortex***, 2013 [Epub ahead of print].

- Incorporated in Chapter 4.

Contributor	**Statement of contribution**
Amir Omidvarnia	- contributed to the concept and design of study, - performed the analysis, - implemented the codes, - significantly contributed to writing the first drafts (particularly, wrote the technical parts), - contributed to editing the manuscript.
Peter Fransson	- contributed to the concept and analysis (in particular, fMRI time series analysis), - provided the fMRI datasets for analysis, - contributed to editing the manuscript.
Marjo Metsäranta	- contributed to data acquisition, - contributed to editing the manuscript.
Sampsa Vanhatalo	- contributed to the concept, design of study, and analysis, - wrote most of the first drafts, - contributed to editing the manuscript.

[3] **A. Omidvarnia**, G. Azemi, P. B. Colditz, and B. Boashash, "A time–frequency based approach for generalized phase synchrony assessment in nonstationary multivariate signals," ***Digital Signal Processing***, vol. 23, no. 3, pp. 780-790, 2013.

- Incorporated in Chapter 2.

Contributor	Statement of contribution
Amir Omidvarnia	- contributed to the concept and design of study, - performed the literature survey and analysis, - implemented the codes, - wrote the first drafts, - contributed to editing the manuscript.
Ghasem Azemi	- contributed to the concept, design of study and analysis, - significantly contributed to editing the manuscript.
Paul Colditz	- contributed to the concept, - contributed to editing the manuscript.
Boualem Boashash	- provided digital signal processing insight, - reviewed the concept and methodology, - contributed to editing the manuscript.

Conference Articles

[1] **A. Omidvarnia**, B. Boashash, G. Azemi, P. Colditz, and V. Vanhatalo, "Generalised phase synchrony within multivariate signals: an emerging concept in time-frequency analysis," in IEEE 37th International Conference on Acoustics, Speech, and Signal Processing Kyoto, Japan, 2012.

- Incorporated in Chapter 2.

Contributor	Statement of contribution
Amir Omidvarnia	- contributed to the concept and design of study, - performed the literature survey and analysis, - implemented the codes, - wrote the first drafts, - contributed to editing the manuscript.
Boualem Boashash	- provided digital signal processing insight, - reviewed the concept and methodology, - contributed to editing the manuscript.
Ghasem Azemi	- contributed to the concept, design of study and analysis, - significantly contributed to editing the manuscript.
Paul Colditz	- contributed to the concept, - contributed to editing the manuscript.
Sampsa Vanhatalo	- contributed to the concept, design of study and analysis, - contributed to editing the manuscript.

[2] **A. Omidvarnia**, M. Mesbah, M. S. Khlif, J. M. O'Toole, P. Colditz, and B. Boashash, "Kalman filter-based time-varying cortical connectivity analysis of newborn EEG" in IEEE 33th Annual International Conference of Engineering in Medicine and Biology Society (EMBS) Boston, US, 2011, pp. 1423-1426.

- Incorporated in Chapter 3.

Contributor	Statement of contribution
Amir Omidvarnia	- contributed to the concept and design of study, - performed the literature survey and analysis, - implemented the codes, - wrote the first drafts, - contributed to editing the manuscript.
Mostefa Mesbah	- contributed to the concept and design of study, - significantly contributed to editing the manuscript.
Mohamed S. Khlif	- contributed to the concept, - contributed to editing the manuscript.
John M. O' Toole	- contributed to the concept and design of study, - contributed to editing the manuscript.
Paul Colditz	- contributed to the concept, - contributed to editing the manuscript.
Boualem Boashash	- provided digital signal processing insight, - reviewed the concept and methodology, - contributed to editing the manuscript.

[3] **A. Omidvarnia**, G. Azemi, B. Boashash, J. M. O' Toole, P. Colditz, and S. Vanhatalo, "Orthogonalized Partial Directed Coherence for Functional Connectivity Analysis of Newborn EEG," ICONIP 2012, Part II, LNCS 7664, pp. 683–691, 2012.

- Incorporated in Chapter 3.

Contributor	Statement of contribution
Amir Omidvarnia	- contributed to the concept and design of study, - performed the literature survey and analysis, - implemented the codes, - wrote the first drafts, - contributed to editing the manuscript.
Ghasem Azemi	- contributed to the concept, design of study and analysis, - significantly contributed to editing the manuscript.
Boualem Boashash	- provided digital signal processing insight, - reviewed the concept and methodology, - contributed to editing the manuscript.
Paul Colditz	- contributed to the concept, - contributed to editing the manuscript.
Sampsa Vanhatalo	- contributed to the concept, design of study and analysis, - significantly contributed to editing the manuscript.

[4] **A. Omidvarnia**, S. Vanhatalo, M. Mesbah, G. Azemi, P. Colditz, and B. Boashash, "Generalized Mean Phase Coherence for Asynchrony Abnormality Detection in Multichannel Newborn EEG," in IEEE 11th International Conference on Information Sciences, Signal Processing and their Applications (ISSPA), Montreal, Canada, 2012, pp. 274-279.

- Incorporated in Chapter 2.

Contributor	Statement of contribution
Amir Omidvarnia	- contributed to the concept and design of study,

	- performed the literature survey and analysis, - implemented the codes, - wrote the first drafts, - contributed to editing the manuscript.
Sampsa Vanhatalo	- contributed to the concept, design of study and analysis, - contributed to editing the manuscript.
Mostefa Mesbah	- contributed to the concept and design of study, - contributed to editing the manuscript.
Ghasem Azemi	- contributed to the concept, design of study and analysis, - contributed to editing the manuscript.
Paul Colditz	- contributed to the concept, - contributed to editing the manuscript.
Boualem Boashash	- provided digital signal processing insight, - reviewed the concept and methodology, - contributed to editing the manuscript.

[5] **A. Omidvarnia**, M. Mesbah, J. M. O'Toole, P. Colditz, and B. Boashash, "Analysis of the time-varying cortical neural connectivity in the newborn EEG: A time-frequency approach," in 7th International Workshop on Systems, Signal Processing and their Applications (WOSSPA), Algeria, 2011, pp. 179-182.

- Incorporated in Chapter 3.

Contributor	**Statement of contribution**
Amir Omidvarnia	- contributed to the concept and design of study, - performed the literature survey and analysis, - implemented the codes, - wrote the first drafts, - contributed to editing the manuscript.
Mostefa Mesbah	- contributed to the concept and design of study, - significantly contributed to editing the manuscript.
John M. O' Toole	- contributed to the concept and design of study, - contributed to editing the manuscript.
Paul Colditz	- contributed to the concept, - contributed to editing the manuscript.
Boualem Boashash	- provided digital signal processing insight, - reviewed the concept and methodology, - contributed to editing the manuscript.

Conference Abstract

[1] **A. Omidvarnia**, P. Fransson, M. Metsäranta, P. Colditz, and S. Vanhatalo, "Bimodal networking in the newborn brain," in the 22nd Annual Meeting of the Australian Society for Psychophysiology (ASP2012), Sydney, Australia, 2012 (winner of the Brain Sciences UNSW Award for the student abstract presentation).

- Incorporated in Chapter 4.

Contributor	**Statement of contribution**
Amir Omidvarnia	- contributed to the concept and design of study, - performed the analysis, - implemented the codes, - wrote the first drafts, - contributed to editing the manuscript.
Peter Fransson	- contributed to the concept and analysis (in particular, the fMRI time series analysis), - contributed to editing the manuscript.
Marjo Metsäranta	- contributed to data acquisition, - contributed to editing the manuscript.
Paul Colditz	- contributed to the concept, - contributed to editing the manuscript.
Sampsa Vanhatalo	- contributed to the concept, design of study, and analysis, - significantly contributed to editing the manuscript.

Contributions by others to the thesis

The following researchers contributed to this thesis in terms of the concept and design of the studies; technical work; analysis and interpretation of the results; and drafting or significantly revising different parts of the research:

- Dr. Ghasem Azemi,
- Prof. Boualem Boashash,
- Prof. Paul Colditz,
- Dr. Peter Fransson,
- Dr. Mohamed S. Khlif,
- Dr. Mostefa Mesbah,
- Dr. Marjo Metsäranta,
- Dr. John M. O' Toole,
- Dr. Sampsa Vanhatalo.

Statement of parts of the thesis submitted to qualify for the award of another degree

None

Acknowledgements

It was not possible for me to accomplish this work without the guidance and immense knowledge of my advisory team members, help from friends and continuous support of my family.

I would like to extend my sincere appreciation to Prof. Paul Colditz and Prof. Boualem Boashash for providing me with the opportunity of doing this research at the Perinatal Research Centre, University of Queensland Centre for Clinical Research. Their constant academic support made this research possible. I gratefully acknowledge financial support from UQ School of Medicine for my PhD program through an International Postgraduate Research Scholarship and also, funding of the Qatar National Research Fund for medical research within our signal processing research group.

I sincerely thank Drs. Ghasem Azemi, Sampsa Vanhatalo, John O'Toole, and Mostefa Mesbah for their patience, enthusiasm, encouragement and insightful comments throughout the research project. Their tireless efforts in proofreading the drafts of my manuscripts and thesis, written in English as my non-native language, are deeply appreciated. They not only taught me valuable academic skills, but also the value of ethics and support in the research environment. I owe a debt of gratitude to Dr. Vanhatalo who opened the doors of brain research and EEG signal processing to me. I acknowledge the valuable help of Dr. Peter Fransson in providing fMRI datasets for my research along with a lot of practical comments and helpful discussions. I am grateful to Dr. Tracey Bjorkman, Prof. Michael Breakspear and Prof. Neil Bergmann who gave me their invaluable feedback during my three PhD milestones.

Many thanks to my fellow colleagues at UQ for academic support, fruitful discussions and all the good times we have had together in the last three and a half years: Maryam, Siamak, Shiying, Majid, Awal, Mohamed, Steph, Amanda and Maxine. Outside of the research environment, I would like to express my deepest gratitude to my precious friends in Australia who made a lot of memorable moments for me during my stay: Adam, Matt, Annie and Russell, Maggie and Mike, Butterfly Mike, Ann and Geoff, Anthea and Thong, Bob, Doug, Carol, Marie and Murray, to name but a few. My special thanks go to Helen and Noel Standfast who supported me unconditionally throughout my degree.

Last but not least, my warmest appreciation goes to my lovely wife, Kimia for her understanding, dedication and consideration, especially during times of stress associated with the thesis. I would also like to sincerely thank my parents in Iran for their lifelong support and tolerance during the years that I was away from home.

Keywords

electroencephalogram, time-frequency analysis, neonatal brain, directional connectivity, multivariate signal, resting state networks, brain abnormality, phase synchrony, volume conduction effect

Australian and New Zealand Standard Research Classifications (ANZSRC)

ANZSRC code: 090609, Signal Processing, 40%

ANZSRC code: 090399, Biomedical Engineering not elsewhere classified, 60%

Fields of Research (FoR) Classification

FoR code: 0906, Electrical and Electronic Engineering, 40%

FoR code: 0903, Biomedical Engineering, 60%

To my dear wife, ***Kimia*** *and our little son,* ***Kian***

Contents

List of Figures

List of Tables

Acronyms and abbreviations

3D	3 dimensional
AIC	akaike information criterion
AUC	area under curve
BAF	band amplitude fluctuation
BIC	bayesian information criterion
CTD	complex-time distribution
CWD	choi-williams distribution
dDTF	direct directed transfer function
DEKF	dual extended kalman filter
DTF	directed transfer function
EEG	electroencephalogram
EMD	empirical mode decomposition
FFT	fast fourier transform
FIR	finite impulse response
fMRI	functional magnetic resonance imaging
FNR	false negative rate
FPR	false positive rate
GCI	granger causality index
GePS	generalized phase synchrony
gOPDC	generalized orthogonalized partial directed coherence
gPDC	generalized partial directed coherence
Hz	hertz
IF	instantaneous frequency
IMF	intrinsic mode decomposition
IP	instantaneous phase
MBD	modified b-distribution
MEG	magnetoencephalogram
MPC	mean phase coherence

MVAR	multivariate autoregressive
NICU	neonatal intensive care unit
OPDC	orthogonalized partial directed coherence
PDC	partial directed coherence
PLV	phase locking value
PWVD	polynomial wigner-ville distribution
QTFD	quadratic time-frequency distribution
RBBDD	real base-band delay demodulator
RBWH	royal brisbane and women’s hospital
RID	reduced interference distribution
ROC	receiver operating characteristic
SNR	signal to noise ratio
SPEC	spectrogram
SSVEP	steady-state visual evoked potential
TF	time-frequency
TFD	time-frequency distribution
TFSA	time-frequency signal analysis
TNR	true negative rate
TPR	true positive rate
tv	time-varying
WVD	wigner-ville distribution

Chapter 1

Introduction

The human brain can be considered as a complicated structure with lots of networks dynamically interacting with each other. The situation gets even more sophisticated when it comes to the level of newborn brain development processes during which the brain is changing on a daily basis. An infant is born with billions of unconnected or sparsely neurons within the cortex which become gradually more connected, a process modulated through new sensory and emotional experiences. The ability of the brain to conduct high level sensory and cognitive functions will strongly depend on underlying interactions between different cortical areas. Surface electroencephalographic (EEG) signals, projections of cortical electrical activity on the scalp, reflect useful information about interrelations between cortical areas. Researchers and clinicians commonly use EEG to study normal functionality and/or abnormalities of the developing brain due to its non-invasive nature, high temporal resolution and low cost of the recordings [2-4].

Time-varying behavior of the early cortical networks is crucial for endogenous brain wiring at the developmental period (mainly last trimester of gestation), when the connections between cortical areas have not still been established by the exogenous stimuli [5, 6]. Therefore, a bimodal behavior can be observed in the electrical activity of these networks characterized by two alternating modes: the high mode associated with the self-organizing, locally generated spontaneous activity transients (SATs, also known as bursts) and the low mode representing low-amplitude intervals between SATs [7-11]. Newborn EEG bimodality gradually attenuates by becoming more mature with continuous activity from the preterm period to term age [10]. In addition, the characteristic cellular level network mechanisms underlying interactions within the healthy/unhealthy brain cortical areas in neonates differ from the ones seen in the more mature brain [12]. Some features of adult abnormal brain functionality may be normal features in the newborn and vice versa [13, 14].

The study of electrical and structural brain connectivity during the perinatal period has developed from a pure medical interest to pioneering research insights being provided by engineers, mathematicians and physicists. In fact, developing neural pathways within the immature brain can be characterized from different perspectives, each of which sheds light on a certain aspect of brain functionality. However, the dominant method of outcome assessment that relies on clinical assessment in neonatal brain clinical trials is still highly subjective, mainly because it suffers from the lack of rigorous quantitative descriptions for normal/abnormal cortical interrelations. This

shortcoming will be addressed throughout this thesis by incorporating a multitude of temporal, spectral and spatial scales obtained from different characteristics of newborn EEG signals.

In this dissertation, novel methodologies are developed for studying newborn brain functionality through scalp EEG connectivity analysis. The proposed methods account for three aspects of neonatal scalp EEG signals: (i) time-varying behavior, (ii) directional relationships between channels and (iii) frequency-specific fluctuations of amplitudes This approach leads to a more comprehensive insight into the electrical interactions between different cortical areas of the newborn brain extracted from time and/or frequency domains. In this way a narrow view on the problem of newborn EEG connectivity analysis and its different dimensions has been avoided. Studies of newborn EEG seizures and intra-ventricular hemorrhage (IVH) have been described using different connectivity analysis techniques. Neonatal electric resting state networks (eRSNs) have also been characterized using EEG recordings of healthy fullterm babies, healthy preterm babies and preterm babies with IVH and also with newborn functional magnetic resonance imaging (fMRI).

This chapter describes the background and rationale of the thesis which precedes a description of the significance, objectives and overall contributions of the work. It concludes with an outline of the whole thesis.

1.1 Background and rationale

1.1.1 Essential definitions

For the sake of clarity throughout this thesis, definitions of general concepts are given here, while the definitions of more specific concepts are provided within the relevant chapters:

Gestational age (GA – also known as menstrual age), usually expressed in weeks + days: the time difference between the first day of the last normal menstrual period and the day of delivery [15].

Conceptional age (CA): the time difference between the day of conception and the day of delivery [15]. When the CA is known, the GA is approximately calculated by adding 2 weeks to the CA [15].

Preterm baby: an infant born before 37 completed weeks of GA [16, 17].

Term baby: an infant born at 38-42 weeks GA[16].

Neonatal intensive care unit (NICU): an intensive care unit (ICU) with special equipment for caring of sick or preterm babies.

International 10-20 system: an internationally recognized standard which defines a universal arrangement procedure for EEG electrode placement over the scalp.

Cerebral cortex: the folded outer layer of the brain formed by gyri and sulci and composed of several lobes over two hemispheres. It is the predominant source of electrical activity that is then projected onto the scalp and recorded by EEG electrodes.

Scalp EEG: projection of the cortical electrical activities over the scalp which is non-invasively recorded by surface electrodes.

EEG Symmetry: spatial correspondence of EEG patterns on left and right hemispheres with respect to the sagittal plane.

EEG Synchrony: temporal coincidence of EEG patterns between channel recordings.

1.1.2 Newborn EEG connectivity analysis

Brain connectivity can be described as either functional connectivity or effective connectivity [18]. Functional connectivity is described as the "temporal correlations between remote neurophysiological events", whereas effective connectivity is defined as "the influence one neural system exerts over another" [18]. Consequently, measures of functional connectivity deal with the statistical directional/non-directional relationships of neurophysiological signals that include EEG, magnetoencephalography (MEG) and fMRI. In contrast, measures of effective connectivity quantify the interactions between neuronal systems. Investigating the dynamic characteristics of human brain connectivity is not as straightforward as the situation in anatomical studies where post-mortem tissues can be directly studied. In fact, a significant part of our knowledge about newborn and adult brain functionality originates from animal experiments [17]. However, non-invasive measurements of the human brain activities such as scalp EEG recordings and fMRI provide a rich source of information reflecting many important aspects of brain development.

EEG signals originate from ionic current flows within the cortex and include spatial averaging of electrical activity over cortical areas. It has been shown that long-range connections within the immature brain are developed much earlier than short-range cortico-cortical connections [17].

Therefore, unilateral autonomous cortical activity in the most preterm babies is dominant with no significant inter-hemispheric relationship observed at this stage [17]. However, expansion of new neuronal pathways through the corpus callosum, establishment of the thalamo-cortical loops and emergence of cortical gyri/sulci in the newborn brain imposes fundamental changes on the morphological characteristics of the EEG signal during the first months after birth [17].

Newborn EEG during early brain development shows a spontaneous, intermittent behavior resulting in a discontinuous ('trace discontinue' [19]) appearance with an alternating combination of bursts (a.k.a SATs [11]) and low voltage activity (usually referred to as 'inter-burst intervals') [20]. This pattern needs to be distinguished from EEG burst-suppression which is abnormal when observed in more mature infants where it is associated with major cerebral impairments [20]. Burst events arise from simultaneous firing of pyramidal neurons within neural networks of the developing cortex, when triggered by external sensory stimuli [17]. It leads to inter-connections between cortical areas through excitatory synapses. Thus the occurrence of SATs in the preterm brain can be directly related to newborn EEG connectivity during brain maturation.

SATs play an important role in the establishment of neuronal connections between immature brain areas [16]. The earliest SATs appear focally at the EEG electrodes over the sensory cortices at about 24 weeks GA, the earliest stage at which a preterm born baby is likely to survive in the NICU [17]. SATs become more widespread over the cortex as the newborn approaches full term. The discontinuous morphology of the EEG gradually becomes more continuous towards term age (from 25 to 40 weeks of GA) by merging more complex electrical activity patterns with higher amplitudes between SATs ('tracé alternant' [19]). Reduction of the SAT amplitudes during this period is probably associated with dispersion of the orientation of cortical electrical fields through the ongoing gyration process and expansion of the cortical areas with coherently active SATs [17]. Existence of distinctively high amplitude bursts in the signal at this stage may reflect brain dysfunction [17]. From this point of view, two concepts of newborn brain connectivity and abnormality can be linked through characterization of newborn EEG bursts and inter-burst intervals. Developing interconnections within the immature brain at about 30 weeks gestation causes a rough temporal co-occurrence of SATs between the two hemispheres. Inter-hemispheric synchrony then becomes more consistent and more localized as 35 weeks GA is approached [17]. Large thalamo-cortical and cortico-cortical networks are involved which may or may not be connected through the corpus callosum [17]. The presence, absence or synchronization of SATs in newborn multichannel EEG in preterm and term infants may lead to promising prognostic and diagnostic tool in the NICU.

A typical SAT waveform is characterized by a dominant low frequency envelope (0.1-0.5 Hz) combined with several higher frequency oscillations nested on it [17]. Although the majority of information obtained from EEG signals during early ages comes from the δ band, higher

frequencies can convey important aspects of rapid oscillations within the cortex. Also, higher spectral bands (β and γ) are represented more in later ages resulting in a dramatic decrease in the amplitude of SATs and distribution of the EEG power over a wider frequency span. Considering this multiband nature and the nonstationary behaviour of newborn EEG signals during brain development, time-frequency analysis techniques may be very useful in analyzing cortical interconnections in the neonatal brain [21, 22]. Reciprocal relationships between the frequency domain and phase domain allow useful information about unilateral/inter-hemispheric synchrony of SATs regardless of the difference between their amplitudes. Time-varying multivariate autoregressive (tv-MVAR) modeling has shown its applicability for connectivity analysis of biosignals in different signal domains. A MVAR process is able to represent interactions between EEG channels in the form of linear difference equations and allows the direction of information flow between channels including direct and indirect influences.

Some newborn brain abnormalities such as inter-hemispheric asymmetry/asynchrony are associated with a global change of connectivity patterns over scalp EEG channels. Pair-wise comparison of surface EEG recordings is a potential method to evaluate their inter-relationships. A bivariate measure, however, is unlikely to capture the key feature of abnormal newborn EEG connectivity characterized by a global disruption in multiple locations. By using the MVAR representation of EEG signals, not only can the direction of the information flow between channels be inferred, but also the direct or indirect influences detected.

The effect of volume conduction is important in connectivity analysis of scalp EEG because a given brain source is often reflected in several EEG channels leading to inaccurate results for EEG connectivity. This is particularly problematic with the MVAR-based connectivity measures that are sensitive to volume conduction effects. A potential solution is to perform the EEG/MEG connectivity analysis at the source level, although this would require sufficiently reliable source localization. Combining orthogonalization at the MVAR coefficients level and the imaginary part of coherence has the potential to reduce spurious co-variability, the common result of volume conduction effects.

Functional connectivity within resting-state networks (RSNs) has recently been established. RSNs, discovered by Biswal et al [23], are spatially long-range brain networks synchronized in time through low-frequency (<0.1 Hz) fluctuations of blood oxygen level-dependent (BOLD) signals, while subjects are apparently resting [24-26]. Numerous resting-state relationships can be detected between different cortical areas of the adult brain including the visual cortex, sensorimotor areas and auditory areas using fMRI signal analysis [27]. In other words, the brain during rest is not idle, but it conducts spontaneous, intrinsic activities – both endogenous and sensory driven - associated with human behavior [28, 29], pain [30, 31] and diseases [1, 32, 33]. In fact, large-scale RSNs are

developed across anatomically remote, but functionally integrated cortical regions [34, 35]. The emergence of RSNs is tightly linked to cortical and thalamo-cortical development in the newborn brain [10, 24, 36-38]. fMRI studies on sleeping human newborns, including preterm babies, have shown inter-hemispherically developing RSNs analogous to those seen in older subjects [24, 37, 38]. Investigation of the spanning RSNs within the newborn brain in the presence of neuronal deficits helps to understand the establishment of these networks during abnormal brain maturation processes.

1.2 Significance and motivation

The preterm birth rate has increased over the last two decades in Australia [39]. This trend is expected to be even higher based on the predictions of World Health Organization [40] and Australian Institute of Health and Welfare [41]. According to the Australian Government's authoritative information and statistics released in 2012, around 8% of newborns in Australia are born preterm each year and approximately 15% of babies are admitted to Neonatal Intensive Care Units (NICUs) [42]. Preterm birth is known to interrupt vital brain development processes, diminishing future cognitive abilities in babies [43]. Cortical brain regions associated with social and emotional processing are less developed in the preterm infants in contrast to fullterms at term equivalent age [43]. In addition, follow-up studies on adults have revealed that preterm babies are much more prone to bipolar disorder, depression and psychosis during their adulthood compared with full-term babies [44]. Therefore, design of early intervention tools for preterm babies is efficacious in controlling the occurrence of abnormal neurodevelopmental outcomes. It reveals the magnitude of studies on the developing brain cortical networks as infrastructure of cognition, language and other mental abilities.

This thesis is concentrated on advancing the field of newborn brain monitoring through scalp EEG connectivity analysis using time-frequency signal processing techniques. Significance of the work falls within two major categories:

A. **Significance of newborn scalp EEG monitoring**: assessment of scalp EEG early in life is useful for predicting long-term neurological consequences and in reducing the mortality/morbidity rate in more mature groups [45]. The current dominant approach to newborn EEG assessment is based on the visual inspection of the EEG recordings by an expert. This process can be very subjective, requires high levels of expertise and usually takes a lot of time (especially for long-length EEG recordings) [3]. Therefore, developing computer-assisted clinical tools in NICUs for continuous and objective monitoring of newborn EEG was another motivation for this research. Neonatal EEG seizures and IVH with respect to their impact on the

interactions between cortical areas were targeted in this thesis. Both these abnormalities are known to have significant effect on newborn well-being [46, 47]. Although the applicability of newborn EEG for seizure characterization has been well established, there is still disagreement on the usefulness of continuous EEG monitoring in treating IVH [47]. Therefore, the findings of this research on IVH and its relation to newborn EEG will address a significant research question.

A further challenge in studies of newborn scalp EEG connectivity analysis arises from volume conduction between brain and scalp through cerebrospinal fluid (CSF) and skull as well as the effect of mutual brain sources on scalp EEG recording where a given brain source activity is often reflected in several channels. Consequently, their similarity may be falsely perceived as 'connectivity' by the analysis paradigms. This is particularly problematic with the directional connectivity measures that are very sensitive to volume conduction effects. Moreover, the numerical problem associated with possibly different variances of signal amplitudes has to be taken into account. This thesis aims to develop novel measures for extracting partial and directed information flow between surface EEG electrodes in the presence of volume conduction and effect of mutual sources.

B. Significance of newborn brain connectivity analysis: interactions within early brain networks are of crucial importance for the survival of young neurons and their functional segregation [6, 9, 10]. Characterization of the cortical inter-relations through brain connectivity analysis methods sheds light on the mechanisms behind early brain wiring, before they are driven by sensory experiences. Fundamental aspects of immature brain functionality and their links to growing brain spatial networks can be effectively explored using the capacities of advanced signal processing and multivariate signal connectivity analysis techniques. Since human brain is a time-varying dynamical system, the potential of time-frequency analysis for solving neonatal brain-related research questions is considerable [3]. In contrast, the dominant approach to analyzing brain interrelations has relied on the simplifying assumption of stationarity. Hence, time-frequency analysis has the important capacity to address current limitations in this area of research [3]. For example, the classical partial directed coherence function on a multichannel newborn EEG signal shows a number of peaks at different frequencies representing spectral relationships between channels. But, it does not provide any clue about how these inter-dependencies behave over time. This type of information is highly significant for the neuroscience community when the time-varying cortical interactions are going to be investigated within the immature brain's evolving environment. Therefore, methodological development of

newborn EEG connectivity analysis tools in the T-F domain was the main motivation for this research.

Intermittent network activities within newborn RSNs are tightly linked to the system-level cortical connectivity during the normal/abnormal brain maturation process. This significant fact motivated us to also design a practical framework for studying newborn RSNs through scalp EEG signals.

The significance of the methodological approaches taken in this thesis extends beyond this PhD research topic. There are important potential applications to the field of brain source localization. For example, external stimuli (tactile, visual, olfactory etc) have specific effects with time-varying spectral behaviour on the pre-defined brain areas. Applying the algorithms proposed in the thesis in conjunction with brain source localization methods on subjects with known brain abnormalities such as epilepsy could lead to better understanding of brain defects.

1.3 The Aim and objectives

The main aim of this thesis is to define newborn EEG connectivity during the maturation process and in the presence of brain abnormalities using time-frequency signal processing techniques. This may enable early detection of the abnormal signatures in neonatal cortical activity and possibly the development of diagnostic/prognostic tools for clinical use in NICUs. The methods will be suitable for any type of EEG recordings for the purpose of investigating cortical connectivity at the scalp level. Considering the fundamental differences between mature and immature brains and skulls, EEG connectivity analysis methods applied to the study of the adult brain are unlikely to be suited to neonatal brain research.

The specific objectives of the research can be described as follows:

Objective 1: Develop multivariate EEG connectivity measures that take into consideration the time-varying nature of newborn cortical activities.

Objective 2: Study the impact of newborn brain abnormalities (seizures and IVH) on EEG connectivity patterns.

Objective 3: Investigate the capacity of scalp EEG recordings for neonatal RSN analysis with respect to fMRI time series analysis.

Objective 4: Characterize the behavior of neonatal RSNs during brain development.

Objective 5: Mitigate the confounding effect of volume conduction for scalp EEG connectivity analysis.

1.4 Proposed approach and methods

Figure 1.1 depicts the analytic pathways taken in this thesis. The approach is two-fold: directional analysis versus non-directional analysis. Both approaches take into account the nonstationary and multivariate nature of EEG signals. However, the former approach also accounts for the directional relationships within multichannel EEG signals. Three methodological contributions are made:

1. Measurement of tv-gOPDC in scalp EEG signals with respect to volume conduction effect:
   This is done by modifying the classical PDC measure by combining the idea of orthogonalization at the level of MVAR coefficients and taking the imaginary part of ordinary coherence. The capacity of the measure to reduce the effect of spatial smearing for surface EEG connectivity analysis is investigated and validated through simulations. Figure 3.2 (block diagram of the tv-gOPDC in Chapter 3) illustrates the block diagram of the tv-gOPDC method.

2. Evaluation of GePS in multivariate nonstationary signals based on the concept of cointegration and Granger causality:
   Cointegrating relationships between IP as well as IF laws of a multivariate nonstationary signal are investigated using the Johansen test. Simulations are conducted for performance evaluation of the proposed approach.

3. Correlation analysis of scalp EEG power envelopes (eRSN analysis):
   A framework (Figure 4.1 in Chapter 4) is designed to purify the true interactions between BAFs of newborn EEG signals through a non-uniform segmentation approach and extraction of the connectivity maps between EEG electrodes. Graph measures are then elicited from the maps and fed into various statistical tests.

The following applications are introduced for the proposed methods:

1. Application of the tv-gOPDC method to newborn steady-state visual evoked potential analysis,

2. Application of the GePS paradigm for newborn EEG seizure characterization,

3. Application of the proposed correlation analysis method for studying RSNs during the brain maturation process as well as in the presence of IVH in the preterm brain.

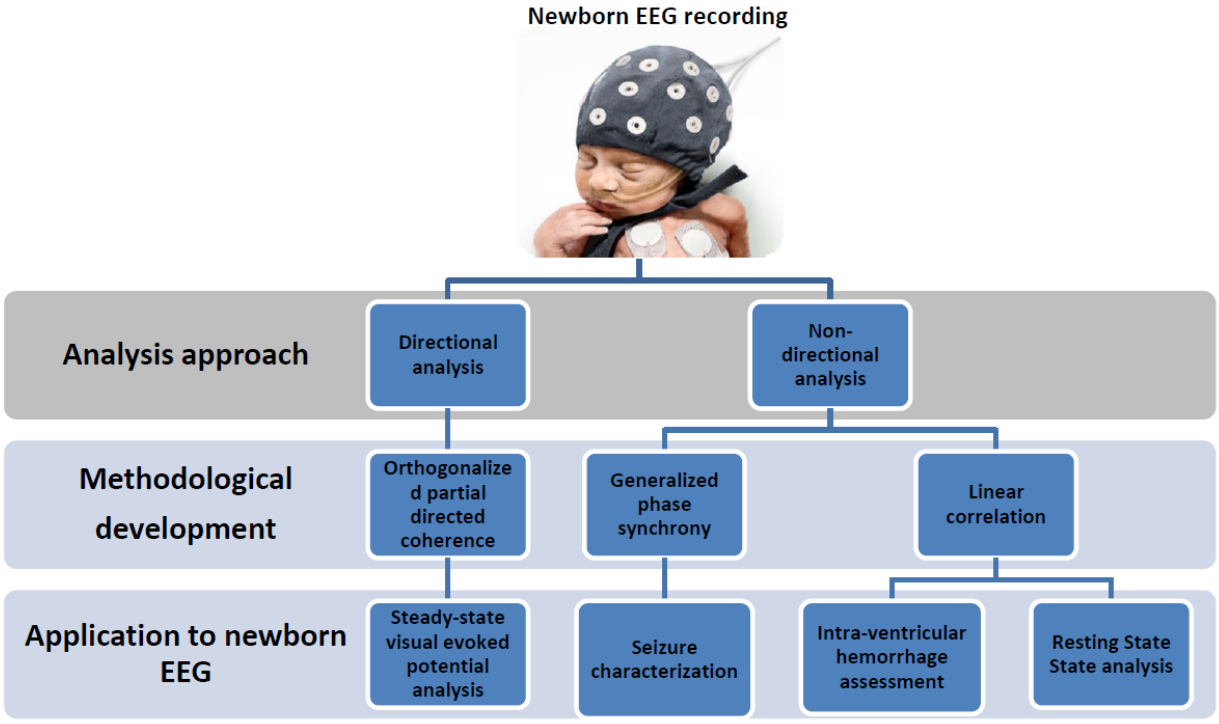

Figure 1.1: A schematic of the analysis pathways used in this thesis.

1.4.1 Contributions

Contributions of the thesis with regard to the research objectives in section 1.3 are listed below:

Objective 1: two time-frequency methods (generalized phase synchrony assessment and orthogonalized partial directed coherence) are proposed in Chapter 2 and Chapter 3 for analyzing the relationships between newborn scalp EEG channels by taking the time-varying characteristics of the signals into account. The former method describes an approach for GePS assessment within multivariate signals in the time-frequency domain. The latter method introduces a time-varying version of the classical PDC function which is able to extract pure correlation between neighboring EEG electrodes after mitigating the effect of mutual sources. The eRSN analysis approach developed in Chapter 4 has deliberately assumed stationarity for under-investigated BAF envelopes, as the fluctuations within the networks have a very slow frequency (>0.1 Hz).

Objective 2: Chapter 2 characterizes newborn EEG seizures by assessing generalized phase synchrony within multichannel EEG datasets. It is shown that GePS is significantly increased during seizures suggesting the capacity of this measurement for newborn EEG seizure characterization. Chapter 4 investigates the effect of IVH on the relationships between newborn EEG signals and studies the graph measures extracted from the affected neonatal eRSNs. The findings imply a significant difference between graph features between eRSNs of healthy preterms and preterms with IVH.

Objective 3: Chapter 4 reveals an important aspect of newborn EEG signals for RSN analysis which is not observed in fMRI time series. Newborn cortical electrical activity exhibits bimodal long-range spatial connections. But, no temporal bimodality is found in the fMRI recordings, suggesting that early EEG activity and fMRI signal reflect quite different mechanisms of spatial coordination.

Objective 4: Chapter 4 studies the dynamics of spontaneous brain activity in premature and fullterm babies with EEG and fMRI. The spatial correlations between scalp EEG channels follow a robust bimodality: during high amplitudes (high mode), the brain exhibits strong widespread correlations that disappear during low amplitudes (low mode). Moreover, a clear spatial structure with frontal and parietooccipital subnetworks appears only towards term age.

Objective 5: Chapter 3 presents an improvement for the classical partial directed coherence to deal with the volume conduction effect in newborn EEG and its application to directional connectivity analysis of neonatal steady-state visual evoked potentials. It is shown, using simulations and real EEG signals, that the proposed method intensifies true interactions between scalp EEG channels, whilst also suppressing spurious correlations due to the impact of mutual cortical sources on the surface electrical activity.

1.5 Thesis structure

This dissertation is organized as follows. Chapter 1 contains the significance, motivation and aims of the thesis and also briefly describes the neurophysiology of neonatal brain and newborn EEG as the realization of its cortical electrical activity. The next three chapters are associated with the methodology, innovations and comparisons of the approach to the problem of defining newborn brain connectivity at the scalp level. A relevant literature review has been provided within each of these chapters due to the multi-dimensional nature of this research.

Chapter 2 presents the proposed time-frequency EEG connectivity analysis for neonatal EEG abnormality assessment and its performance evaluation using simulations as well as newborn EEG seizure/non-seizure datasets. The concept of generalized phase synchrony within multivariate nonstationary signals is discussed in this chapter.

In Chapter 3, the suggested approach to extracting directional interactions between scalp EEG signals in the presence of volume conduction is reviewed and supported by simulations as well as estimates of newborn EEG signals.

Chapter 4 discusses bimodal functionality in the newborn EEG signals and its relation to the brain maturation process. Finally, the concluding remarks and suggestions for future work are given in Chapter 5.

Chapter 2

A T-F multivariate phase synchrony measure and its application to newborn EEG abnormality assessment[1]

2.1 Introduction

Phase synchrony has been used to investigate the dynamics of complex systems which result from time-varying interactions of several subsystems [48]. The human brain is such a complex system with different components interacting with each other dynamically. Therefore, studying the global coincidences within event-level EEG activities requires the use of multivariate phase synchrony measures which take the non-stationarity nature of EEG signals into account [49].

The concept of *analytic signals* [3, 50] or *complex Gabor wavelet filtering* [51] are usually utilized to extract the *instantaneous phase* (IP) of a real-valued signal. A measure of phase synchrony can then be computed from the resulting phase information [51]. Several methods were proposed for the evaluation of phase synchrony for bivariate and multivariate signals including *Mean Phase Coherence* (also, sometimes referred to as *Phase Locking Value*) [50, 51], *Evolution Map Approach* [52], *Instantaneous Period Approach* [53], *Mutual Prediction Approach* [53], *General Field Synchronization* [54], EMD-based methods [55, 56] and *frequency flows analysis* [57]. All of these methods are restricted by the assumption that the phase-locking ratio between signals is always rational. This restriction has been lately relaxed by proposing a generalized version using the concept of *cointegration* [58, 59] where the phase locking ratio is allowed to be irrational. Such generalization covers the classical definition as a special case, while it shares a broader view of phase interactions which can be observed in neuronal signals [59].

To overcome the limitations of the existing measures, this chapter proposes a novel approach for measuring phase synchrony within nonstationary multivariate signals. The approach is based on an interpretation of the generalized phase synchrony (GePS) using linear relationships between *instantaneous frequency* [60] and phase (IP) laws. The proposed method is evaluated by simulations as well as a multi-channel newborn EEG seizure/non-seizure database acquired from five subjects.

[1] This chapter is an extended version of the following publication: *A. Omidvarnia, G. Azemi, P. B. Colditz, and B. Boashash, "A time–frequency based approach for generalized phase synchrony assessment in nonstationary multivariate signals," Digital Signal Processing, vol. 23, no. 3, pp. 780-790, 2013.*

2.2 Time-frequency analysis and if estimation: a brief review

T-F signal processing allows signal analysis in both time and frequency domains simultaneously and is therefore an effective tool for dealing with nonstationary signals [3].

2.2.1 Quadratic TFDs

Dealing with non-stationary signals whose frequency content changes over time is a common situation in many engineering areas including biomedical signal processing [53, 61, 62], radar [63-65] and telecommunications [66, 67]. For the analysis of non-stationary signals, T-F distributions (TFDs) are the most suitable tools as they provide two-dimensional representations that reflect the time-varying spectral characteristics of the nonstationary signal and show how the energy of the signal is distributed over the two–dimensional T-F space. They also determine the number of signal components, the start and stop times and frequency range of an event in the signal. Quadratic TFDs (QTFDs) are the most commonly used TFDs and can be considered as smoothed versions of the Wigner-Ville Distribution (WVD) [3]. The discrete version of a QTFD with time-lag kernel $G[n,m]$ is given by [3]:

$$\rho_z[n,k] = 2\underset{m\to k}{DFT}\{G[n,m]\underset{n}{*}(z_s[n+m]z_s^*[n-m])\}, k = 1,\dots,M \tag{2.1}$$

where * denotes the complex conjugation, the symbol $\underset{n}{*}$ represents discrete convolution over time and $z_s[n]$ is the analytic associate of the real signal $s[n], n = 0,\dots,N-1$, i.e.:

$$z_s[n] = s[n] + j\mathcal{H}(s[n]) = a_z[n]e^{j\varphi_z[n]} \tag{2.2}$$

with $\mathcal{H}(.)$ being the Hilbert transform operator. The resulting $\rho_z[n,k]$ is an $M \times N$ matrix where M is the number of frequency bins. In (2.2), $a_z[n]$ and $\varphi_z[n]$ are respectively the *instantaneous amplitude* (IA) and IP of the signal. As RIDs have been shown to be efficient in the analysis and processing of EEG signals [60, 68, 69], three popular RIDs, spectrogram (SPEC), modified-B distribution (MBD) and Choi-Williams distribution (CWD), are used in this study for IF estimation [3]. Our selection is also based on the comparison of TFDs in [70] where SPEC, MBD and CWD are ranked within the first four high-resolution TFDs. Table 2.1 summarizes the discrete forms of the time-lag kernels and their parameters utilized in this study.

Table 2.1: Time-lag kernels of the TFDs and their parameters utilized in this study. The parameters N, L_w and L_{lag} denote the time length of the segment in samples, the window function length and the lag window length, respectively.

TFD	Discrete form of the time-lag kernel $G[n,m]$	Parameter(s)

SPEC	$w[n+m]w[n-m]$	Rectangular window w ($L_w = N/4$)
MBD	$\frac{cosh^{-2\beta}n}{\sum_{n=1}^{N} cosh^{-2\beta}n}$	$\beta = 0.01$, $L_{lag} = N/4$
CW	$\frac{\sqrt{\pi\sigma}}{2\lvert m\rvert} e^{-\frac{\pi^2\sigma n^2}{4m^2}}$	$\sigma = 10$, $L_{lag} = N/4$

2.2.2 Instantaneous frequency definition and estimation

The IF of a nonstationary signal shows how its frequency content changes over time. A signal may have one T-F component (called monocomponent signal) or multiple T-F components (called multicomponent signal). Following (2.2), the definition of IF of the real-valued signal $s[n]$, i.e. $f_z[n]$ is defined as the derivative of the signal's IP:

$$f_z[n] = F_s \frac{\varphi_z[n] - \varphi_z[n-1]}{2\pi} \tag{2.3}$$

where F_s is the sampling frequency. Several methods have been suggested to estimate the IF of monocomponent and/or multicomponent nonstationary signals [71-73]. Among these, the ones based on TFDs such as WVD [3], L-Wigner distribution [74], polynomial WVDs (PWVDs) [75] and complex-lag argument TFDs [76-78] have received a lot of attention, as they can disclose the multi-component nature of nonstationary signals.

2.2.2.1 Phase derivative of the analytic associate

The most straightforward way of extracting the IF is taking the derivative of the IP. To this end, the underlying signal is converted into its analytic associate using the Hilbert transform according to (2.2). Then, the phase angles are corrected using an unwrapping method to produce smoother IP traces. In this study, the MATLAB command *unwrap* was used to smooth the IP by adding multiples of $\pm 2\pi$ to the absolute jumps between successive points greater than or equal to π radians. Finally, the IF is obtained based on its original definition as the derivative of the IP given by (2.3).

2.2.2.2 TFD-based IF estimation

The first order moment of a digitized QTFD $\rho_z[n,k]$ with respect to frequency (aka the normalized linear moment IF estimator) is defined as [79]:

$$f_z[n] = \frac{F_s}{2M} \frac{\sum_{k=0}^{M-1} k\rho_z[n,k]}{\sum_{k=0}^{M-1} \rho_z[n,k]}. \quad (2.4)$$

Based on (2.4), $f_z[n]$ is the weighted mean frequency of the signal. In this study, three QTFDs were used for first order moment IF estimation: SPEC, MBD and CWD (see Table 2.1).

2.2.2.3 Real base-band delay demodulator (RBBDD)

For estimating the IF of the signal $z_s[n]$ in this method [80], it is first normalized, i.e.:

$$z_{sn}[n] = \frac{z_s[n]}{|z_s[n]|} = z_r[n] + jz_i[n]. \quad (2.5)$$

The block diagram depicted in Figure 2.1 is then used to extract the IF. The term $g[n]$ in the figure can be written as:

$$g[n] = sin(\varphi_z[n])cos(\varphi_z[n-1]) - sin(\varphi_z[n-1])cos(\varphi_z[n]) = sin(\varphi_z[n] - \varphi_z[n-1]) \quad (2.6)$$

which results in the estimated IF having the general form of (2.3). It is worth mentioning that although this approach results in the same estimation for the IF as the first derivative, it has the advantage of not requiring the computation of the IP of the signal which can be problematic.

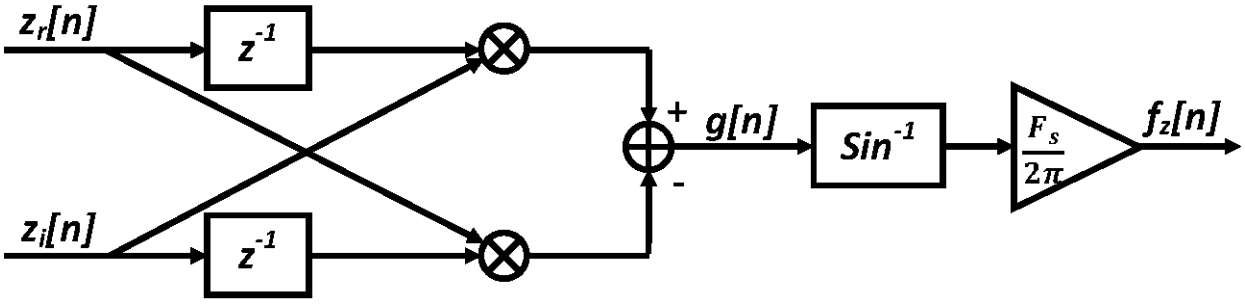

Figure 2.1: Block diagram of the real base-band delay demodulator

2.2.3 Monocomponent signals vs multicomponent signals: necessity of signal decomposition for IF estimation

In practice, the vast majority of real signals are multicomponent. In this case, $\varphi_z[n]$ in (2.2) will represent an ambiguous or meaningless weighted squared average of the phases corresponding to different components of the signal [57]. Therefore, the definition of IF in (2.3), based on the Hilbert transform, become useless [81]. Filtering in the frequency domain to isolate T-F components may lead to distortion of the constituent waveforms. Therefore, IF estimation of the nonstationary signals requires a separation of the T-F components prior to estimating the IFs [57]. Although there are other methods in the literature to deal with the multicomponent non-stationary signals (e.g, see [82, 83]), the EMD was adapted for decomposing the signals in the proposed approach. In contrast

to most existing methods, the EMD follows a fully data-driven scheme which does not need any a priori knowledge about the signal. The technique is an adaptive method which breaks down a nonstationary and nonlinear signal into its intrinsic mode functions (IMFs) [84]. Each IMF is a monocomponent signal which generates no interference in a QTFD [85]. In other words, the IMFs represent simple oscillatory modes with time-varying amplitude and frequency:

$$s[n] = \sum_{k=1}^{M} IMF_k[n] + r[n] \tag{2.7}$$

where $s[n]$ is a real-valued multicomponent signal with M components and $r[n]$ is the residue [81, 84]. By applying the Hilbert transform to (2.7), the analytic associate $z_s[n]$ can then be expressed as [81, 84]:

$$z_s[n] = \sum_{k=1}^{M} a_z^{(k)}[n] e^{j\varphi_z^{(k)}[n]} \tag{2.8}$$

where $a_z^{(k)}$ and $\varphi_z^{(k)}$ are respectively the IA and IP associated with the kth IMF. Each IMF of a nonstationary signal contains a limited frequency content of the original signal, as EMD acts basically as a dyadic filter bank [86]. It turns out that with adequate length, an IMF satisfies the assumption of an asymptotic signal. More details about the EMD process are given in Appendix **A**. Once the IMFs have been extracted, mono-component IF estimation techniques can be used to estimate the IF law of each component. In this study, the IF laws of monocomponent signals are estimated by taking the first order moments of three TFDs and also, by using a delay demodulator. The IF is also estimated according to (2.3). A detailed review of IF estimation algorithms can be found in [72, 73], while brief details are given below.

2.3 Formulation and assessment of generalized phase synchrony

2.3.1 Bivariate phase synchrony

Let $z_x[n]$ and $z_y[n]$ be the analytic associates of two one-dimensional stochastic real-valued signals $x[n]$ and $y[n]$, respectively; that is:

$$z_x[n] = x[n] + j\tilde{x}[n] = a_x[n] e^{j\varphi_x[n]} \tag{2.9}$$

$$z_y[n] = y[n] + j\tilde{y}[n] = a_y[n] e^{j\varphi_y[n]} \tag{2.10}$$

where $\tilde{x}[n]$ and $\tilde{y}[n]$ are the Hilbert transforms of $x[n]$ and $y[n]$, respectively. The original signals are assumed to be asymptotic signals [3]. The two signals $x[n]$ and $y[n]$ are said to be phase-locked of order $P_x : P_y$ if [50]:

$$\Delta\varphi_{x,y}[n] = P_x\varphi_x[n] - P_y\varphi_y[n] = const. \tag{2.11}$$

Such a strict condition is rarely satisfied for real-life signals. Therefore, this condition is often replaced with a more relaxed condition called phase entrainment condition expressed by [50]:

$$\left|P_x\varphi_x[n] - P_y\varphi_y[n]\right| < const. \tag{2.12}$$

The ratio P_x/P_y is assumed to be rational. In the case of discrete signals and for the case $P_x = P_y = 1$ (phase-locking of order 1:1), the phase synchrony measure is given by [50]:

$$R = \left|\frac{1}{N}\sum_{n=1}^{N-1} e^{j(\varphi_x[n]-\varphi_y[n])}\right| \tag{2.13}$$

where N is the length of the two signals in samples. The measure R is often referred to as mean phase coherence (MPC) or phase locking value (PLV) [50, 51]. The value R can be rewritten in a simpler form as:

$$R = \sqrt{\langle cos(\varphi_x - \varphi_y)\rangle^2 + \langle sin\,(\varphi_x - \varphi_y)\rangle^2}. \tag{2.14}$$

where < > represents the mean. R is restricted to the interval [0,1] where $R = 0$ reflects complete asynchrony and $R = 1$ implies a perfect synchrony between two signals.

2.3.2 Generalized phase synchrony (GePS)

The classical definition of phase synchrony for bivariate signals can be extended to multivariate signals using the concept of cointegration [87] using the following procedure.

2.3.2.1 Cointegration concept

A one-dimensional stochastic process is said to be *integrated of order d* ($I(d)$) if the reverse characteristic polynomial of its fitted multivariate autoregressive (MVAR) model has *d* roots on the unit circle in the z-complex plane [58]. The $I(d)$ process is unstable, but it can be converted into a stable one ($I(0)$) by *d* times differentiation [58]. Two or more integrated signals can be in a long-run relation with each other if there is a linear combination of these signals that results in a stationary process [58]. In such case, the underlying signals are called *cointegrated* signals with cointegration rank r. The parameter r represents the number of cointegrating relationships among the signals. Multivariate Johansen test can be used to determine the cointegration rank and cointegrating coefficients across multivariate integrated processes [58, 88]. For more details about the Johansen test, refer to Appendix **B**.

2.3.2.2 Phase synchrony assessment based on the cointegration concept

Two signals $x_1[n]$ and $x_2[n]$ are said to be in a generalized phase synchronous relationship if their phases satisfy the following condition [58, 59]:

$$\exists\, c_1, c_2 :\ c_1\varphi_1[n] + c_2\varphi_2[n] = e[n] \tag{2.15}$$

where $e[n]$ is a normally distributed stationary stochastic process with finite second order moment and c_1 and c_2 are real-valued numbers. The relation presented in (2.15) reflects a cointegrating relationship between two phase signals $\varphi_1[n]$ and $\varphi_2[n]$. Given $\varphi_x[n] = [\varphi_1[n],\ \ \ldots\ \ , \varphi_K[n]]$ as the multivariate phase signal associated with $x[n] = [x_1[n],\ \ \ldots\ \ , x_K[n]]^T$ a multivariate real-valued signal with K variables, such relationship can be generalized to a multivariate cointegrating relationship among K phase signals as follows:

$$\exists\, c_1, \ldots, c_k : c_1\varphi_1[n] + c_2\varphi_2[n] + \cdots + c_K\varphi_K[n] = e[n]. \tag{2.16}$$

The Hilbert transform is used to obtain the phase of each signal component $x_i[n]$ separately. If the multivariate IP signal $\varphi_x[n]$ is integrated of order r, there are r stationary linear relationships within $\varphi_x[n]$ and the signal $x[n]$ is said to be in generalized phase synchrony of rank r [58, 59]. A higher rank implies a larger number of phase signals are involved in relationships and therefore, higher synchrony within channels. Based on (2.16), cointegrating coefficients $c_1, \ldots, c_k$ and the cointegration rank r $(0 \le r \le K)$ are estimated using the multivariate Johansen test [88].

2.3.3 Proposed IF-Based generalized phase synchrony quantification

The phase angle $\varphi_z[n]$ in (2.2) usually exceeds the range $-\pi$ to π, which results in unpredicted $\pm 2\pi$ jumps between some consecutive phase values [89]. This problem is due to the stochastic nature of the sampled signal where the angular distance between two successive samples may be multiples of 2π. Although one may use the unwrapping methods to deal with the problem, the use of the IF laws of the signals is proposed in this chapter instead of their IPs to skip the issue. We take advantage of the direct relationship between the IP and the IF to extract the cointegrating relations within phase signals by simply differentiating (2.16) with respect to time. A measure is then defined to quantify the level of interaction.

2.3.3.1 Interpretation of the IF-based GePS

Suppose $x[n]$ and $y[n]$ are two periodic signals, phase-locked of order $P_x : P_y$ where both P_x and P_y are integers. Let the two signals start from a similar point on the time axis. If the phase-locking ratio is rational, it implies that the two signals will cross each other periodically at the same initial

common value and this period is related to the least common multiple (LCM) between P_x and P_y. Therefore, the rational phase-locking order is associated with an intuitive physical meaning for periodic signals. In contrast, the two periodic signals never reach the same point with passing time in the case of irrational P_x/P_y.

Explanation of phase synchrony for non-periodic signals is not such straightforward. It becomes even more difficult for nonstationary signals which by definition cannot be periodic. In this case, the concept of frequency flows [57] in the T-F domain may help to clarify the issue. The notion of phase synchrony in (2.12) is strictly equivalent to the concept of frequency synchrony through the following formulation [57]:

$$\Delta\varphi_{x,y}[n] = P_x\varphi_x[n] - P_y\varphi_y[n] \approx const \tag{2.17}$$

which leads to

$$\frac{1}{2\pi} diff(\Delta\varphi_{x,y}[n]) = \frac{P_x}{2\pi} diff(\varphi_x[n]) - \frac{P_y}{2\pi} diff(\varphi_y[n]) = P_x f_x[n] - P_y f_y[n] \approx 0 \tag{2.18}$$

$$f_x[n] \approx \frac{P_y}{P_x} f_y[n]$$

This means that the two signals have similar IF shapes. The condition becomes equality when $P_x = P_y$. From this perspective, the concepts of phase synchrony and IF are connected [3, 57]. If two signals have similar IF laws during a time interval, they are phase-locked of order 1:1 over that time period [57]. Consequently, a linear relationship between two IFs with rational gain (P_x/P_y) implies phase-locking of order $P_x{:}\,P_y$. Such a definition cannot explain GePS in the case where the linear relationships between phase signals can be irrational. Therefore, the following interpretation is proposed for generalized phase synchronization based on the concept of cointegration [59]:

For a multi-channel nonstationary signal, if there is a linear relationship between the IF laws of a subgroup of channels during a reasonably long time period, they are said to be generally phase synchronized over that time period.

In this case, there is no reason for the coefficients to be integer as the notion of phase-locked may not in general apply. Figure 2.2 illustrates an example of GePS within the IFs of three channels. As the figure shows, there is *a linear relationship* (see the shadowed area) for all three IF laws during the shadowed time interval. Such linear combination defines a generalized phase-locking between channels. Note that the new explanation reduces to the classical definition of phase synchrony for rational phase-locking orders.

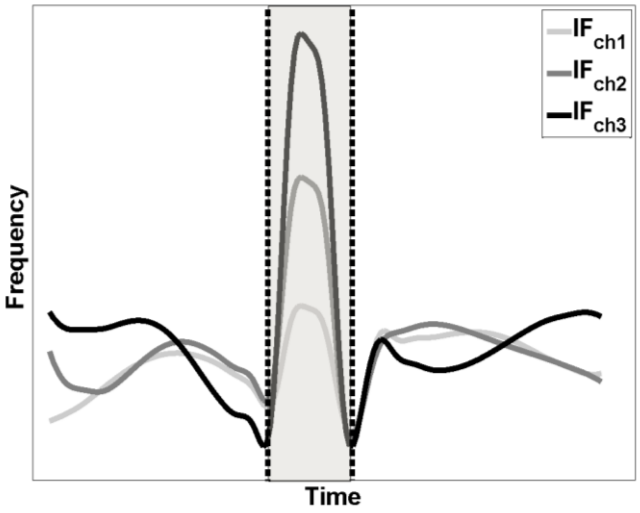

Figure 2.2: An example of generalized phase synchrony within a three-channel signal (curves show IF ridges in the T-F domain. Shadowed area illustrates the phase-locking time period).

2.3.3.2 Implementation of the proposed approach

The proposed procedure of GePS assessment for a nonstationary K-dimensional signal $x[n]$ is fully described by the following steps:

1. Each channel $x_i[n]$ $(i = 1, \dots, K)$ is decomposed into Q IMFs $g_{x_i}^{(q)}[n]$ $(q = 1, \dots, Q)$ using the EMD. The parameter Q can be estimated by the EMD stoppage criteria [81] as $Q = min_i\, Q_i$ $(i = 1, \dots, K)$ where Q_i is the number of IMFs in the ith channel. It is, then, kept the same for all channels.

2. The analytic associate of each IMF for the ith channel is obtained using the Hilbert transform, $z_i^{(q)}[n] = g_{x_i}^{(q)}[n] + j\mathcal{H}(g_{x_i}^{(q)}[n])$ and its IP is extracted, $\varphi_{z_i}^{(q)}[n] = \measuredangle(\frac{\mathcal{H}(g_{x_i}^{(q)}[n]}{g_{x_i}^{(q)}[n]})$. The phases $\varphi_{z_i}^{(q)}[n]$ are then corrected using an unwrapping method [89] to suppress phase angle jumps between consecutive elements and produce smoother phase traces. The IF $f_{z_i}^{(q)}[n]$ are then extracted by taking the derivative of the unwrapped phase signals $\varphi_{z_i}^{(q)}[n]$. The IF $f_{z_i}^{(q)}[n]$ may also be estimated using other IF estimates that bypass the problem of phase ambiguity (see section 2.2).

3. IFs of all channels at each decomposition level $f_z{}^{(q)} = [f_{z_1}^{(q)}, \dots, f_{z_K}^{(q)}]$ are divided into non-overlapping time segments with adequate length. The minimum window length is determined

based on the requirement of the MVAR parameter estimation where the length should be significantly larger than $K^2 p$ (p is the MVAR model order in the Johansen test) [90].

4. The Johansen method (maximum eigenvalues test) [58, 88] is applied on each multivariate segment at the 99% confidence level and the linear relationships between IFs are extracted as follows:

$$\begin{cases} c_{11} f_{z_1}^{(q)}[n] + c_{12} f_{z_2}^{(q)}[n] + \cdots + c_{1K} f_{z_K}^{(q)}[n] = e_1^{(q)}[n] \\ c_{21} f_{z_1}^{(q)}[n] + c_{22} f_{z_2}^{(q)}[n] + \cdots + c_{2K} f_{z_K}^{(q)}[n] = e_2^{(q)}[n] \\ \vdots \\ c_{r^{(q)}1} f_{z_1}^{(q)}[n] + c_{r^{(q)}2} f_{z_2}^{(q)}[n] + \cdots + c_{r^{(q)}K} f_{z_K}^{(q)}[n] = e_{r^{(q)}}^{(q)}[n] \end{cases} \quad (2.19)$$

5. where $f_{z_i}^{(q)}[n]$ represents the ith segmented IF ($i = 1, \dots, K$) of the qth IMF ($q = 1, \dots, Q$), $r^{(q)}$ ($0 \le r^{(q)} \le K$) is the number of cointegrating relationships within the multivariate segment, c_{ki} ($k = 1, \dots, r^{(q)}$) is the kth cointegrating coefficient of $f_{z_i}^{(q)}[n]$ and $e_k^{(q)}[n]$ is the stationary residual of the kth cointegrating relationship at the qth IMF.

6. The phase synchrony measure for each segment is defined as the normalized number of the cointegrating relationships $r^{(q)}$ over the IMF components:

$$\eta_{IF}{}^{seg} = \frac{1}{Q.K} \sum_{q=1}^{Q} r^{(q)}. \quad (2.20)$$

This measure always takes values between zero and 1 where zero means no cointegrating relationship within IF laws and 1 implies complete phase locking within the multivariate segment. The cointegrating relations can also be investigated among the phase signals directly. In this case, steps 3-5 are repeated for the multichannel IP signal $\boldsymbol{\varphi}^{(q)}[n]$ leading to another measure $\eta_{IP}{}^{seg}$ with similar definition of (2.20) in which $r^{(q)}$ accounts for the number of cointegrating relationships between phases at the q^{th} decomposition level.

2.3.3.3 Statistical analysis

The proposed method performance is evaluated using the receiver operating characteristic [91] curve to determine sensitivity and specificity. Suppose the multivariate signal $x[n]$ is divided into N segments with $N_{synch} \le N$ segments present generalized phase synchrony. True positive rate (TPR), true negative rate (TNR), false positive rate (FPR) and false negative rate (FNR) of the method are defined as:

$$TPR = \frac{No\ of\ segments\ correctly\ marked\ as\ synchronized}{N_{synch}},$$

$$TNR = \frac{No\ of\ segments\ correctly\ marked\ as\ asynchronized}{N - N_{synch}},$$

$$FPR = \frac{No\ of\ segments\ incorrectly\ marked\ as\ synchronized}{N_{synch}},$$

$$FNR = \frac{No\ of\ segments\ incorrectly\ marked\ as\ asynchronized}{N - N_{synch}}.$$

The sensitivity and specificity of the method are then defined as follows:

$$Sensitivity = \frac{TPR}{TPR + FNR}$$

$$Specificity = \frac{TNR}{TNR + FPR}.$$

The ROC curve is obtained by plotting the sensitivity versus (1-specificity). The curve allows calculating the optimum threshold based on its area under curve.

2.4 Results and Discussion

This section evaluates the IF-based generalized phase synchrony assessment framework on both simulated and real newborn EEG signals. At the beginning, the GePS measure is tried on the Kuramoto model without incorporating EMD (step 1 of the procedure), as the model outputs have narrow frequency contents. Then, the entire procedure is applied on a more relevant simulated signal as well as the newborn EEG datasets using different IF estimation methods.

2.4.1 Simulations

2.4.1.1 The Kuramoto model

The *kuramoto model* is a mathematical model of collective synchronization among a population of weak oscillators locked to a common frequency [92]. Realizations of this model in real-world systems are ranging from neural networks of the brain to arrays of lasers [92]. Due to the usefulness of this model for quantifying the synchronization within coupled oscillators (similar to what is observed within the cortex), it is used here to evaluate the performance of generalized phase synchrony framework.

The model represents pair-wise phase relationships among a population of N oscillators:

$$\dot{\theta}_i(t) = \omega_i + \frac{K}{N}\sum_{j=1}^{N} sin\big(\theta_j(t) - \theta_i(t)\big), \qquad i = 1, \dots, N \tag{2.21}$$

where N is the number of oscillators, $K \geq 0$ is the coupling strength, and θ_i, $\frac{\dot{\theta}_i}{2\pi}$ and ω_i are the IP, the IF and intrinsic natural frequency of oscillator i, respectively. The angular frequencies ω_i belong to a unimodal and symmetric distribution about a mean frequency Ω. Also, the coefficient $\frac{1}{\mathrm{N}}$ in (2.21) guarantees a stable behavior for the model as N approaches infinity [92].

To quantify the macroscopic characteristics of the Kuramoto model, a complex value $r(t)e^{i\psi(t)}$ is defined as the collective phase congruency of the network [92]:

$$r(t)e^{i\psi(t)} = \frac{1}{N}\sum_{j=1}^{N} e^{i\theta_j(t)} \tag{2.22}$$

where $r(t)$ is a measure of global phase coherence within the population and $\psi(t)$ represents the average phase. The coherence r is limited to the interval [0 1] where $r \approx 0$ reflects complete asynchrony and $r \approx 1$ implies a perfect synchrony between two oscillators. Combination of (2.21) and (2.22) leads to another form of the Kuramoto model revealing its mean-field character [92]:

$$\dot{\theta}_i(t) = \omega_i + Kr(t)\,sin\big(\psi(t) - \theta_i(t)\big), \qquad i = 1, \dots, N. \tag{2.23}$$

2.4.1.2 GePS assessment using the Kuramoto model

The Kuramoto model was simulated for $N = 10$ oscillators over a time span of 50 s and 20 ms step size ($F_s = 50\ Hz$). The GePS measures η_{IF} and η_{IP} in (2.20) were then extracted from the simulated model through the Monte-Carlo method with 50 iterations. For each run, the natural frequencies ω_i were randomly selected from a Gaussian distribution of mean zero and variance of 0.1 rad. The coupling coefficient K was varied from 0 to 2 with 0.1 steps to ensure that it exceeds its critical value [92]. Also, the MVAR model order for both measures was set to 10. Figure 2.3 depicts temporal evolutions and final phases of a population of 10 oscillators at three different coupling coefficients as well as the performance of the measures on the simulated signals. As the figure suggests, both measures are able to follow a similar pattern with $r(t)$ during the synchronization process of the model. However, the IF-based measure η_{IF} is more accurate for strong coupling, a situation which is commonly observed among EEG channels during seizure. Therefore, η_{IF} was finally utilized for newborn seizure EEG analysis in the next stage.

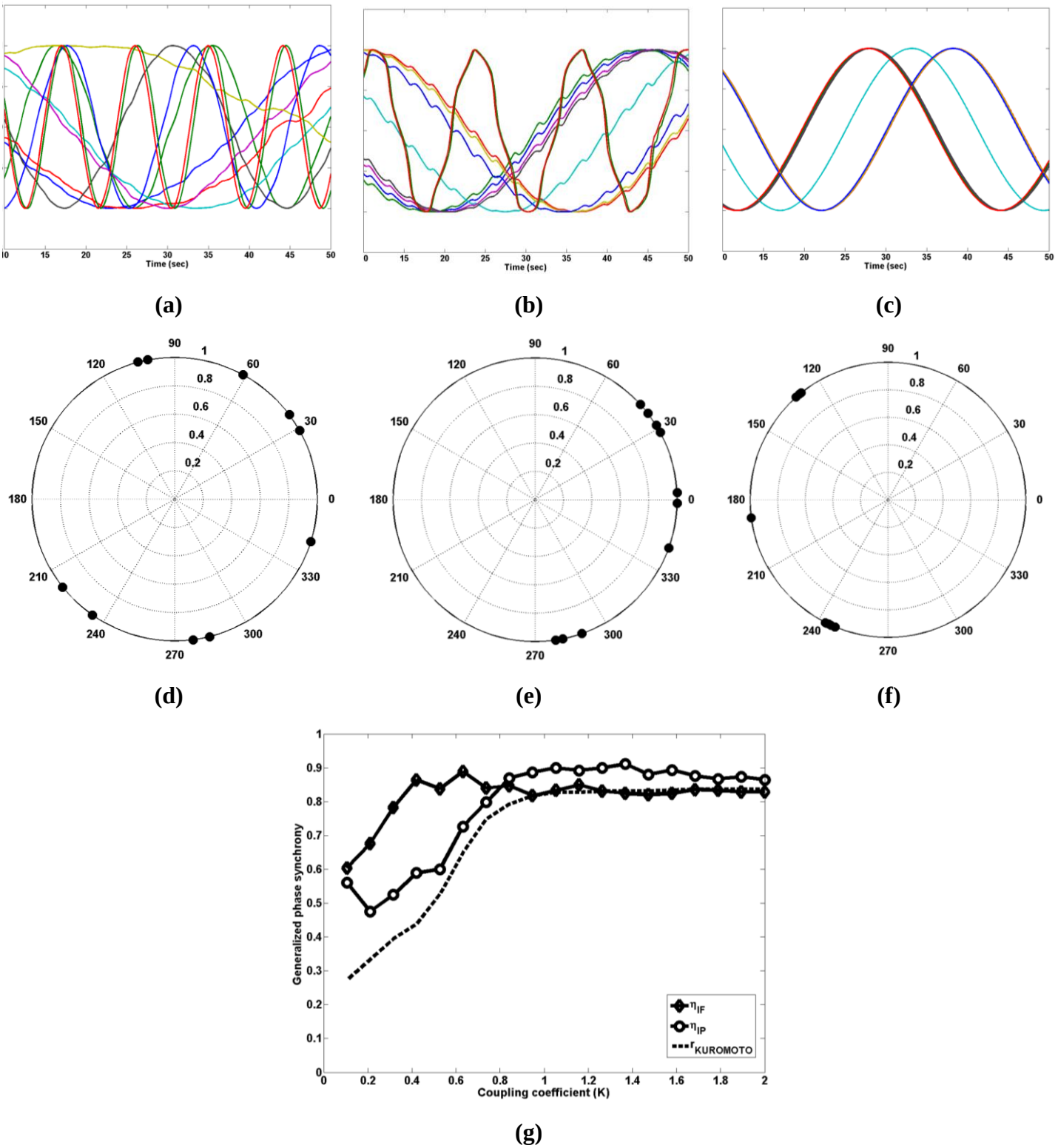

Figure 2.3: Simulation results for the Kuramoto model with 10 oscillators over a weak to strong coupling procedure.

Top row (a-c) illustrates temporal evolutions of three oscillators at $K = 0.2$, $K = 0.6$ and $K = 1$. Middle row (d-f) shows the final phases of the aforementioned oscillators at $t = 50\ s$. (g) depicts the global phase coherence $r(t)$ of the oscillators along with the two GePS measures η_{IF} and η_{IP} extracted from them using RBBDD (see sections 2.2.2 and 2.3.3).

2.4.1.3 GePS assessment with an integrated signal

In order to evaluate the performance of the proposed approach with different IF estimators for the nonstationary multivariate case, two 4-channel nonstationary signals with a length of 1000 seconds and unit amplitude at the sampling frequency of 100 Hz were simulated. For the asynchronous signal, the phase $\varphi_i[n]$ of each channel i was defined as an integrated process of order two. The phase $\varphi_i[n]$ was therefore obtained as the output of a linear shift-invariant system whose impulse response has two poles on the z-plane unit circle:

$$H(z) = \frac{1}{(1 - z^{-1})^2} \tag{2.24}$$

driven by a white noise process $w[n]$. The discrete form of the process in the time domain is therefore given by:

$$\begin{gathered} \varphi_i[n] = 2\varphi_i[n-1] - \varphi_i[n-2] + w[n], \\ 1 \le i \le 4, n = 1, \dots, L \end{gathered} \tag{2.25}$$

where, $L = 100000$ samples and $\varphi_i[1] = \varphi_i[2] = 0$. It implies that the IF laws are integrated processes of order one (one pole on the z-plane unit circle – random walk). In other words, there is no cointegrating relationship within the IFs or equivalently, no generalized phase synchrony within the channels. The asynchronous signal x^{asynch} was then defined as:

$$x^{asynch}[n] = real\{e^{j\varphi[n]}\}. \tag{2.26}$$

where $\varphi[n] = [\varphi_1[n], \quad \dots \quad , \varphi_4[n]]$. A perfectly synchronous 4-channel signal with the same form of (2.26) was also simulated with random walk phase signals:

$$\begin{gathered} \varphi_i[n] = \varphi_i[n-1] + w[n], \\ 1 \le i \le 4, n = 1, \dots, L \end{gathered} \tag{2.27}$$

where $\varphi_i[1] = 0$. It yields IFs with stationary trends with four cointegrating relationships. Both signals were divided into 4-sec segments and 100 segments were drawn out of the pool for each condition (synchrony/asynchrony). The dynamics of all phase signals was slowed artificially by a moving average process with the span of one second to magnify slow drift of the mean phase. Since the simulated signals are composed of multiple random frequency components, generalized phase synchrony can be observed within different intrinsic mode functions. Therefore, as described in Appendix **A**, an EMD sifting process was initially applied to decompose each channel of the segments into 5 IMFs. The proposed GePS measure was then extracted from the segments at each IMF, namely, 5 measures for each segment. The final measure for the segment was obtained by taking the average over 5 values. The MVAR model order for the Johansen test was set to 10 during the process.

Four IF estimation methods (RBBDD, SPEC, MBD and CWD – see section 2.2.2), along with the classical procedure of obtaining IF laws as the unwrapped phase derivative, were applied on the decomposed synchronous and asynchronous simulated signals. Figure 2.4 illustrates the ROC curves of the synchrony/asynchrony detection method associated with the IF estimators.

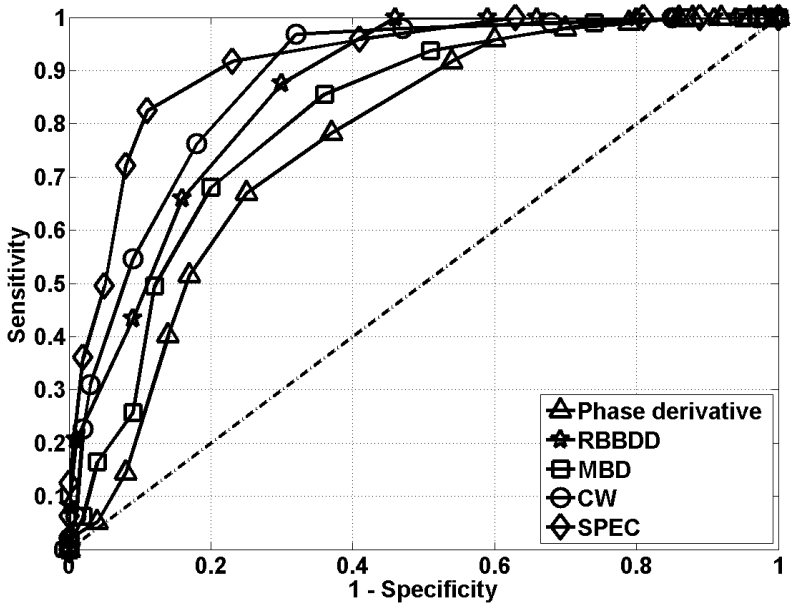

Figure 2.4: ROC curves of the IF estimation methods used in this chapter to extract generalized phase synchrony within the simulated signals.

In order to gain more insight into the performance of the IF estimators, the areas under the curve (AUCs) were computed for the ROC curves on the simulated signals. Table 2.2 summarizes the AUC of the ROC plots in Figure 2.4. As the results suggest, the CWD- and SPEC-based IF estimators showed the highest discrimination rate for estimating the GePS measure from the simulated signals.

Table 2.2: Area under curve for the ROC plots of Figure 2.4

IF estimator	**AUC (%)**
Phase derivative	79
RBBDD	85
CWD	88
MBD	82
SPEC	92

The next section presents the GePS assessment with neonatal EEG signals in the presence and absence of seizure.

2.4.2 Newborn EEG analysis

2.4.2.1 Datasets, preprocessing and segmentation

Eight monopolar channels (F_3, F_4, C_3, C_4, P_3, P_4, O_1 and O_2) out of 14 channels recorded using the 10-20 standard [93] were selected from the EEG datasets of five newborns. Figure 2.5 illustrates the arrangement of the electrodes. These electrodes were chosen according to the symmetrical combination of electrodes from left and right hemispheres in order to enable inter-hemispheric phase synchrony assessment. The data was recorded using a Medelec Profile system (Medelec, Oxford Instruments, Old Woking, UK) at 256 Hz sampling rate and marked for seizure by a pediatric neurologist from the Royal Children's Hospital, Brisbane, Australia. All signals were bandpass filtered within 0.5-30 Hz using a FIR filter of order 100. The filtered signals were inspected visually to remove highly artifactual segments. Artifact free intervals were then segmented into 4-sec windows. In this thesis, 100 non-overlapping ictal segments and 100 non-overlapping interictal segments were extracted randomly from 27 min of artifact-free seizure signals and 39 min of artifact-free nonseizure signals obtained from 5 subjects. The window length (1024 samples) was chosen to be larger than K^2p where p is the MVAR model order for the Johansen test (here, $p \leq 6$) and K is the number of channels (here, $K = 8$) [90].

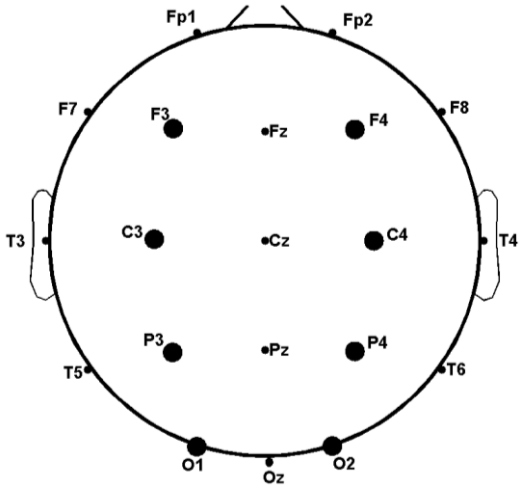

Figure 2.5: arrangement of the electrodes. Large circles illustrate the utilized electrodes.

2.4.2.2 Significant increment of the GePS measure during the seizure periods

The procedure described in section 2.3 was applied on each 8-channel (4 left and 4 right) newborn EEG segment in order to analyze the generalized phase synchronization within both seizure and non-seizure groups. Figure 2.6 illustrates the Modified-B distributions ($\beta = 0.01$, $L_{lag} = N/4$) and time traces of 5 IMFs extracted from 2 adjacent left-right electrodes (F3 and F4) for a random

seizure segment. The IFs of each multi-channel segment at each decomposition level (each IMF) are analyzed by the Johansen test. The cointegration ranks of the IMFs are then utilized for calculating the GePS measure of the underlying segment using (2.20). A vertical frequency shift can be observed between each two successive rows in Figure 2.6. This observation reflects the nature of the EMD sifting process as a dyadic filter bank [86]. As the figure suggests, the IMFs can be roughly linked to the EEG frequency bands: IMF5 covers the δ band (up to 5 Hz), IMF4 covers the δ and θ bands (up to 10 Hz), IMF3 mostly covers the θ and α bands (5-15 Hz), IMF2 mostly covers the α and β bands (10-20 Hz) and IMF1 mostly covers the β and γ bands (above 20 Hz).

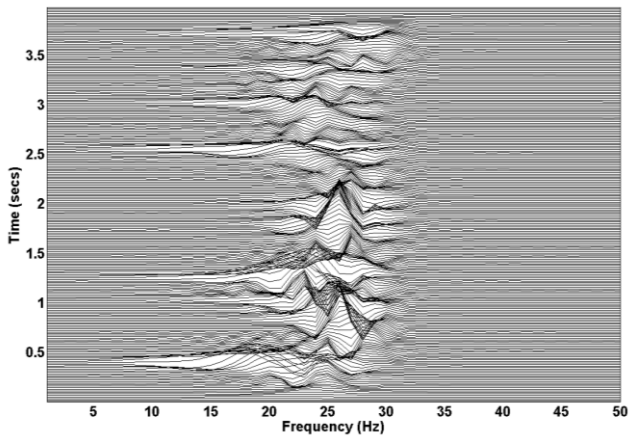

(a) IMF_1 extracted from F_3

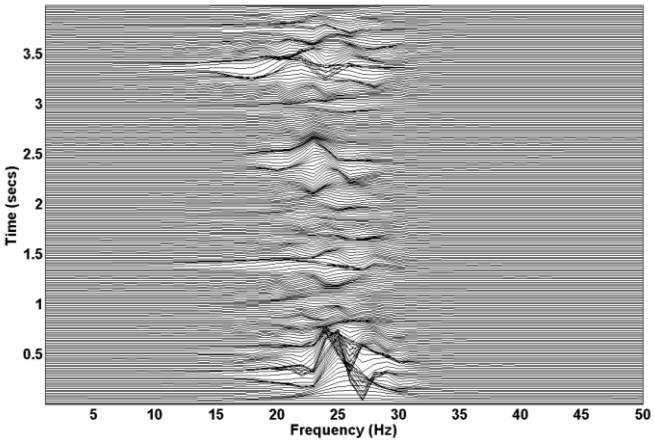

(b) IMF_1 extracted from F_4

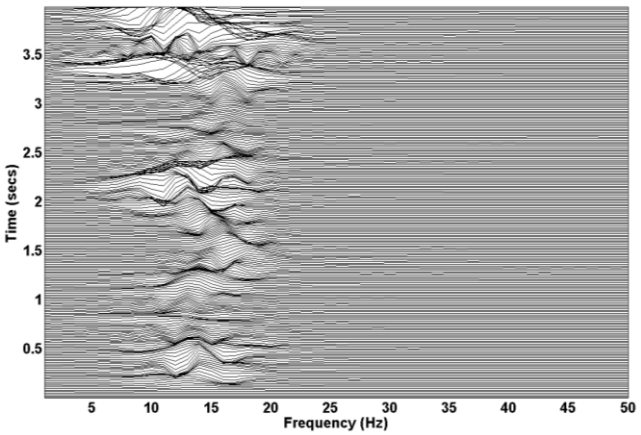

(c) IMF_2 extracted from F_3

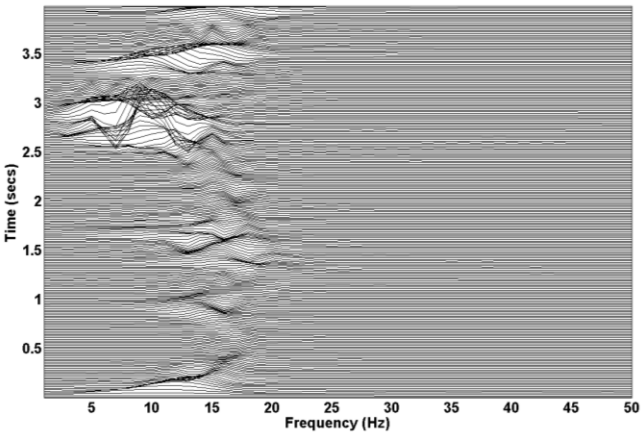

(d) IMF_2 extracted from F_4

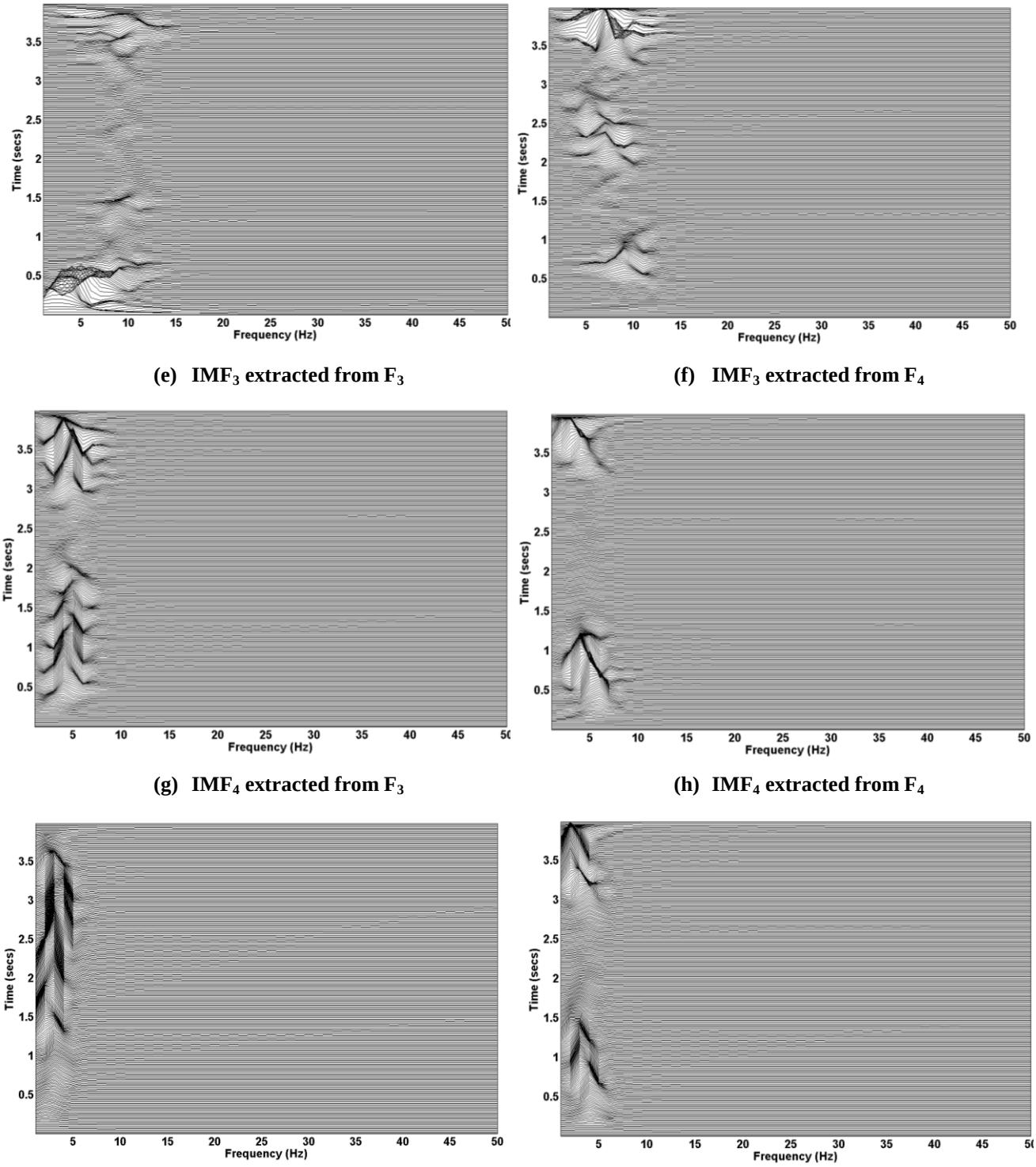

(e) IMF_3 extracted from F_3 **(f) IMF_3 extracted from F_4**

(g) IMF_4 extracted from F_3 **(h) IMF_4 extracted from F_4**

(i) IMF_5 extracted from F_3 **(j) IMF_5 extracted from F_4**

Figure 2.6: T-F representations of the IMFs at five decomposition levels extracted from two adjacent left-right electrodes (F3 and F4).

In order to evaluate the performance of the IF estimators for quantifying newborn EEG generalized phase synchrony, five methods (discussed in section 2.2) were employed. Figure 2.7 exhibits the ROC curves of the IF estimators on the seizure/non-seizure EEG segments. As the figure implies, the sensitivity is significantly higher than the false alarm (1-specificity) for all estimators. It

indicates increased GePS measures within the seizure segments compared to the non-seizure segments.

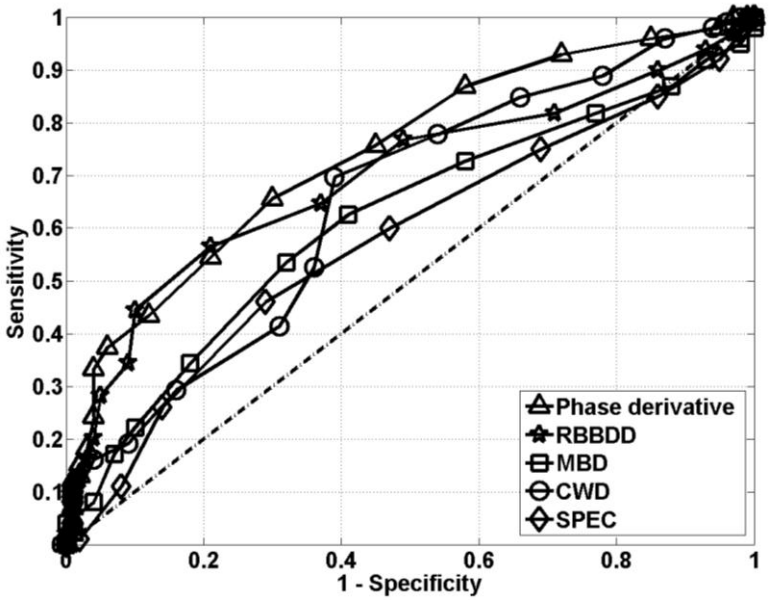

Figure 2.7: ROC curves of the IF estimation methods used in this chapter to extract GePS within the seizure/non-seizure EEG segments.

Table 2.3 contains the AUC values associated with the ROC curves in Figure 2.7. From the table, it becomes clear that most estimators are significantly different from the chance level (50%). However, the AUC values remain lower than what was obtained for the simulated signals (see Table 2.2). Unlike the simulated data analysis, performance of the TFD-based IF estimators on the EEG data is lower than the phase derivative and RBBDD.

Table 2.3: Area under curve for the ROC plots of Figure 2.7

IF estimator	**AUC (%)**
Phase derivative	75
RBBDD	71
CWD	65
MBD	67
SPEC	62

A two-sample t-test was conducted on the newborn EEG results to evaluate the null hypothesis that two groups of GePS values estimated by the unwrapped phase derivative estimator are independent random samples with equal means against the alternative that the means are not equal. The resultant p-value at the 1% significance level was 1.18×10^{-8} implying that the mean GePS values of the seizure group are significantly higher than the non-seizure group ($GePS_{seiz} = 0.46 \pm 0.14, GePS_{nonseiz} = 0.36 \pm 0.08$).

2.4.3 Discussion

The results presented in this chapter show differences between the performances of IF estimators used in the simulated signals and newborn EEG. It was demonstrated that the EMD sifting process can be used in estimating the GePS measure to break down multi-component signals into monocomponent signals, containing relevant information for evaluation of the cointegrating relationships within the multivariate datasets. EMD provides a clearer physical interpretation for synchronization between broadband signals, as it does for the EEG datasets. This is of high importance, as the role of the selected frequency band is always crucial for EEG analysis applications. The IMFs extracted from newborn EEG can be roughly linked to the well-defined EEG frequency bands. The results indicate that the GePS assessment proposed in this chapter can be considered as a global evaluation of phase synchrony over all channels and all frequencies in a typical multi-channel newborn EEG signal. From this point of view, the choice of keeping a constant number of IMFs (here, five) during the whole EEG analysis is compatible with the nature of EEG signals. For the GePS measures derived from synchronization between simulated signals, maximum discrimination rates of 92% and 88% were obtained for the SPEC and CWD-based IF estimators, respectively. The highest rates for newborn EEG signals were 75% and 71% associated with the phase derivative and RBBDD IF estimators, respectively. Unlike the simulations, the performance of TFD-based IF estimators on the newborn EEG data was lower than the phase derivative estimator and the RBBDD method. This observation may imply that the TFD-based IF estimators are more vulnerable to the unknown factors (which will remain in the real EEG signals after pre-processing) compared to the phase derivative and RBBDD. Higher performance of the phase derivative estimator for newborn EEG analysis also suggests that the IMFs extracted from the EEG channels satisfy the requirements of the asymptotic signals [3].

The statistical results also suggest that there is a constant inter-hemispheric connectivity within the newborn brain during the interictal periods as all of the $GePS_{nonseiz}$ values are greater than zero. This is consistent with fMRI-based studies suggesting stable low-frequency, spontaneous fluctuations within the newborn brain during resting-state conditions, termed resting-*state networks* [24, 37]. This study also suggests that the inter-hemispheric connectivity increases during seizure periods in terms of the GePS. This is in agreement with previous neonatal EEG studies where EEG channels are more synchronized within the seizure periods than the non-seizure intervals [94].

The effect of EEG montage is another important factor which needs to be investigated in all EEG phase synchrony assessments. While a monopolar montage has been used for the study presented in this chapter, other montages such as bipolar, average reference and Laplacian montages may give different results. In addition, it is worth exploring the effect of the number of electrodes in each group on the GePS measures. One, however, needs to be careful about selecting the number of

electrodes in EEG connectivity studies including phase synchrony assessment, as highly dense arrangement of the electrodes may increase the interfering effect of volume conduction between neighboring electrodes and affect the connectivity analysis results. Therefore, the effect of volume conduction needs to be explored in future work to assess its impact on the new measure of synchrony.

The ratio of synchronous time periods in the whole newborn EEG signal can be used as an index of newborn brain asynchrony. Such a single number as a representative of asynchronous bursts within a long newborn EEG recording may be used as a qualitative measure of EEG inter-hemispheric asynchrony. This could provide an accurate quantitative measure of asynchrony in the neonatal EEG, and thereby significantly improves the current way of providing only a qualitative description of synchrony/asynchrony from the newborn EEG. Such an objective tool is required to supplement the highly subjective, visual assessment of EEG (see also [45]).

2.5 Summary and conclusions

This chapter establishes the relevance of the GePS assessment for quantifying the global phase synchronization within multivariate nonstationary signals (such as newborn EEG). The contributions of this chapter can be summarized as follows. A novel framework for GePS assessment within nonstationary multi-channel signals has been described based on IP/IF estimation in the T-F domain. The approach has also been evaluated using different T-F methods to optimize its application to newborn EEG seizure detection. The significance of the proposed scheme is demonstrated by the finding that during seizure activity, greater synchrony is observed within multichannel EEG signal. A statistical analysis of the results obtained suggests that the GePS increases significantly during the ictal periods. This is in agreement with previous neonatal EEG studies where EEG channels were more synchronized during ictal periods than in the interictal periods [94]. The promising simulation results suggest the SPEC and CWD-based IF estimators as the most efficient IF estimators for GePS assessment. The TFD-based estimators, however, don't keep their superiority over the phase derivative and RBBDD for the newborn EEG datasets used in this study. The measure may also be utilized as a multivariate EEG feature for newborn EEG seizure detection. However, its discriminating ability needs to be further analyzed and compared with the other existing newborn seizure detection methods. Also, the concept of generalized phase synchrony within the newborn brain calls for a more robust statistical conclusion on larger populations. Unlike classical phase synchrony measures, the proposed measure deals with the generalized phase synchrony in cases where the phase-locking ratio is not rational. This allows a more flexible view of synchronous cycles within the nonstationary multi-channel signals. The

statistical distribution of the GePS measure associated with the interictal (non-seizure) EEG signals of two hemispheres lies always above the zero level suggesting that there may be stable low-frequency and spontaneous fluctuations within the newborn brain. The proposed framework may help quantifying the inter-hemispheric functional connectivity within multi-channel newborn EEG signals. Future work will concentrate on improving the temporal resolution of the proposed approach, utilizing multi-component IF estimation techniques [82], and recruiting more subjects to support the statistical analysis and quantifying other newborn EEG abnormalities such as EEG asymmetry/asynchrony in preterm babies using the proposed approach. The findings of increased synchrony in seizure EEG and variable synchrony in non-seizure periods warrant exploration of the approach in a range of newborn neurological disorders where biomarkers and prognostic indicators are essential to improving management for these babies.

Chapter 3

Measuring time-varying information flow in scalp EEG signals: Orthogonalized Partial Directed Coherence[2]

3.1 Introduction

The human brain performs its sensory and cognitive functions by dynamically employing highly complex and interlaced neuronal networks. Better understanding of these network functions may open insights into pathophysiological mechanisms of neurological development and disease [13]. Due to its non-invasive nature, high temporal resolution and low cost, scalp EEG is often used as the basis for studying brain connectivity [95-101]. A wide range of EEG connectivity analysis methods (like the GePS approach presented in Chapter 2) do not consider the direction of information flow within multichannel scalp EEG signals. However, inter-dependences between surface EEG electrodes are of particular importance when neural communications within cortex such as visual feedback system [102] or evoked response potentials [103] are investigated. Several methods have been developed for assessing directed interactions from EEG (or MEG) signals (reviewed in [104]). Among these, multivariate autoregressive (MVAR) models have been widely used for neurophysiological signal analysis [21, 98, 99, 105, 106]. An MVAR process is able to model interactions between EEG channels in the form of linear difference equations and allows the direction of information flow between channels including direct and indirect influences [106]. The concept of *Granger causality* [107], is widely used to investigate the flow of information within the coupled dynamical networks based on MVAR models. A dynamical process X is said to Granger-cause a dynamical process Y, if the prediction of the process Y is enhanced using the information of the past of process X compared to the knowledge of the past of process Y alone [99]. This definition incorporates the lagged effects only from one channel to another, hence it is also denoted as lagged causality [99]. The immediate effect of a channel on the other channels at the zero delay is called instantaneous causality [99]. The combination of the concepts of lagged and instantaneous causality leads to the general form of extended causality [99]. In this paradigm, the classical MVAR models accounting only for the lagged causality are called *strictly-causal MVAR models*, while the models also considering the zero-lag effects are denoted as *extended MVAR models* [99]. The instantaneous effects built in the strictly-causal MVAR models are reflected in the non-diagonal

[2] This chapter is based on the following publication: *A. Omidvarnia, G. Azemi, B. Boashash, J. O' Toole, P. Colditz, and S. Vanhatalo, "Measuring time-varying information flow for scalp EEG signals: orthogonalized partial directed coherence," to appear in IEEE Transactions on Biomedical Engineering, 2013.*

elements of their noise covariance matrix. Therefore, they can be converted into the extended models using the Cholesky decomposition of their uncorrelated noise covariance matrix [99].

Strictly-causal and extended MVAR models provide the basis for several measures of directional influence in multivariate systems, such as Granger Causality Index (GCI) [108], Directed Coherence [109], Multiple Coherence [110], Partial Directed Coherence (PDC) [109], extended PDC (ePDC) [99], generalized PDC (gPDC) [111], Directed Transfer Function [31, 110], and direct DTF (dDTF) [112] which have been validated using simulated models [99, 106, 109, 113, 114]. Since the focus of this chapter is on the linear approach of time-varying MVAR modelling, we deliberately avoide mentioning the existing non-linear measures here and instead, refer the interested reader to [104, 105, 115, 116].

Ordinary coherence quantifies the linear relationship between two signals in the frequency domain. In a multichannel dataset, the linear relationship between two channels in absence of all other channels is measured by the partial coherence function. In fact, the function removes linear influences from all other channels in order to detect direct interaction between channels i and j [109]. Multiple coherence describes the proportion of the power of the i^{th} channel at a certain frequency which is explained by the influences of all other channels [110]. These coherence measures provide a symmetric representation of the relations between channels, namely, the extracted interrelationship matrix is always symmetrical. Directed coherence is defined as a unique decomposition of the ordinary coherence function and represents the directed interaction between channels. This measure is obtained by spectral decomposition of the cross-spectral density matrix and channel-wise normalization of each element in the matrix [109]. Although the directed coherence has a straightforward physical interpretation in terms of signal power transferred from one process to another, it cannot distinguish between direct and indirect causal effects within the channels. DTF and PDC account for the activity flow in a given direction as a function of frequency/time-frequency. In particular, the PDC inherits useful characteristics of both directed coherence and partial coherence at the same time. While the DTF shows all direct and cascade flows together (e.g. both propagations 1→2→3 and propagation 1→3 are reflected in it), dDTF [112] can separate direct flows from indirect flows [9, 10]. The two frequency domain approaches to connectivity analysis (PDC vs. DTF) are designed to assess different properties in the signal with each having its own advantages and disadvantages [22, 101, 106, 109, 113]. The measure gPDC [111] combines the idea of DTF (to show the influencing effects) and PDC (to reflect influenced effects) between channel i and channel j. Also, GCI [108, 113] is a time-domain connectivity measure based on the concept of Granger causality. The original versions of the previously discussed measures assume that the underlying signals are stationary and their interactions are constant over time, which has made their use challenging for EEG - a known time-varying (non-

stationary) signal [117, 118]. This has prompted the development of time-varying MVAR-based connectivity measures for EEG signal processing [100, 106, 114].

A further significant challenge in connectivity analysis of scalp EEG (or sensor space MEG) is the effect of volume conduction where a given brain source is often reflected in several EEG/MEG signals, and consequently, their similarity may be falsely perceived as 'connectivity' by the analysis paradigms [119]. This is particularly problematic with the MVAR-based connectivity measures that are sensitive to volume conduction effects (for example, see page 94 in ref [120]). A potential solution is to perform the EEG/MEG connectivity analysis at the source level [121], although this would require sufficiently reliable source localization [122]. An intriguing idea for an alternative solution was provided by a recent study that mitigated the effect of volume conduction in the analysis of spatial EEG amplitude correlations [123] by orthogonalizing signal powers. A well-known related procedure is use of the imaginary part of the (ordinary) coherence function [119], which renders the estimate insensitive to instantaneous effects between two signals. In the present chapter, the ideas of the dual extended Kalman filter (DEKF)-based time-varying PDC analysis [21], orthogonalization and imaginary part of coherence function are combined leading to an orthogonalized version of the classical PDC, which is hereafter called orthogonalized PDC (OPDC). It is proposed here that combining orthogonalization and the imaginary part of coherence has the potential to reduce spurious co-variability, the common result of volume conduction effects. Moreover, its generalized version (called gOPDC) is developed to handle the numerical problem associated with potentially different variance of signal amplitudes (known as 'time-series scaling [111]). The novel OPDC paradigm is compared with the classical PDC and gPDC, first using simulated time-invariant and time-varying models, and then using task-related EEG data obtained from flash light-evoked EEG responses of newborn babies. Finally, stringent statistical testing is applied to assess significances of individual findings, and the time-frequency (T-F) connectivity maps are subsequently visualized in 3D directed graphs of the baby's head to demonstrate the potential power of the proposed method in studying dynamical brain networks.

3.2 Methods

3.2.1 Multivariate autoregressive model

For a given time series $y[n] \in \mathbb{R}^M$ with L number of samples ($n = 1, \dots, L$), a strictly-causal multivariate autoregressive (MVAR) model of order p is defined as [90]:

$$\begin{bmatrix} y_1[n] \\ \vdots \\ y_M[n] \end{bmatrix} = \sum_{r=1}^{p} A_r \begin{bmatrix} y_1[n-r] \\ \vdots \\ y_M[n-r] \end{bmatrix} + \begin{bmatrix} w_1[n] \\ \vdots \\ w_M[n] \end{bmatrix} \tag{3.1}$$

where $[w_1 \cdots w_M]^T = w$ is a normally distributed real valued zero-mean white noise vector with diagonal covariance matrix $\Sigma_w = \langle ww^T \rangle = diag\{\lambda_{kk}^2\}$ where $\langle . \rangle$ is the expected value operator and M denotes the number of channels. The assumption of diagonality for Σ_w ensures that there is no instantaneous effect within the MVAR model described in (3.1), as there is no non-diagonal element in Σ_w [99]. The matrices A_r are given by:

$$A_r = \begin{bmatrix} a_{11}^r & \cdots & a_{1M}^r \\ \vdots & \ddots & \vdots \\ a_{M1}^r & \cdots & a_{MM}^r \end{bmatrix} \tag{3.2}$$

for $r = 1, \dots, p$. The real valued parameter a_{kl}^r reflects the linear relationship between channel k and channel l at the delay r. In the stationary case, the optimum order p of an MVAR model can be estimated using different methods such as Akaike Information Criterion (AIC) and Schwarz's Bayesian Criterion (SBC) [101, 124].SBC has been shown to be preferable over AIC for time series analysis [125]. For a reliable estimation of the MVAR parameters, the number of data points available (ML) need to be significantly larger than the number of parameters (M^2p) or equivalently, the signal length (L) should be much longer than Mp [90].

3.2.2 Time-varying PDC Measure

Partial and directed relationships in a network can be detected using the PDC measure. As an example, suppose channel 1 affects channel 2 and channel 2 affects channel 3, that is. 2←1, 3←2 where the arrows show the direction of the information flow. In this case, channel 1 has a direct relationship with channel 2, while there is an indirect (partial) relationship between channel 1 and channel 3. It has been shown in previous studies that the PDC measure outperforms its MVAR-based counterparts for connectivity analysis because it misses this partial relation [22, 109, 113].

The PDC measure is based on the concept of Granger causality [109]. The time-varying version of the PDC is defined based on the time-varying version of the model given in (3.1) (in which matrices $A_r[n]$ are time-varying) as [114]:

$$\pi_{kl}(n,f) \triangleq \frac{|A_{kl}(n,f)|}{\sqrt{a_l^H(n,f)a_l(n,f)}} \tag{3.3}$$

where $a_l(n,f)$ is the l'th column of $A(n,f)$ defined as:

$$A(n,f) = I - \sum_{r=1}^{p} A_r[n]z^{-r}|_{z=e^{j2\pi f}} \tag{3.4}$$

where I is the identity matrix and the frequency f varies within the range of 0 to the Nyquist rate. In (3.3), $A_{kl}(n,f)$ is the kl'th element of $A(n,f)$, a_l^H denotes the Hermitian transpose of the vector a_l and $|.|$ represents the absolute value operator. The measure $\pi_{kl}(n,f)$ takes values between 0 and 1 where high values in a certain T-F bin reflects a directionally linear influence from channel l to

channel k at that bin ($CH_k \leftarrow CH_l$). Note that the measure is directional, i.e., $\pi_{kl}(n,f)$ is not equal to $\pi_{lk}(n,f)$ necessarily. The scale invariance version of the classical PDC (called generalized PDC or gPDC) is obtained by incorporating the variances of the innovation processes $w_i[n]$ [99, 111]:

$$\tilde{\pi}_{kl}(n,f) \triangleq \frac{{\lambda_{kk}}^{-1}|A_{kl}(n,f)|}{\sqrt{a_l^H(n,f)\Sigma_w^{-1}a_l(n,f)}}. \tag{3.5}$$

where λ_{kk} are the diagonal elements of Σ_w. The null hypothesis in the statistical significance test of the PDC-based connectivity analysis is then stated as:

$$H_0: PDC_{kl}(n,f) = 0, \tag{3.6}$$

where $PDC_{kl}(n,f)$ is either $\pi_{kl}(n,f)$ or $\tilde{\pi}_{kl}(n,f)$. Rejection of H_0 implies a significant partial directed outflow of information from channel l to channel k [111].

3.2.3 Time-varying orthogonalized PDC for reducing the effect of volume conduction

The cortical electrical activity recorded by a scalp electrode is a space-averaged potential that is often considerably affected by spatial smearing in the tissue layers between cortex and scalp [126]. This process, known as volume conduction, leads to co-variability in the EEG signal amplitude that is not due to true connectivity between underlying cortical activities. This effect needs attention in the pre-processing stage in any EEG connectivity analysis to differentiate presumably genuine brain interactions from those caused by smearing of EEG signal via volume conduction. To reduce the co-variability due to spatial smearing of the surface EEG signals, one can orthogonalize their power envelopes in the complex domain to remove the parallel components and extract the orthogonal parts [123]. The orthogonal components are then used in the connectivity analysis. Note that two signals can be orthogonal and still correlated [127]. The power envelope of a random signal represents the temporal evolution of its spectral power and can be derived using Morlet's wavelets [123] or the Hilbert transform [128]. Parametric or non-parametric (FFT-based) methods are also used to explore the frequency content of the signal. It is known, however, that the FFT-based methods inherit performance limitations of the FFT approach. Namely, they are unable to provide high-frequency resolution and also suffer from the spectral leakage caused by the effect of windowing on the signal. Autoregressive (AR) model-based spectral estimation methods can overcome these limitations by fitting the observations to an AR model. These methods can be extended to multivariate signals using (3.1) leading to the power spectral density (PSD) matrix. Therefore, the MVAR model coefficients in (3.1) and (3.4) reflect the interactions within the channels and at the same time, they represent the spectral information of the signal power envelopes. The main idea behind the OPDC and gOPDC measures is that instead of performing the orthogonalization process at the signal level, it can be done at the level of MVAR coefficients to alleviate the effect of mutual sources [129].

Suppose scalp EEG channels are generated through a linear superposition of K independent source signals within the brain with instantaneous effect on the surface electrodes. This relationship can therefore be formulated in the frequency domain using Fourier transform as follows:

$$Y_i(f) = \sum_{k=1}^{K} v_{ik} S_k(f). \tag{3.7}$$

Equation (3.7) can be re-written in its matrix form:

$$Y(f) = VS(f) \tag{3.8}$$

where $Y(f) \in \mathbb{C}^M$ is the multichannel EEG signal in the frequency domain, $S(f) \in \mathbb{C}^K$ is the multivariate source signal in the frequency domain, and $V \in \mathbb{R}^{M \times K}$ includes all source weights:

$$V = \begin{bmatrix} v_{11} & \cdots & v_{1K} \\ \vdots & \ddots & \vdots \\ v_{M1} & \cdots & v_{MK} \end{bmatrix}. \tag{3.9}$$

Note that zero lag between the source signals and the sensor realizations ensures that the matrix V is real-valued. Assuming independence among sources, that is $< S_i(f) S_j^*(f) >= \delta_{ij} \langle |S_i(f)|^2 \rangle$ with δ_{ij} denoting the Kronecker delta, the cross-spectral density function $C_{ij}(f)$ between $Y_i(f)$ and $Y_j(f)$, i.e. :

$$C_{ij}(f) =< Y_i(f) Y_j^*(f) >= \sum_{k=1}^{K} v_{ik} v_{jk} \langle |S_k(f)|^2 \rangle \tag{3.10}$$

is necessarily real-valued [119]. Now, let us fit a strictly-causal MVAR model on the multichannel EEG signal $y[n]$ in the time domain according to (3.1) and transform it into the frequency domain. We have:

$$Y(f) = \sum_{r=1}^{p} A_r e^{-j2\pi fr} Y(f) + W(f) = B(f) Y(f) + W(f) \tag{3.11}$$

where

$$B(f) = \sum_{r=1}^{p} A_r e^{-j2\pi fr}, \tag{3.12}$$

$$B_{kl}(f) = \sum_{r=1}^{p} a_{kl}^r e^{-j2\pi fr}. \tag{3.13}$$

Combining (3.8) and (3.11), we have:

$$Y(f) = B(f) VS(f) + W(f) \tag{3.14}$$

Then, the cross-spectral density matrix of $Y(f)$, namely $C(f)$ can be computed as:

$$C(f) = \langle Y(f) Y^H(f) \rangle = \langle \big(B(f) VS(f) + W(f)\big) \big(S^H(f) V^H B^H(f) + W^H(f)\big) \rangle. \tag{3.15}$$

where the superscript H denotes the Hermitian operator. Assuming the source signals and noise processes are statistically independent, (3.15) is written as:

$$C(f) = \langle \big(B(f)VS(f)S^H(f)V^H B^H(f)\big)\rangle + \langle W(f)W^H(f)\rangle. \tag{3.16}$$

Therefore, $C_{ij}(f)$ in (3.10) can be obtained based on (3.16) as:

$$C_{ij}(f) = \langle \sum_{n_1=1}^{M}\sum_{n_2=1}^{M}\sum_{k_1=1}^{K}\sum_{k_2=1}^{K} B_{in_1}(f)B^*_{jn_2}(f)v_{n_1k_1}v_{n_2k_2}S_{k_1}(f)S^*_{k_2}(f)\rangle + \langle W_i(f)W_j^*(f)\rangle. \tag{3.17}$$

Since $S_{k_1}(f)$ and $S_{k_2}(f)$ are independent, all terms including $\langle S_{k_1}(f)S^*_{k_2}(f)\rangle, k_1 \neq k_2$ are zero resulting in:

$$C_{ij}(f) = \sum_{n_1=1}^{M}\sum_{n_2=1}^{M}\sum_{k=1}^{K} B_{in_1}(f)B^*_{jn_2}(f)v_{n_1k}v_{n_2k}|S_k(f)|^2 + \langle W_i(f)W_j^*(f)\rangle. \tag{3.18}$$

True interaction between channels, independent from the pure effect of mutual sources (that is, relations in which the effect of mutual independent sources has been excluded) is reflected in the imaginary part of $C_{ij}(f)$. Since $v_{n_1k}v_{n_2k}|S_k(f)|^2$ and $\langle W_i(f)W_j^*(f)\rangle$ are necessarily real-valued, $Imag\{C_{ij}(f)\}$ will be written as:

$$Imag\{C_{ij}(f)\} = \sum_{n_1=1}^{M}\sum_{n_2=1}^{M}\sum_{k=1}^{K}\Big\{v_{n_1k}v_{n_2k}|S_k(f)|^2 Imag\{B_{in_1}(f)B^*_{jn_2}(f)\}\Big\}. \tag{3.19}$$

Therefore, the terms $Imag\{B_{in_1}(f)B^*_{jn_2}(f)\}$ are associated with the true interactions between channels devoid of the effect of mutual sources and given by:

$$Imag\{B_{in_1}(f)B^*_{jn_2}(f)\} = \sum_{r_1=1}^{p}\sum_{r_2=1}^{p} a_{in_1}^{r_1}a_{jn_2}^{r_2}\, sin\big(2\pi f(r_1 - r_2)\big) \tag{3.20}$$

$$\begin{aligned} &= \sum_{r_1=1}^{p}\sum_{r_2=1}^{p} a_{in_1}^{r_1}a_{jn_2}^{r_2}\, sin\big(2\pi f(r_1)\big)\, cos\big(2\pi f(r_2)\big) \\ &\quad + \sum_{r_1=1}^{p}\sum_{r_2=1}^{p} a_{in_1}^{r_1}a_{jn_2}^{r_2}\, sin\big(2\pi f(r_2)\big)\, cos\big(2\pi f(r_1)\big). \end{aligned} \tag{3.21}$$

Thus the orthogonalized components of $a_{kl}^r e^{-j2\pi fr}, k = 1, \dots, M,\ \ l = 1, \dots, M$ at different delays, i.e. the real part $a_{kl}^r cos(2\pi fr)$ and the imaginary part $a_{kl}^r sin(2\pi fr)$ play a salient role in estimating the true relations between channels, when the effect of mutual sources has been excluded. In fact, the orthogonalized components at different delays do not share the trivial co-variability caused by linear superposition of independent sources. Based on this rationale, the orthogonalized version of the classical time-varying PDC (called OPDC) is proposed as a combination of the orthogonal components of the MVAR coefficients in the time-frequency domain given by:

$$\Psi_{kl}(n,f) \triangleq \frac{\left|\sum_{r_1=1}^{p}\sum_{r_2=1}^{p} a_{kl}^{r_1}[n]\, a_{kl}^{r_2}[n]\, cos(2\pi f r_1)\, sin(2\pi f r_2)\right|}{a_l^H(n,f)a_l(n,f)} \tag{3.22}$$

$$= \frac{\left|\sum_{r_1=1}^{p}\sum_{r_2=1}^{p} Real\{a_{kl}^{r_1}[n]e^{-i2\pi f r_1}\} Imag\{a_{kl}^{r_2}[n]e^{-i2\pi f r_2}\}\right|}{a_l^H(n,f)a_l(n,f)}. \tag{3.23}$$

Summation of the weighted sine and cosine terms in (3.22) imposes a trend varying appearance to the OPDC measure along the frequency axis. It is straightforward to show that (3.22) and (3.23) are equivalent with the following decomposition of $\pi_{kl}(n,f)$ in (3.3):

$$\Psi_{kl}(n,f) = \frac{|Real\{A_{kl}(n,f)\}|}{\sqrt{a_l^H(n,f)a_l(n,f)}} . \frac{|Imag\{A_{kl}(n,f)\}|}{\sqrt{a_l^H(n,f)a_l(n,f)}} \qquad if\ k \neq l. \tag{3.24}$$

Since each factor in (3.24) is greater than zero and less than $\pi_{kl}(n,f)$, the measure $\Psi_{kl}(n,f)$ will always take values between zero and 1. In analogy to the definition of gPDC, the OPDC can be extended to the gOPDC $\widetilde{\Psi}_{kl}(n,f)$ by taking the effect of time series scaling into consideration:

$$\widetilde{\Psi}_{kl}(n,f) = \frac{1}{\lambda_{kk}^2} \frac{|Real\{A_{kl}(n,f)\}|}{\sqrt{a_l^H(n,f)\Sigma_w^{-1}a_l(n,f)}} . \frac{|Imag\{A_{kl}(n,f)\}|}{\sqrt{a_l^H(n,f)\Sigma_w^{-1}a_l(n,f)}} \qquad if\ k \neq l. \tag{3.25}$$

In the next sections, the proposed measures are evaluated on two simulated models consisting of a time-invariant as well as a time-varying strictly-causal MVAR model affected by a linear superposition of independent sources.

3.3 Testing the gOPDC Paradigm

To evaluate the performance of the OPDC and gOPDC measures against the performance of the classical PDC and gPDC, two independent simulations were conducted covering both time-invariant and time-varying circumstances. The basic form of the time-invariant model was used in [109] to reflect the superiority of the PDC to the DTF. Also, the time-varying one has been previously used in [114] to extract time-variant directed influences during Parkinsonian tremor. The models were then manipulated by adding random interactions between channels to test the integrity of the proposed connectivity analysis framework.

3.3.1 Time-invariant simulated model

The model is a 5-dimensional time-invariant strictly-causal MVAR[1]-process plus a linear superposition of sparse uniformly distributed random sources with approximately 50% nonzero entries within the interval [0 3], given by:

$$x[n] = y[n] + Vs[n] \tag{3.26}$$

where $y[n]$ is a strictly-causal MVAR model of order 3 with 5 channels and $x[n]$ is its distorted version with some confounding instantaneous interferences between channels defined by $V \in \mathbb{R}^{5\times 6}$,

a time-constant random mixing matrix and $s[n]$ the intermittent interactions between channels given as a 6-channel sparse uniformly distributed random matrix with 50% nonzero entries. The matrix V is a weighting matrix whose element in the i, j position represents the random interaction between the i^{th} and j^{th} component of $s[n]$. In fact, it has assumed that six sparse and instantaneous relationships are being imposed randomly on $y[n]$. The distorted matrix $x[n]$ is finally used for connectivity analysis. The elements of V were selected from the interval [0, 1] through a uniformly distributed pseudorandom generator. The MVAR process $y = [y_1\ y_2\ y_3\ y_4\ y_5]^T$ is expressed as (see also [109]):

$$\begin{cases} y_1[n] &= 0.95\sqrt{2}y_1[n-1] - 0.9025y_1[n-2] + 10w_1[n] \\ y_2[n] &= 0.5y_1[n-2] + 5w_2[n] \\ y_3[n] &= -0.4y_1[n-3] + w_3[n] \\ y_4[n] &= -0.5y_1[n-2] + 0.25\sqrt{2}y_4[n-1] + 0.25\sqrt{2}y_5[n-1] + 1.5w_4[n] \\ y_5[n] &= -0.25\sqrt{2}y_4[n-1] + 0.25\sqrt{2}y_5[n-1] + 2w_5[n] \end{cases} \quad (3.27)$$

where $w = [w_1\ w_2\ w_3\ w_4\ w_5]^T$ is a normally distributed white noise vector with different variances for its entries. The model is simulated for $L = 2000$ samples at the sampling frequency $F_s = 200\ Hz$.

3.3.2 Time-varying simulated model

The model is a 3-dimensional time-varying strictly-causal MVAR[1]-process plus a linear superposition of sparse uniformly distributed random sources with approximately 50% nonzero entries within the interval [0 1], given by (3.26) where $V \in \mathbb{R}^{3\times6}$ is a time-constant mixing matrix and $s[n]$ represents the intermittent interactions between channels. Similar to the time-invariant case, the elements of V were selected from the interval [0, 1]. The MVAR process $y = [y_1\ y_2\ y_3]^T$ is denoted as (see also [114]):

$$\begin{cases} y_1[n] &= 0.59y_1[n-1] - 0.20y_1[n-2] + b[n]y_2[n-1] + c[n]y_3[n-1] + w[n] \\ y_2[n] &= 1.58y_2[n-1] - 0.96y_2[n-2] + w_2[n] \\ y_3[n] &= 0.60y_3[n-1] - 0.91y_3[n-2] + w_3[n] \end{cases} \quad (3.28)$$

where $w = [w_1\ w_2\ w_3]^T$ is a normally distributed white noise vector. For a model of length $L = 2000$ samples and the sampling frequency $F_s = 200\,Hz$, parameters $b[n]$ and $c[n]$ are depicted in Figure 3.1. For MVAR parameter estimation, the model order is fixed to 2 throughout the process.

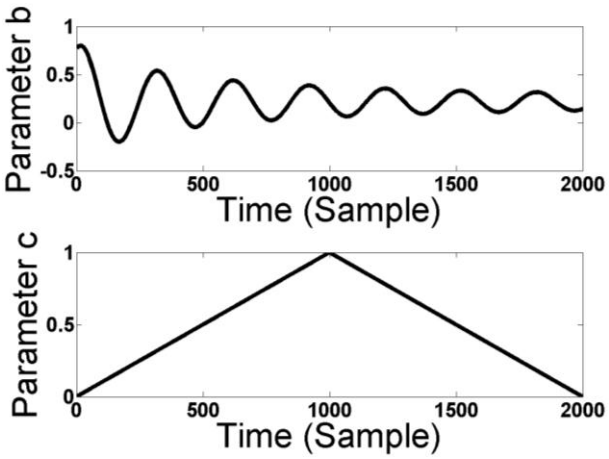

Figure 3.1: Time course of the time-varying parameters in the simulated model (see also [114]).

3.3.3 Newborn EEG data

20-channel EEG recordings of four full-term newborns were obtained from EEG archives in the Department of Children's Clinical Neurophysiology (Helsinki University Central Hospital, Finland). The signals were recorded during sleep with sampling rate of 256 Hz using a NicoOne EEG amplifier (Cardinal Healthcare, USA) and EEG caps (sintered Ag/AgCl electrodes; Waveguard, ANT-Neuro, Germany) with positioning according to the international 10-20 standard (see [130] and http://www.nemo-europe.com/en/educational-tools.php for further details of the newborn EEG recording method). To capture connectivity in the brain network associated with visual processing (postcentral) driven by the visual stimuli, ten monopolar channels were selected (Cz as the reference - see also Figure 3.7) and divided into two groups representing left (O1,C3,P3,T3,T5) and right (O2,C4,P4,T4,T6) hemispheres. The analysis of functional connectivity was then performed on each hemisphere (group) separately. Visual stimuli were delivered with the routine flash stimulator of the NicOne EEG system at 1 Hz for 5 minutes (thus a total of 300 times). The continuous multichannel EEG recordings were then segmented into one-second non-overlapping epochs each of which included one of the 1 Hz visual stimuli. Use of these anonymized EEG recordings has approval from the Ethics Committee of the Hospital of Children and Adolescents, Helsinki University Central Hospital.

3.3.4 Pre-processing prior to the OPDC analysis

The following sequence of pre-processing was applied on the continuous raw EEG data using EEGLAB functions [131]: independent component analysis [132] was used to remove ECG artifact, mains noise (50 Hz) as well as potential artifacts introduced by the flash stimulator directly to the EEG electronics. All 20 EEG electrodes were used at this stage to maximize the reliability of ICA operation [1]. The signal was band-pass filtered between 0.1 Hz and 30 Hz (using a Finite

Impulse Response -FIR- filter of order 200). Periods of the EEG with exceedingly high artifacts were then visually identified, marked manually, and excluded from the later analysis. The remaining epochs were submitted for further analysis (212±28.6 average number of epochs per hemisphere).

3.3.5 Statistical testing of EEG responses

In order to evaluate the significance of the tv-gOPDC results, statistical hypothesis testing was employed for each individual pair-wise connection within a multichannel EEG dataset using a null distribution generated from the signal itself. The null hypothesis is stated as statistical similarity between the baseline condition and post-stimulus activation. In other words, it was tested whether the gOPDC measure after flash light stimulation is statistically different from the gOPDC measure without brain activity triggered by the flash. This approach acknowledged the idea that brain areas may interact spontaneously in the absence of external stimulation leading random connectivity between EEG channels. Hence, the statistically significant event-related information flow can be estimated by comparing it to the level of interactions that take place between those same electrodes in the absence of stimulation. Studies on event related oscillatory activity often use 'baseline' subtraction at the trial level [133]. Figure 3.7-a illustrates an example of the clear difference between the baseline (last 400 ms after flash light stimulation) and stimulus-induced components (first 400 ms interval) in a newborn visual evoked potential (VEP) signal. However, it was searched for additional statistical power and analytical stability by generating a null distribution from a larger set of baseline epochs. The statistical approach used is conceptually straightforward and computationally efficient compared to the sample shuffling, that in the used multivariate dataset needed up to 10 hours computation time per baby (using a Windows-based PC of 2.66 GHz Core2 Duo CPU with 8 GB of RAM).

To this end, the null distribution was constructed using the last 400 ms interval of the one-second inter-stimulus EEG epochs, which was found to be beyond all obvious components of VEPs (see also Figure 3.7-a), hence considered as the 'baseline' (typical EEG activity known as "background"). The tv-gOPDC measures were extracted from the first 400 ms of each epoch and compared with a distribution of the same measures extracted from the last 400 ms intervals for all epochs. The procedure of obtaining a T-F thresholding plane for each group (either left or right hemisphere) of each subject is as follows:

1. tv-gOPDC measures are extracted from the whole length (one second) of each epoch. If N is the number of epochs for subject i obtained from either right or left hemisphere, N time-frequency representations of the gOPDC measures are obtained at the end of this step.

2. Each time-frequency representation is divided into two parts: the first one covering the beginning 400 ms interval and the second one covering the last 400 ms interval. First intervals over epochs provide the original estimates and the second intervals build the null distribution's library.
3. The highest score at the 99th percentile of the distribution of each T-F bin over epochs is computed. With the resolution used in this study (3.9 ms × 0.5 Hz), this yields a threshold plane (or matrix) with 102 time bins (0.4 s, $F_s = 256$ Hz) and 60 frequency bins ($F_{max} = 30$ Hz), thus altogether 6120 threshold values in the thresholding plane that covers the whole T-F graph.

Figure 3.2 illustrates the above procedure for constructing the thresholding plane that determines significance level of the T-F bins in the gOPDC graph. The statistical testing procedure was applied on the pre-processed data of each subject at each group (hemisphere) to obtain a subject-dependent thresholding plane. To find the T-F bins with significant values over the first 400ms time interval, a T-F threshold was applied to each epoch Average of the thresholded gOPDC plots was computed as the mean connectivity representation of the subject in the under-investigated hemisphere (see Figure 3.2). At the end, each subject had two average multichannel representations, one for each hemisphere.

3.3.6 Implementation of the DEKF-based OPDC measure for the EEG signals

In this chapter, the coefficients $A_r[n]$ in (3.4) are estimated using the dual extended Kalman filter (DEKF) [134]. Time dependent parameters $A_r[n]$ account for the nonstationary behavior of the signals. The DEKF is employed to estimate time-varying MVAR parameters fitted on the multichannel EEG signals. It leads to a time resolved gOPDC measure quantifying the time-varying directed influences within channels in the T-F plane. The resulting DEKF-based T-F plane is constructed on a sample-by-sample basis. Therefore, the time resolution is defined by the sampling step size and the frequency resolution is determined by the number of frequency bins in the gOPDC measure (here, $F_s = 256$ Hz leading to 3.9 ms steps and $N_{FFT} = 2F_s$ leading to 0.5 Hz spectral steps). The MVAR model order determines the frequency resolution of the estimates: low-order MVAR models cannot capture low-frequency components due to their short memory [135]. On the other hand, high-order MVAR models are able to represent rapid changes in the signal, but reliable estimation of their numerous parameters needs lengthy signals. If the signal is known to be stationary (which is not generally true for EEG), the optimum order p can be estimated using different methods such as the Akaike information criterion (AIC) or the Schwarz's Bayesian criterion (SBC) [124]. The model order selection is not straightforward for time-varying MVAR models, as it may vary over time. In this study, the optimal model order is estimated by evaluating the SBC for a range of p values over the entire data using the ARFIT toolbox [124] and is kept

constant during the process. Since the MVAR parameters needed to be inferred from a short EEG segment in this study (one second), the order of the model was kept as low as possible ($p = 5$). The whole procedure of extracting the tv-gOPDC values from the multichannel newborn EEG datasets is depicted in Figure 3.2. The two hemispheres were analyzed as separate groups of electrodes, and quantitative 3-D maps of directed influences were plotted using customized MATLAB functions of eConnectome toolbox [136].

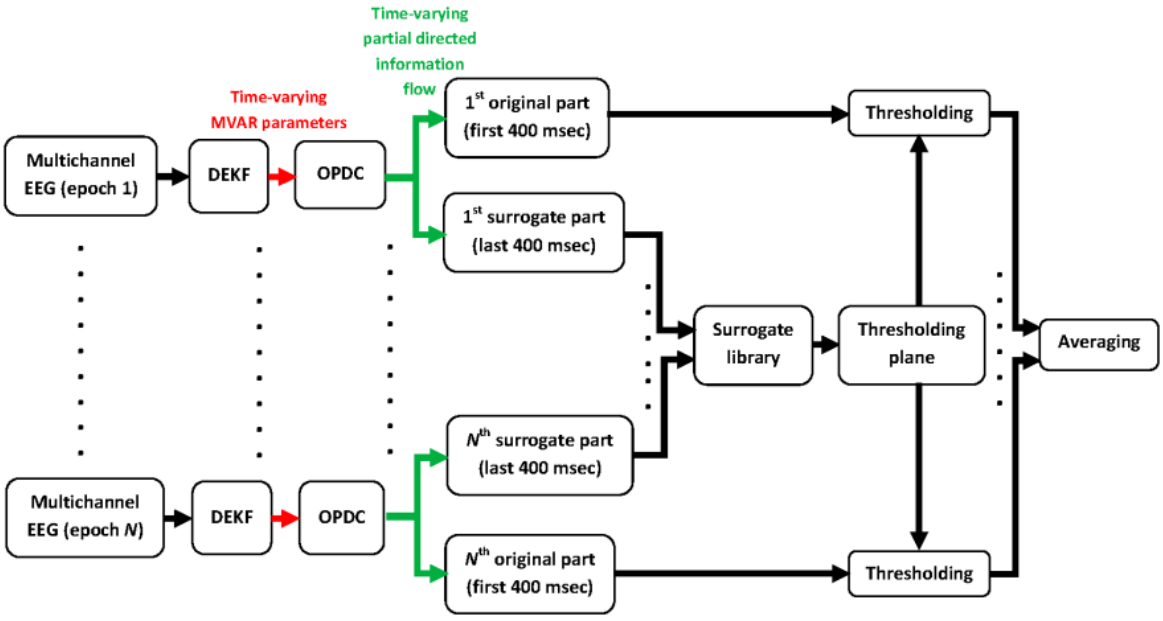

(a)

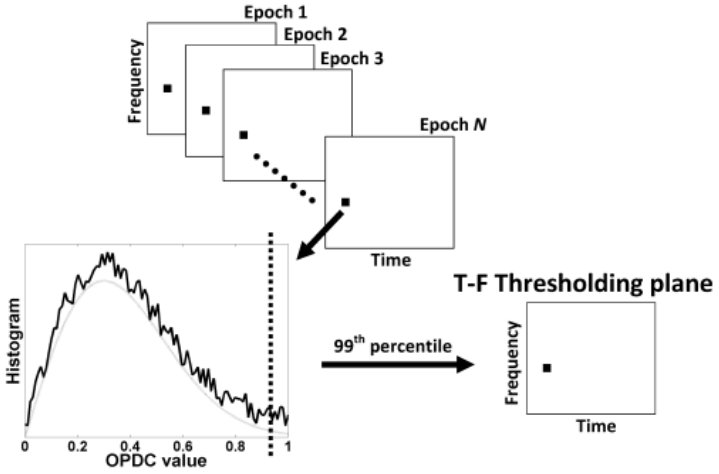

(b)

Figure 3.2: a) The block diagram of implementing the DEKF-based gOPDC measure and the null distribution from N multichannel epochs of the newborn VEP responses. The thresholding plane in the last stage will be used to determine the significant values of the OPDC measures in the T-F domain. b) The procedure of constructing the thresholding plane for the tv-gOPDC measures. Each white square represents a tv-gOPDC representation associated with the last 400 ms of an epoch. The histogram of each T-F bin (small black squares) over all epochs of a group is obtained and its highest score at the 99th percentile is extracted. The estimated value is then used as the threshold of that T-F bin in the thresholding plane.

3.4 Results

The comparison between different methodologies is based on visual inspection (Figure 3.4 and Figure 3.5) analogous to the original PDC study [109]. This was found sufficiently revealing to conclude that there were considerable differences between methods. However, a quantitative measure with statistical testing was used for an objective comparison of the EEG results in which the average tv-gOPDC values over predefined T-F planes were computed (see Figure 3.7).

3.4.1 Time-invariant simulation

The corresponding PDC, gPDC, OPDC and gOPDC measures for the time-invariant model given by (3.26) and (3.27) are plotted in a matrix layout in Figure 3.3. In the ideal case, it is expected to see the immediate impact of channel 1 to channels 2, 3 and 4 as well as the reciprocal effect between channels 4 and 5 (that is, non-zero values for $\pi_{21}(f)$, $\pi_{31}(f)$, $\pi_{41}(f)$, $\pi_{45}(f)$ and $\pi_{54}(f)$, while the other flows are zero). Because of the effect of mutual sources, the classical PDC (Figure 3.3-a) shows an erroneous reflection of the true connections (considerable effect of channel 1 on the other channels) in addition to the spurious leakages among some other channel pairs. The distinctive role of channel 1 in contrast to the other channels refers to its large noise variance. This problem is tackled to some extent by the gPDC (Figure 3.3-b), although leakage due to the effect of mutual sources still exists. The OPDC measure (Figure 3.3-c) alleviates the leakage problem, but is not able to confront the issue of different amplitude scaling. Namely, considerable non-zero values due to the large noise variance of channel 1 are observed for $\Psi_{13}(f)$ and $\Psi_{15}(f)$ in Figure 3.3-c. The gOPDC measure (Figure 3.3-d) takes both the issue of time series scaling and information leakage into consideration and provides the most desired presentation of the information flows.

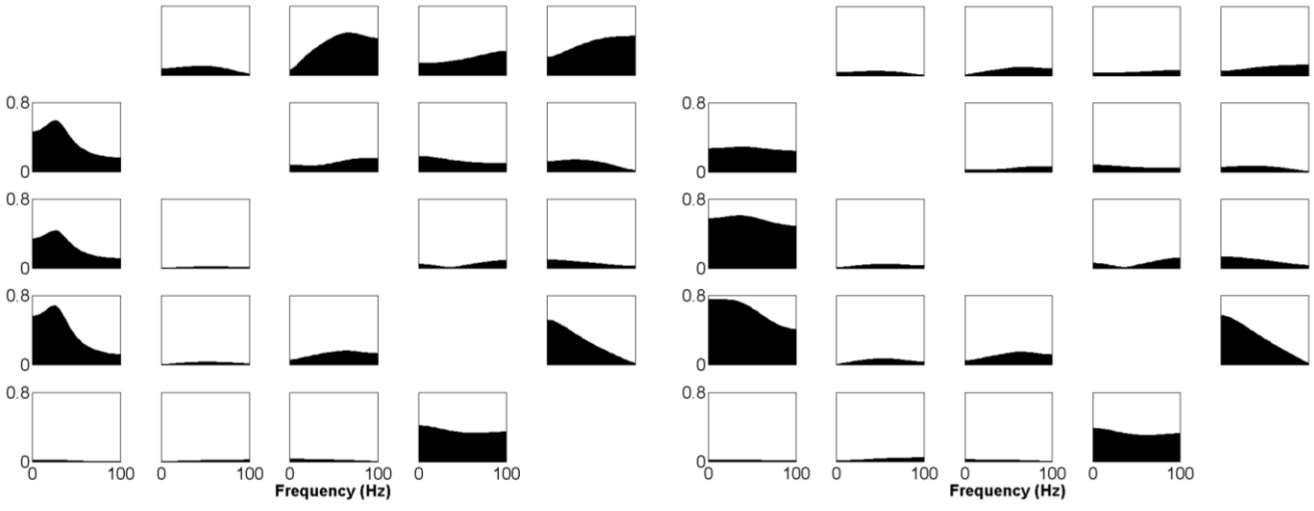

(a) **(b)**

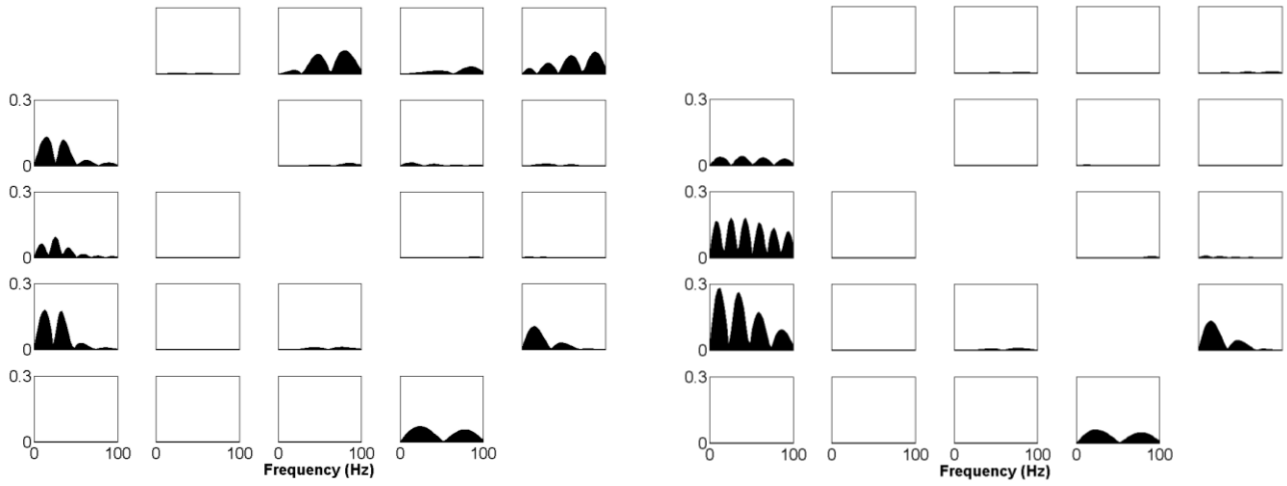

Figure 3.3: Diagrams of the mutual influences within the multichannel time-invariant model given by (3.26) and (3.27): a) PDC, b) gPDC, c) OPDC and d) gOPDC. The diagonal plots (effect of each channel on itself) are excluded from the matrix layouts.

3.4.2 Time-varying simulation

Comparison of the tv-gOPDC measures to tv-gPDC measures on the time-varying simulated model described in (3.26) and (3.28) demonstrates that gOPDC can effectively remove the intermittent interactions between variables (Figure 3.4). In this study, the optimal model order was estimated by evaluating the SBC for a range of p values over the entire data using the ARFIT toolbox [124] and kept constant during the process for all simulations as well as EEG signal analysis. Both measures are able to successfully reflect the oscillatory partial connectivity from channel 2 to channel 1 ($\tilde{\pi}_{12}(n,f)$, $\widetilde{\Psi}_{12}(n,f)$) as well as the ramp-shaped strength influence from channel 3 to channel 1 ($\tilde{\pi}_{13}(n,f)$, $\widetilde{\Psi}_{13}(n,f)$) (see Figure 3.4). According to the model, there is no direct coupling from $y_1[n]$ to $y_2[n]$ and $y_3[n]$, from $y_2[n]$ to $y_3[n]$, and also from $y_3[n]$ to $y_2[n]$. This is reflected well in the corresponding gOPDC graphs with negligible activity. However, the corresponding gPDC graphs for $\tilde{\pi}_{21}(n,f)$, $\tilde{\pi}_{23}(n,f)$, $\tilde{\pi}_{31}(n,f)$ and $\tilde{\pi}_{32}(n,f)$ represent high false positive values. Another large difference can also be observed: the residual connectivity values after removing the effect of mutual sources reveal much smaller magnitude than the gPDC values (note the color bars in Figure 3.4). This observation originates directly from the orthogonalization step in the gOPDC measure where the spurious connectivity caused by the mutual sources is attenuated.

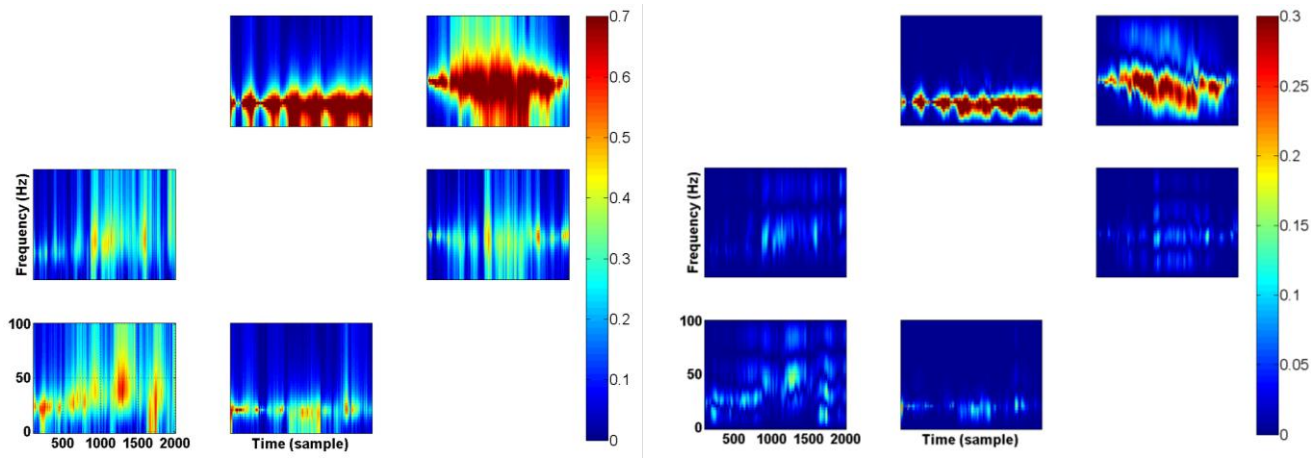

(a) **(b)**

Figure 3.4. The connectivity measures extracted from the simulated model. a) time-varying gPDC, b) time-varying gOPDC. The diagonal plots (effect of each channel on itself) have been excluded from the matrix layouts.

3.4.3 Newborn EEG data

Because the MVAR parameters need to be inferred from a short EEG segment (one second), the order of the model should be kept as low as possible ($p = 5$). Many coefficients of a high-order MVAR model cannot be reliably estimated from a short length signal. Therefore, the optimum model order was selected conservatively as the lowest order at which a near constant plateau appears in the information criterion diagram of the SBC method. On the other hand, low-order MVAR models cannot capture low-frequency components, as they have short memory [135]. Therefore, low-frequency results of this study (below 1-2 Hz) were excluded from the interpretations.

To make sure that the EEG results are not substantially affected by different amplitude scaling in scalp EEG electrodes (see Figure 3.7-a), the gOPDC was used for EEG connectivity analysis and its performance was compared with the gPDC. The time-varying results (Figure 3.5) were obtained for the scalp EEG electrodes of the left hemisphere after thresholding as described above. As shown in, the gPDC levels are notably high and spread across the whole T-F plane with emphasis on low frequency components, whereas gOPDC levels are clearly emphasized around 10 Hz. In particular, the low frequency content (lower than 3 Hz) associated with the mutual components of the newborn EEG signals have been almost eliminated in the gOPDC plots.

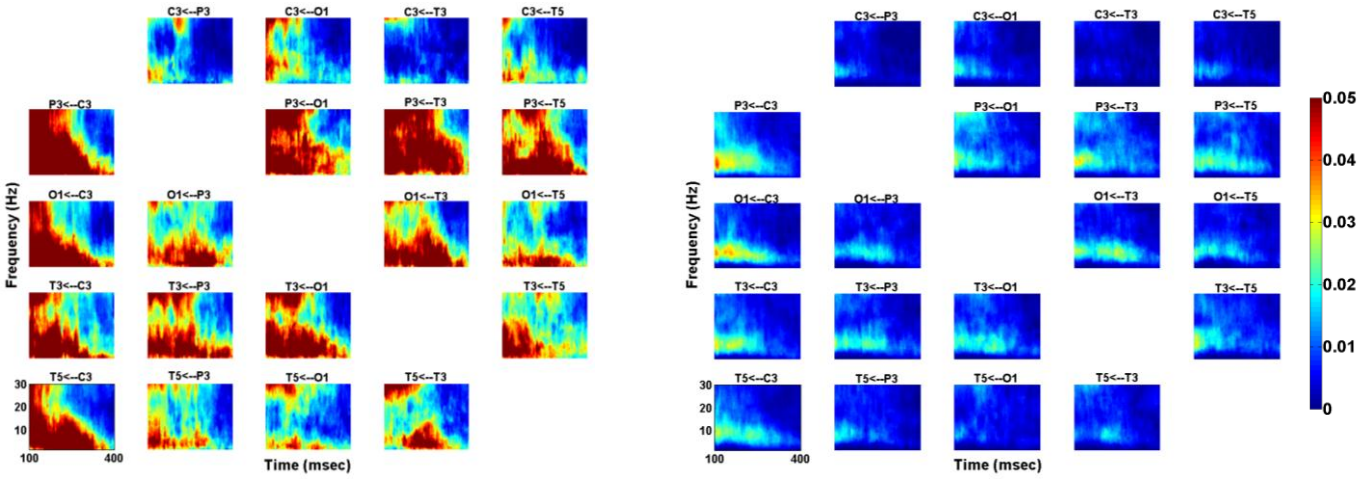

(a) **(b)**

Figure 3.5: Time-varying connectivity analysis of the scalp EEG electrodes from the left hemisphere. A) gPDC measure, b) gOPDC measure.

The time-invariant measures (Figure 3.6) can be readily obtained by temporal averaging of the corresponding time-varying values (Figure 3.5). They show a clearly dominant hump at around 7-10 Hz. In contrast, the gPDC plots show strikingly high levels towards both higher and lower frequency components. It is reasonable to assume that these frequency components represent mainly the "common mode" effect of reference electrode that is unavoidably present in monopolar recordings, which is effectively attenuated by orthogonalization at the level of MVAR parameters.

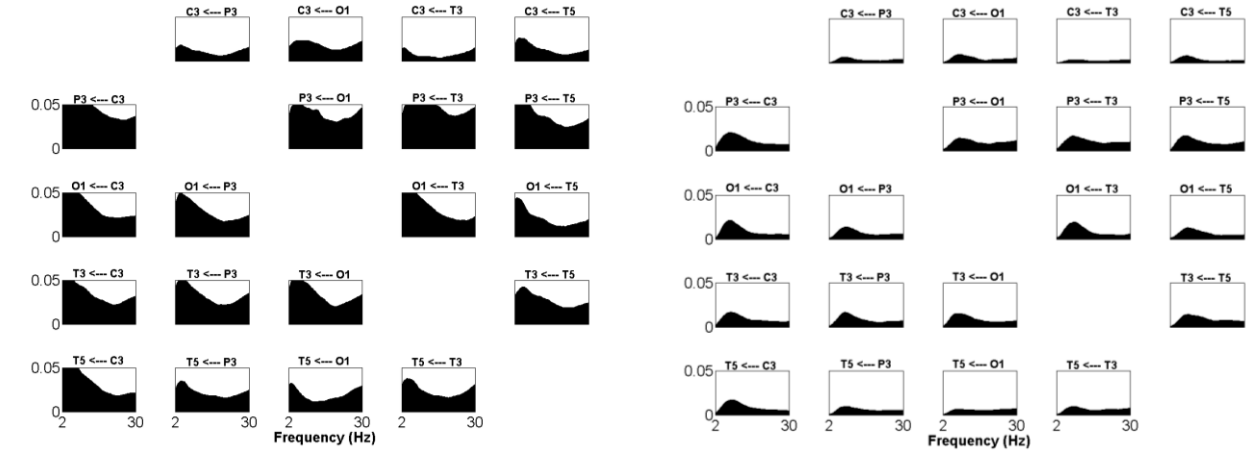

(a) **(b)**

Figure 3.6: Time-invariant connectivity analysis of the scalp EEG electrodes from the left hemisphere. A) gPDC measure, b) gOPDC measure.

The conventional time-locked averaging of the EEG showed canonical shape visual evoked responses in both hemispheres and in all babies (Figure 3.7) with little difference in timing and shape of components between scalp locations. The first components always started before 200ms, and no consistent response components were seen beyond 400ms post stimulus. Notably, all components of this response have a strong spatial decay towards central (C3 and C4) and temporal (T3 and T4) sites, with maximal amplitude in the occipital electrodes (O1 and O2). Based on these observations, the tv-gOPDC analysis was limited to a rectangular time-frequency area from 100ms

post stimulus onwards and within the frequency range of 5-15 Hz (Figure 3.7-d). Grand-mean T-F maps of directional interactions between EEG channels at each hemisphere over subjects are demonstrated in Figure 3.7-b and c. The 3-D connectivity maps of the grand mean interactions at 5-15Hz band were then created from 2-D averaging of the T-F gOPDC values within three different time spans: Δt_1=100-200 ms, Δt_2=200-300 ms and Δt_3=300-400 ms (see Figure 3.7-e, f and g, respectively).

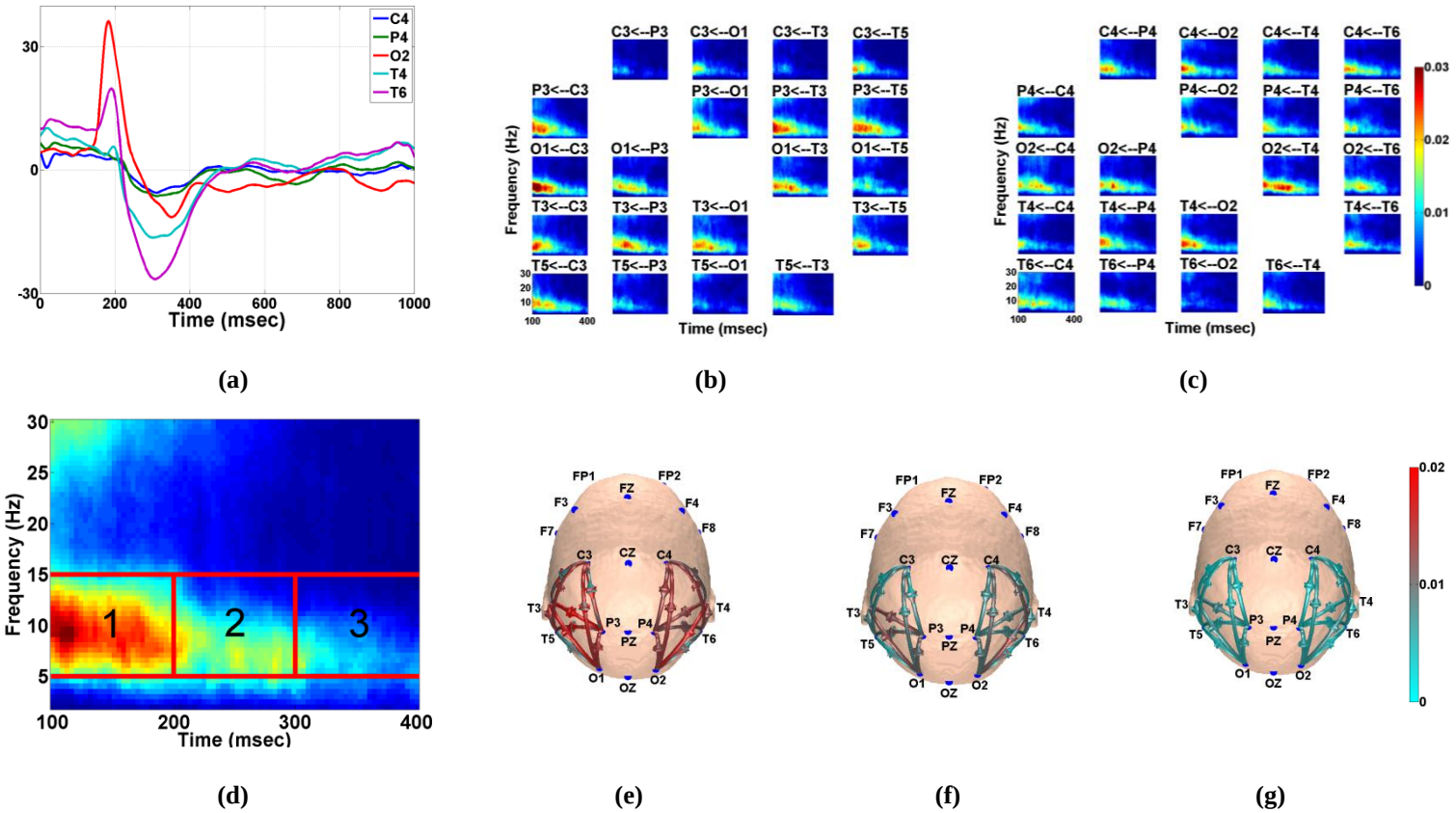

(a) **(b)** **(c)**

(d) **(e)** **(f)** **(g)**

Figure 3.7: a) Average VEPs of a typical subject - responses of the right group of electrodes, b,c) Average tv-gOPDC measures across four subjects for the occipital-temporal-parietal areas from 100 ms to 400 ms post-stimulus at the left and right hemispheres, respectively. The direction of the information flow is presented on top of each map. d) Rectangular T-F compartments over which the gOPDC measure was averaged. e,f,g) Color-coded 3-D directed graphs representing the grand-mean information flow at Δt_1=100-200 ms, Δt_2=200-300 ms and Δt_3=300-400 ms, respectively, after the stimulus onset within the frequency range of 5-15 Hz. Note the substantial decrease of information flow in the last time window compared to the first two time windows. Each color-coded arrow shows a directed interaction between two electrodes.

An overall inspection of the results in Figure 3.7-b,c suggests that there are preferential frequencies and directions of information flow in the T-F domain. To quantify the visual interpretation of the results, the total mean gOPDC value was calculated for each plot. The pair-wise gOPDC maps, i.e. two maps for each electrode pair (one for each direction) can be interpreted as the pure directional 'coherence spectrogram' between the two electrodes, when the effect of volume conduction is removed. Notably, most directed information flow appears to take place at 5-15Hz frequency band, with a general decrease in frequency over time. This change in frequency is, indeed, compatible with the respective changes in the intrinsic frequency content of the average waveforms (Figure 3.7-

a) which show a clear attenuation of interactions towards the end of the 400ms analysis window. The grand mean gOPDC maps (Figure 3.7-b,c) reveal strong interrelations between the occipital and central areas at the left hemisphere and between the occipital and temporal areas at the right hemisphere around the central frequency of 10 Hz (most dominant interactions are O1←C3 and O2←T4). In both matrix layouts (left and right – 40 maps in total), the dominant electrode pairs involve the occipital and parietal electrodes as the sink of information (e.g. P3←T3, O2←T4, O1←C3). In addition, relatively high T-F interactions originate from the temporal lobe and discharge into the occipital and parietal lobes (e.g. P3←T5, P3←T3, O2←T4).

The 3-D plots are compatible with the observations from the time-frequency gOPDC graphs in Figure 3.7-b,c that show attenuation of the interactions in the network over time. In the earliest time window (100-200ms), most connections are active, whereas the interactions weaken towards the end of the analysis time. The 3-D maps also show the long connections from the occipital lobe to the central regions.

3.5 Discussion

It was demonstrated that directional information flow can be assessed in the T-F domain from multivariate EEG datasets, and it can be statistically tested at the level of each individual connection. The method described here stems from combining multiple independent streams of prior analytical development: the core of the OPDC measure and its generalized version is grounded on the T-F representation of MVAR processes and the notion of Granger causality. To render the estimate insensitive to instantaneous effects between two scalp EEG signals, the well-known idea of taking the imaginary part of the coherence function has been used [119]. In this chapter, the idea of time-varying PDC analysis [21] was combined with orthogonalization at the level of MVAR parameters, as considering the imaginary part of the coherence function lead to an orthogonalized version of the classical PDC. Moreover, its generalized version (called gOPDC) was developed to handle the numerical problem associated with varying amplitude scaling between signals. The performance of the gOPDC measure was evaluated using a simulated model and real newborn EEG signals.

The major properties of the tv-gOPDC paradigm and their relationship with the previously published measures can be summarized as follows:

A. The gOPDC approach is based on the strictly-causal MVAR model given in (3.1) which does not consider the instantaneous interactions between EEG channels. An extended MVAR model which takes into account the instantaneous effects will be similar to (3.1) with $A_r \neq 0$ for $r = 0$ [99]. In this case, the gOPDC measure given in (3.25) can be extended in a similar way as presented in [99] where the MVAR coefficients are modified in the presence of zero-lagged

effects. However, it is shown in [99] that if a strictly-causal MVAR model is inaccurately fitted on an extended MVAR process, true instantaneous influences are likely to be reflected as spurious lagged interconnections among the model inputs.

B. In contrast to ordinary coherence, partial coherence, multiple coherence and similar to the DTF, dDTF, PDC and gPDC, the proposed gOPDC method is able to extract direction of the information flow and differentiate between direct/indirect interactions.

C. it inherits all characteristics of the classical PDC which makes it superior to the DTF and dDTF.

D. as opposed to GCI, it can extract both temporal and spectral interactions.

E. in comparison with the PDC and gPDC for the specific application of scalp EEG analysis, it is able to alleviate the distorting effect of volume conduction within multichannel EEG signals.

One should note, however, that the inverse spectral matrix elements employed in the family of PDC-based measures makes physical interpretation of their results difficult in terms of power spectral density.

It was demonstrated that tv-gOPDC using DEKF is able to track changes associated with transient couplings and remove the effect of mutual independent sources within the multivariate nonstationary signals. Most of the existing EEG connectivity analysis methods assume stationarity of interactions in the underlying signals, while EEG signals are well-known to be nonstationary [117, 118]. Also, the effect of volume conduction and the differences in amplitude scaling between EEG signals can pose challenges. The present work introduces a time-frequency framework for functional EEG connectivity analysis to deal with both confounders, and extracts the sequence of nonstationary information flows between EEG channels within sub-second segments and at the lack of scale invariance. This approach obviously requires sufficient signal to noise ratio, which can be achieved by averaging over a larger number of trials. The effects of other sources of constant noise or artefacts, such as mains noise and its harmonics, can be mitigated by efficient artefact handling (see pre-processing steps) and by employing statistical testing of the kind presented in this chapter. The method of generating null distributions from the original EEG segments will directly affect the statistical testing. There are several customized versions of classical surrogate data methods to estimate significance in PDC connectivity analysis [137, 138]. Their application to each epoch in a multivariate dataset (multichannel newborn EEG in this study) is, however, often computationally challenging, and no specific advantages were seen to their use compared to the conceptually straightforward method in this chapter. As an alternative, the null distribution of the presented hypothesis testing (cortical connectivity vs. no connectivity) can be generated using the background EEG in the given experiment, which is also automatically "normalized" with respect to spontaneous (as opposed to event-related) brain connectivity as well as technical variances (for example.

external noise or inter-individual variations in the recording constellation). The method presented in this chapter is conceptually straightforward and computationally efficient.

The effect of EEG montage is another important factor in studies on EEG connectivity. While monopolar montage with Cz reference was used in this study, other montages like Laplacian or average referencing should be explored. Use of monopolar reference outside of the analyzed EEG signals may be perceived as neutral with respect to mixing sources among the analyzed signals; however it also leads to a significant common source in all signals that is technically identical to a serious volume conduction effect. We found it particularly encouraging to see that even such common source component could be alleviated by using the orthogonalization procedure. Using Laplacian or average reference montages would require a high number of recorded EEG channels. Hence, it seems intriguing that the proposed method may even open the possibility to analyze recordings with only few monopolar EEG signals, such as the routine clinical evoked potential studies. However, any effect of the number of electrodes also affects tv-gOPDC measures, and it needs systematic assessment in prospective applications for two reasons: first, higher electrode density implies increased mutual components caused by volume conduction. Second, quantitation of directional interactions between higher number of pair-wise comparisons can dilute the effect between each electrode pair, which calls for higher signal-to-noise ratio. These considerations imply that i) increasing the electrode density may be beneficial when it is used for spatial down-sampling (either at signal or at source space), while ii) the performance of tv-gOPDC improves by selecting a lower number of signal pairs as guided by a priori knowledge about assumed number of underlying, interacting sources. Indeed, such optimization is an inevitable exercise with all advanced analyses of brain interactions.

The ability of the gOPDC in detecting interactions between sources within the cortex in the presence of volume conduction can be quantitatively measured using other simulated models like the one presented in [139] where the interactions at the source level are projected onto the scalp through a realistic lead field matrix. In the special case where source activities are governed by an MVAR process, a different version of (3.26) like $x[n] = Vy[n]$ can be used for simulation purposes in which $x[n]$ is the multichannel scalp EEG, V represents the lead field matrix and $y[n]$ models the lagged source time traces in the form of an MVAR process. The simulation strategy of this study, however, was to look at the EEG connectivity problem from another perspective, namely fitting an MVAR model on the scalp EEG signals (not sources) in the presence of an additive interfering factor.

The time-varying connectivity approach used in this chapter discloses longer range connections from occipital to temporal and central regions, which is strikingly compatible with previous steady state VEP studies in adults [140, 141]. Our proposed analysis methodology as well as the

stimulation paradigm (a routine flash light during routine clinical EEG recording) is directly applicable even for larger scale clinical testing. Notably, a directed information flow, often called 'travelling waves' in the adult literature [142] is considered to be sensitive to changes in sub-cortical structures [143]. In the clinical context, it raises the potential that the proposed paradigm could be used to assess integrity of the sub-cortical structures after acute brain injury, such as birth asphyxia, where diagnostic strategies have remained a challenge [144, 145]. The present paradigm may have applicability to follow change over time in response to therapy and prognostication of long term outcome.

3.6 Summary and conclusions

Estimating time-varying information flow in scalp EEG signals is not a straightforward task. This is due to the effect of volume conduction where a given brain source is often reflected in several EEG/MEG signals, and consequently, their similarity may be falsely perceived as 'connectivity' by the analysis paradigms. This chapter aimed to develop a T-F method for measuring directional interactions over time and frequency from scalp EEG signals in a way that is less affected by volume conduction and amplitude scaling. The tv-gPDC method was modified, by orthogonalization of the strictly causal multivariate autoregressive model coefficients, to minimize the effect of mutual sources. The novel measure, tv-gOPDC, was tested first using two simulated models with feature dimensions relevant to EEG activities. The method was then used for assessing event-related directional information flow from flash-evoked responses in neonatal EEG. For testing statistical significance of the findings, a thresholding procedure driven by baseline periods in the same EEG activity was followed. The results suggest that the gOPDC method **1)** is able to remove common components akin to volume conduction effect in the scalp EEG, **2)** handles the potential challenge with different amplitude scaling within multichannel signals, and **3)** can detect directed information flow within a sub-second time scale in nonstationary multichannel EEG datasets. This method holds promise for estimating directed interactions between scalp EEG channels that are commonly affected by the confounding impact of mutual cortical sources.

Chapter 4

EEG connectivity and resting state networks[3]

4.1 Introduction

Analysis of brain functional connectivity within resting-state networks (RSNs) representing slow and spontaneous intrinsic brain activity has recently come into attention. RSNs, discovered by Biswal et al [23], are spatially long-range brain networks synchronized in time through low-frequency fluctuations (<0.1 Hz) of blood oxygen level-dependent (BOLD) signals, while subjects are apparently resting [24-26]. It has been shown that numerous resting-state relationships can be detected between different cortical areas of the adult brain including the visual cortex, sensorimotor areas and auditory areas using fMRI signal analysis [27]. In other words, the brain during rest is not idle, but it conducts spontaneous, intrinsic activities – both endogenous and sensory driven - associated with human behaviour [28, 29], pain [30, 31] and diseases [1, 32, 33]. In fact, the large-scale RSNs are developed across anatomically remote, but functionally integrated cortical regions [34, 35]. The emergence of RSNs is tightly linked to cortical and thalamocortical development in the newborn brain [10, 24, 36-38]. fMRI studies on sleeping human newborns, including preterm babies, have shown interhemispherically developing RSNs analogous to those seen in older subjects [24, 37, 38]. Investigation of the spanning RSNs within the newborn brain in the presence of neuronal deficits may help to understand the establishment of these networks after injury.

Majority of adult/newborn RSN research has been conducted on fMRI signals. It is known that the networks observed in resting-state fMRI (rs-fMRI) recordings commonly reflect brain activities associated with changes in blood flow. Nonetheless, one expects to find spatial resemblance between the fMRI-based RSNs and those detected by electrophysiological signals such as EEG and MEG recordings due to a causal link between neuronal activity and fMRI signal [146]. This speculation has been verified in adult brain studies exhibiting robust spatial correlations between the frequency-specific power of EEG/MEG signals resembling the fMRI-based RSNs [121, 123, 147, 148]. This, however, may not be the case for newborn brain which changes significantly during the weeks after preterm birth [17] and therefore, follows a fundamentally different neurophysiological mechanism from the more mature one [5-7]. The time-varying nature of the early cortical networks is crucial for endogenous brain wiring, particularly in the third trimester

[3] This chapter is an extended version of the following publication: *A. Omidvarnia, P. Fransson, M. Metsäranta, and S. Vanhatalo, "Functional Bimodality in the Brain Networks of Preterm and Term Human Newborns," Cerebral Cortex, May 2013, doi: 10.1093/cercor/bht120.*

when connections between cortical areas are still forming under the influence of exogenous stimuli such as sensory inputs [5, 6]. A bimodal behavior in the electrical activity of these networks is observed that is characterized by two alternating modes: the high mode associated with the self-organizing, locally generated spontaneous activity transients (SATs, also known as bursts) and the low mode representing low-amplitude intervals between SATs [7-11]. This kind of bimodality gradually attenuates as EEG activity becomes more continuous [10]. In addition, the characteristic cellular level network mechanisms underlying interactions within the healthy/unhealthy brain cortical areas in neonates also differ from those seen in more mature brain [12]. Some EEG patterns which are considered as abnormal signs of adult brain functionality may be normal features in newborn brain [13, 14].

The aim of this chapter is to define functional bimodality within neonatal EEG-based RSNs (also called electric RSNs or eRSNs [10]) of the preterm brain during brain development and also, in the presence of intra-ventricular hemorrhage (IVH), which is a condition characterized by bleeding into or around the preterm infant's brain ventricular system [47]. The extent of IVH is imaged using ultrasound and it is associated with background and epileptiform EEG abnormalities [47]. However, still there is disagreement over the capacities of continuous EEG monitoring for qualifying IVH [47]. In this chapter, the proposed eRSN paradigm is firstly introduced in details. Then, it is evaluated for two groups of healthy preterms and fullterms to characterize the networks during brain development. Finally, the method is applied on EEG recordings of a group of healthy preterm babies and another group of preterm babies with IVH to measure cortical functional connectivity by spatial amplitude correlations between the frequency-specific band amplitude fluctuations (BAFs) computed from scalp EEG signals.

4.2 Materials and methods

4.2.1 EEG data acquisition

For studying the development of bimodality within the newborn brain, 11 healthy human preterm babies (conceptional age 28.3-33.8 weeks) and 10 healthy fullterm babies (conceptional age 37.6-43.5 weeks) were recruited. EEG signals of 6 human preterm babies with IVH (grade 2-4, bilateral) were further added into the analysis to investigate the eRSN characteristics in presence of IVH.

All of the healthy babies had normal serial brain ultrasound examinations, with no diagnosed abnormalities, chronic illnesses or acute inflammations. They received no drug treatments likely to affect the EEG. A clinical neurophysiologist (Dr. Sampsa Vanhatalo) interpreted the data of IVH group as exhibiting significant unilateral/bilateral hemorrhage in all subjects. The signals were recorded during sleep with sampling rate of 256 or 512 Hz using a NicoOne EEG amplifier

(Cardinal Healthcare, USA) and EEG caps (sintered Ag/AgCl electrodes; Waveguard, ANT-Neuro, Germany) which included 28-64 channels with positioning according to the international 10-20 standard (see [130] and http://www.nemo-europe.com/en/educational-tools.php, for further details of the newborn EEG recording method). For each subject, a 5-min continuous segment during quiet sleep was selected by an EEG expert (Dr. Sampsa Vanhatalo) to minimize potential artifacts. The use of these anonymized EEG recordings was approved by the Ethics Committee of the Hospital of Children and Adolescents, Helsinki University Central Hospital.

4.2.2 fMRI data acquisition and preparation

fMRI data of 18 fullterm newborns were acquired during natural sleep using a Philips Intera scanner at 1.5 T4. All babies had normal Apgar [149] score with no visible sign of abnormality in heir anatomical MR scans. More detailed information including age, age at scanning and head geometrical features can be found in [149]. Recordings were performed after obtaining written parental consent for each subject and had the approval of the local ethics committee in Stockholm. In total, 300 image volumes (10 minutes) of BOLD sensitive echo-planar images (TR/TE/flip = 2000 ms/50 ms/80 degrees, matrix size = 64x64, field-of-view = 180x180 mm, 20 axial slices, slice thickness = 4.5 mm, spatial resolution 2.8x2.8x4.5 mm3) were obtained from the neonatal brain. However, only 200 adjacent EPI volumes for each infant were used for further analysis after movement correction. The entire fMRI pre-processing stage was performed by Dr. Peter Fransson using the SPM5 toolbox (Wellcome Department of Imaging Neuroscience, London, UK) and his own developed MATLAB scripts. 39 regions of interest [150] were defined over the neonatal cortex spanning auditory, visual, attention, default, saliency and sub-cortical networks and their corresponding fMRI time series were extracted. Full information of all ROIs is available at Supplementary document of [36]. In fact, the fMRI dataset of each subject was treated as a multichannel signal with 39 channels. All detailed information of the recruited babies including their gestational ages (roughly equal to the conceptional age plus two weeks) can be found in [149].

4.3 Data analysis

The eRSN analysis using BAF envelopes follows a multi-step procedure which is schematically illustrated in Figure 4.1. The analysis starts by pre-processing of the EEG signals, followed by extracting BAF envelopes at the frequency band of interest and evaluating their network characteristics within two modes of activity. The significance of the pair-wise relationships and

[4] The author of this PhD thesis wishes to appreciate Dr. Peter Fransson's courtesy for providing the fMRI datasets.

their corresponding measures is assessed using surrogate signals as well as different statistical testings at individual and group levels as shown in Figure 4.1. The original eRSN process has been published in [10], but the block diagram in Figure 4.1 improves the existing analysis by adding some necessary modifications.

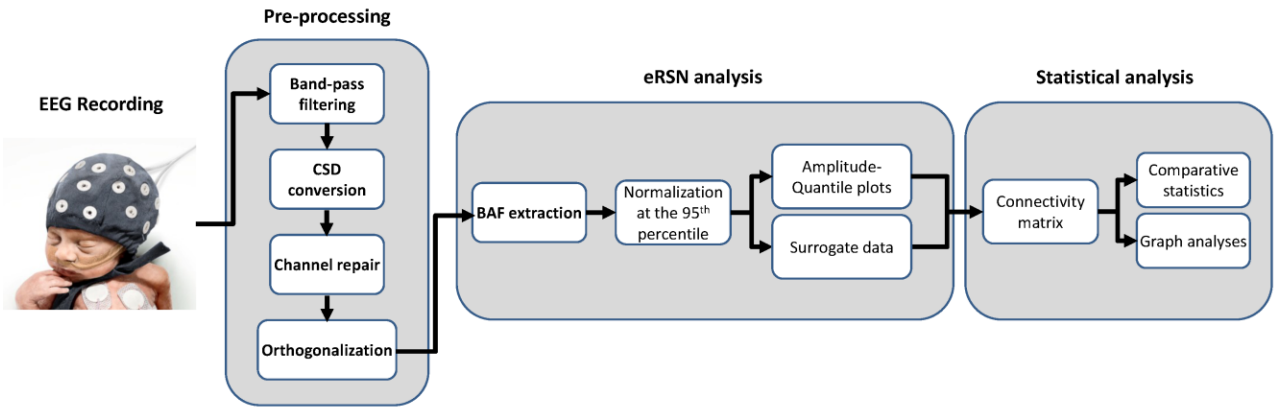

Figure 4.1: block diagram of the eRSN analysis.

4.3.1 Band-pass filtering, CSD conversion and channel repair

Each continuous EEG segment underwent a sequence of pre-processing steps including band-pass filtering at 1-30 Hz, transforming into a reference-free Laplacian current source density (CSD) montage with 21 channels ($\gamma = 5 \times 10^{-6}$ and $m = 4$, see also [151]), repairing bad or missing EEG channels and finally, suppression of the volume conduction effect using orthogonalization. Due to the lack of reliable head models for neonatal EEG source reconstruction, analysis at the source level using scalp EEG signals doesn't lead to precise results for neonates [152]. Therefore, the analysis was conducted at the scalp level after converting the surface EEG data into a Laplacian CSD montage [151] based on the spherical spline interpolation of the recorded surface potentials using the MATLAB-based CSD toolbox [153]. The resulting reference-free (a.k.a minimal smoothing) montage provides higher spatial resolution representing the leaving (sinks) or entering (sources) radial current flows at each electrode. Minimal smoothing in neonatal scalp EEG signals has been described in [152]. Since the electrode positioning and quality of recording were not identical over all EEG datasets, a uniform arrangement of 21 electrodes were selected for all subjects by replacing bad or missing channels based on the information of their neighbour electrodes (function 'eeg_interp' of EEGLAB [154]).

4.3.2 Addressing the volume conduction effect

Spatial smearing of the surface EEG signals was further suppressed by taking the orthogonal projection of each signal power onto the others to diminish common IA components [123]. Pair-

wise orthogonalization of the multichannel EEG-BAF envelopes is a head model-free approach for reducing the spurious co-variability between signal powers. This step aims to reduce the effect of mutual sources on the newborn power envelopes in order to alleviate the volume conduction effect as much as possible. It has been shown in [10] that in contrast to the shallow spatial decay of Spearman's rank correlation between original newborn EEG signal pairs, the correlation between adjacent orthogonalized signal pairs reduces strongly. The mathematical reasoning behind orthogonalization is as follows:

Suppose scalp EEG channels x and y are generated through a linear superposition of K independent dipoles $s_k(f), k = 1, \dots, K$ within the brain with instantaneous effect on the surface electrodes. The spectral representations of x and y, i.e. $X(f)$ and $Y(f)$ are then given by:

$$X(f) = \sum_{k=1}^{K} a_k^x s_k(f) \tag{4.1}$$

$$Y(f) = \sum_{k=1}^{K} a_k^y s_k(f) \tag{4.2}$$

where a_k^x and a_k^y are real coefficients and f is the frequency of interest. Considering the above assumptions on the mutual sources, it can be shown that the cross-spectrum between $X(f)$ and $Y(f)$ is necessarily real [119]:

$$S_{xy}(f) = \langle X(f)Y^*(f) \rangle = \sum_{k=1}^{K} a_k^x a_k^y |s_k(f)|^2. \tag{4.3}$$

Equation (4.3) implies that the real part of the cross-spectrum function between two channels at a certain frequency is always associated with the pure effect of source interactions, while its imaginary part yields interaction of channels without volume conduction in the frequency domain [119].

Now, let $X(t,f)$ and $Y(t,f)$ be the power envelopes of the two channels X and Y at the frequency of interest. The power envelope of a random signal represents the temporal evolution of its spectral power and can be derived using Morlet's wavelets [123] or the Hilbert transform [128]. According to (4.3), the contribution of Y to X, originated from the effect of mutual sources (denoted as $Y_{\|X}$), is the ratio of the real part of the cross-spectrum between two channels ($real\{X(t,f)Y^*(t,f)\}$) to the power of $X(t,f)$ [123]:

$$Y_{\|X}(t,f) = real\left\{\frac{X(t,f)Y^*(t,f)}{|X(t,f)|^2}\right\} X(t,f) = real\left\{\frac{X(t,f)}{|X(t,f)|} Y^*(t,f)\right\} \hat{e}_{\|X}(t,f) \tag{4.4}$$

where $\hat{e}_{\|X}(t,f) = \frac{X(t,f)}{|X(t,f)|}$ is a unit vector in the complex plane along with $X(t,f)$, the superscript $*$ denotes the complex conjugate, $|.|$ is the absolute value operator and $real(.)$ takes the real part of a

complex number. The term $real\left\{\frac{X(t,f)}{|X(t,f)|}Y^*(t,f)\right\}$ determines the strength of $Y_{\|X}(t,f)$ alongside $X(t,f)$ in the complex plane (see Figure 4.2). The difference between $Y(t,f)$ and $Y_{\|X}(t,f)$ reflects the independent share of $Y(t,f)$ from $X(t,f)$ [123]:

$$Y_{\perp X}(t,f) = imag\left\{Y(t,f)\frac{X^*(t,f)}{|X(t,f)|}\right\}\hat{e}_{\perp X}(t,f), \tag{4.5}$$

$$\hat{e}_{\perp X}(t,f) = \frac{iX(t,f)}{|X(t,f)|} \tag{4.6}$$

where $i = \sqrt{-1}$ and $\hat{e}_{\perp X}(t,f)$ is a unit vector in the complex plane and orthogonal to the direction of X in clock-wise direction [123]. In other words, $Y_{\perp X}(t,f)$ and $X(t,f)$ are orthogonal and don't share any common information, while the pure interaction between $X(t,f)$ and $Y(t,f)$ is preserved in $Y_{\perp X}(t,f)$ and $X(t,f)$. This property of the orthogonalization process makes it useful for assessing linear correlation between power envelopes. Figure 4.2 illustrates the relationships between $X(t,f)$, $Y(t,f)$, $Y_{\perp X}(t,f)$ and $Y_{\|X}(t,f)$ (see also supplementary information of [123]).

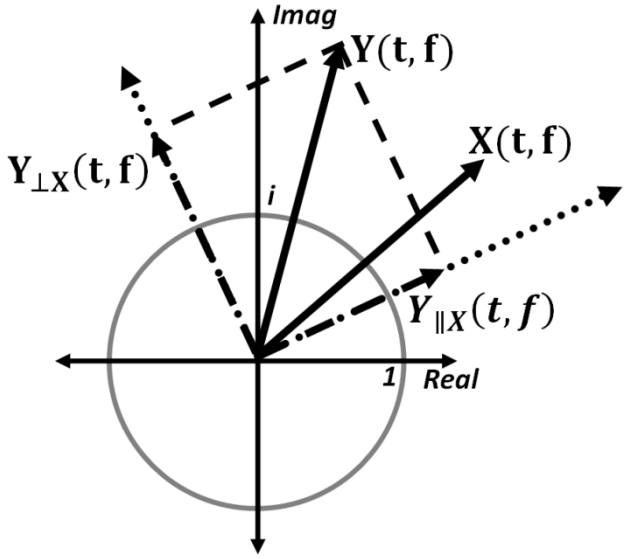

Figure 4.2: Illustration of the signal projections in the orthogonalization process (see also supplementary Information of [123]).

4.3.3 Extraction of the event-level EEG fluctuations

The SAT events (or bursts) in the newborn EEG signal have a duration of up to several seconds consisting of high frequency oscillations (>5 Hz) nested on the low frequency fluctuations (<1 Hz) [11]. A band-pass filtering applied on the signal can indirectly represent the contribution of the higher frequencies in the occurrence of SATs [128]. Since the eRSN analysis is associated with the study of event-level brain activities, the envelopes of the SAT occurrences (i.e. BAFs) were extracted at the frequency bands of interest using the Hilbert transform [128] (see also supplementary information of [10] for more details). In fact, BAF envelopes represent the temporal evolution of the EEG signal's spectral power. Frequency-specific BAF extraction was performed

using Hilbert transform within three frequency bands: 3-8 Hz, 8-15 Hz and 3-15 Hz using a set of 3rd order Butterworth filters through a zero-phase digital filtering in both the forward and backward directions (MATLAB command *filtfilt*). The first two frequency bands correspond to the fairly distinct spectral components of SAT events in the preterm EEG [11] and the latter one provides a wide view of the nested high frequency oscillations in the EEG signals. The BAF envelopes were then defined as the amplitudes of the analytic associate of the filtered EEG signals $X(t,f)$ calculated using the Hilbert transform:

$$A(t,f) = \left|X(t,f) + i\hat{X}(t,f)\right| = \sqrt{X^2(t,f) + \hat{X}^2(t,f)} \tag{4.7}$$

where $\hat{X}(t,f)$ is the Hilbert transform of $X(t,f)$ and $i = \sqrt{-1}$. Since the majority of the normalized mean power spectral density (PSD) of BAF envelopes extracted from preterm EEG signals is limited to very low frequencies (<1 Hz, see also [10]), a sampling rate of 2 Hz will be enough to preserve their information. Such significant decrease in the data sampling rate leads to a salient reduction in the computational load of further analysis. In order to alleviate the effect of mutual sources from the BAF signals, the orthogonalization method is utilized. Orthogonalized BAF envelopes are obtained through a pair-wise orthogonalization process to reduce the spurious correlation caused by the effect of volume conduction. To this end, the following process is applied on each pair of channels $x(t)$ and $y(t)$ in a multichannel EEG dataset:

(A) The channels $x(t)$ and $y(t)$ pass through a zero-phase band-pass filter within a certain frequency band Δf (e.g., 3-8 Hz) leading to the frequency-specific filtered signals $X(t,f)$ and $Y(t,f)$, respectively.

(B) The analytic associates $z_x(t,f)$ and $z_y(t,f)$ are calculated using the Hilbert transform:

$$\begin{aligned} z_x(t,f) &= X(t,f) + j\hat{X}(t,f) \\ z_y(t,f) &= Y(t,f) + j\hat{Y}(t,f) \end{aligned} \tag{4.8}$$

where $\hat{X}(t,f)$ and $\hat{Y}(t,f)$ are the Hilbert transforms of $X(t,f)$ and $Y(t,f)$, respectively.

(C) The orthogonal projections $z_{x\perp y}(t,f)$ (the component of $z_x(t,f)$ orthogonalized to $z_y(t,f)$) and $z_{y\perp x}(t,f)$ (the component of $z_y(t,f)$ orthogonalized to $z_x(t,f)$) are extracted as follows:

$$\begin{aligned} z_{x\perp y}(t,f) &= imag\{z_x(t,f)\frac{z_y^*(t,f)}{\left|z_y(t,f)\right|}\} \\ z_{y\perp x}(t,f) &= imag\left\{z_y(t,f)\frac{z_x^*(t,f)}{|z_x(t,f)|}\right\}. \end{aligned} \tag{4.9}$$

(D) The orthogonalized BAF envelopes $BAF_{x\perp y}(t,f)$ and $BAF_{y\perp x}(t,f)$ are obtained as the absolute value of the orthogonalized signals $z_{x\perp y}(t,f)$ and $z_{y\perp x}(t,f)$, respectively:

$$BAF_{x\perp y}(t,f) = \left|z_{x\perp y}(t,f)\right| \tag{4.10}$$

$$BAF_{y\perp x}(t,f) = \left|z_{y\perp x}(t,f)\right|.$$

(E) The orthogonalized BAF signals are downsampled to the sampling frequency 2 Hz.

4.3.4 Calculation of the connectivity matrices

Spatial correlation analysis using linear measures such as the Pearson product-moment correlation coefficient (PPMCC) is widely used for investigating the RSN characteristics of fMRI time series as well as EEG/MEG signals [37, 38, 121, 148, 155]. Evaluation of PPMCC is meaningful only if the joint distributions of the underlying signals follow a bivariate normal behavior [150]. On the other hand, BAF envelopes represent highly skewed, Rayleigh-like distributions [10]. Therefore, PPMCC doesn't seem a proper candidate for evaluating the pair-wise linear dependence between multichannel BAF signals. An alternative strategy would be to compute Spearman's rank-correlation coefficients [150]. However, highly asymmetric scatter plots of newborn EEG-based BAF amplitudes tending towards the near-zero (EEG background) values preclude any linear correlation analysis [10]. In fact, most of the high-amplitude values at the SAT events are simply reduced to 'outliers' by conventional linear correlation measures, while they play a significant role in the brain maturation process [11, 156]. In order to retain the contribution of the SAT occurrences during each pair-wise comparison, 19 slices were generated from the first underlying BAF signal by dividing its distribution into twenty equidistant 5% quantiles, projecting each slice on the second signal and computing the mean of all amplitude values under that slice. It led to a rescaled plot for each signal pair in which the x-axis represents the 5% steps and the y-axis represents the mean values of the second signal with respect to the slices of the first signal. The rescaling procedure converted the corresponding bivariate scatter plot to a bimodal non-linear curve which consists of a nearly flat region (low-amplitude range: 5-50%) followed by a fairly steep gradient (high-amplitude range: 70-95%) [10]. Unrealistically high amplitudes (95-100%) and very near-zero amplitudes (0-5%) were excluded from the analysis. The y-axis was also normalized with respect to the 95^{th} percentile. The i^{th} row of the connectivity matrix ($i = 1, \dots, CH$, CH: number of channels) was then filled by fitting a line within each mode of the BAF envelope of channel i and the orthogonalized BAFs of all other channels to channel i. The detailed procedure of obtaining the connectivity matrices at the individual level is as follows [10]:

(A) The BAF envelopes $BAF_i(t,f)$, $i = 1, \dots, CH$ of each subject are computed for all EEG channels according to (4.7) and form a matrix called $\mathrm{BAF(t,f)}$.

(B) For each $BAF_i(t,f)$:

a. Lower and upper bands of successive 5% slices on the amplitude distribution are estimated. It leads to 20 double-edge binary masks dividing the whole amplitude range of $BAF_i(t,f)$ into equidistant portions.

b. The BAFs of all other channels orthogonalized to $BAF_i(t,f)$ (i.e. $BAF_{j\perp i}(t,f), j = 1,\dots,CH,\ j \neq i$) are extracted based on the procedure described in Eqs. (4.8)-(4.10).

c. Mean values of the segments under $BAF_i(t,f)$'s binary masks in each orthogonalized signal $BAF_{j\perp i}(t,f), j = 1,\dots,CH,\ j \neq i$ are computed. It leads to $CH-1$ nonlinear plots representing low and high modes.

d. Two lines are fitted on the low-amplitude range (5-50%) as well as the high-amplitude range (70-95%) of each plot using linear regression and their slopes are inserted into two separate matrices.

(C) Repeating step **B** for all channels, two connectivity matrices M_{Low} and M_{High} of size $CH \times CH$ associated with low and high modes are constructed for each subject. Each map provides a non-symmetric representation of all pair-wise slopes between the reference signal $\mathrm{BAF_i(t,f)}$ and projections of other channels on this signal for a certain mode.

(D) The connectivity matrices M_{Low} and M_{High} are symmetrised by averaging the symmetric elements about the main diagonal:

$$\{M(i,j) + M(j,i)\}/2 \rightarrow M(i,j) \qquad (4.11)$$

where M is either M_{Low} or M_{High}. Note that the main diagonal elements of the connectivity matrices are set to zero throughout the analysis.

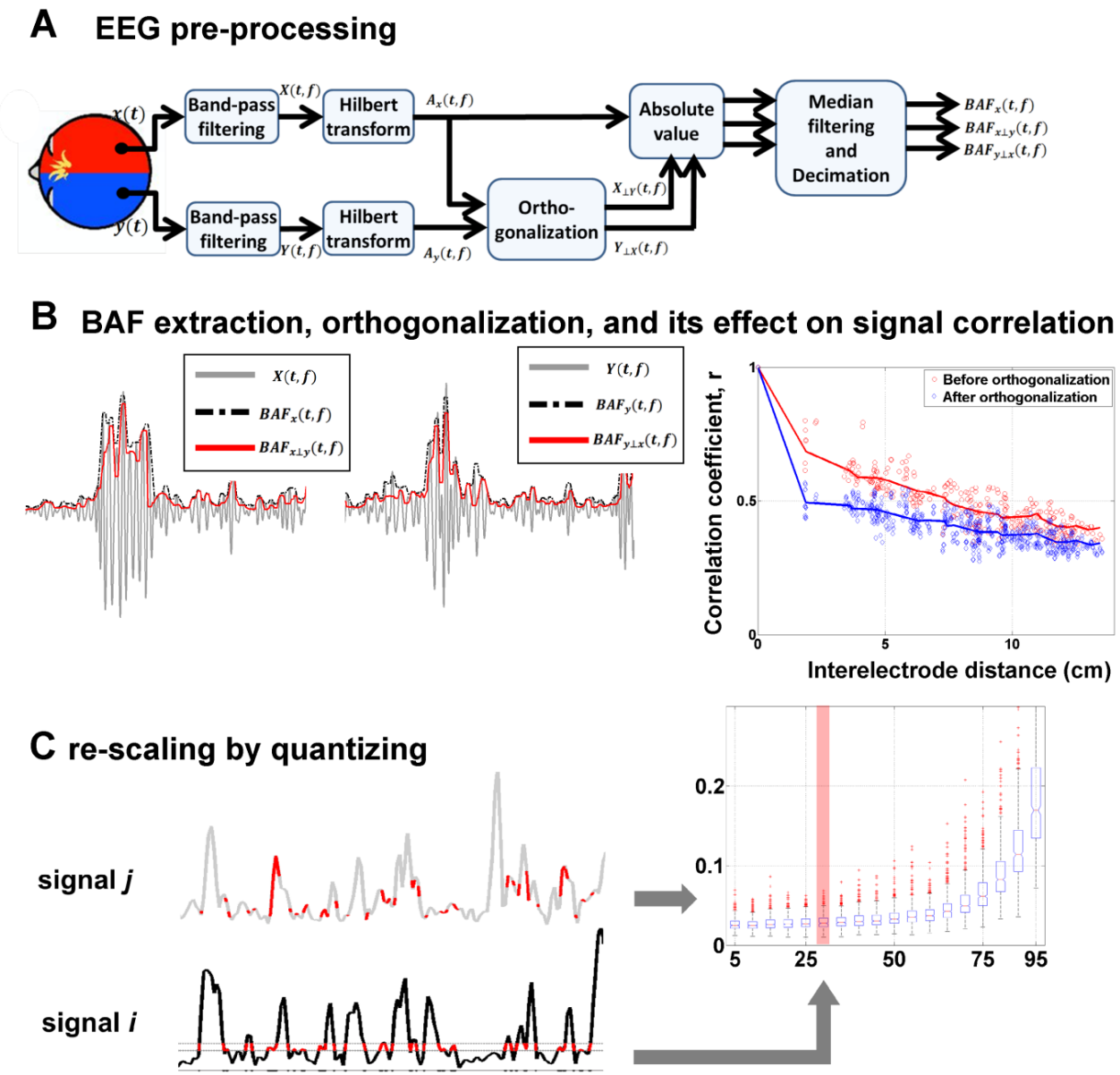

Figure 4.3: (**A**) Workflow in the preprocessing of EEG signals, (**B**) extraction of BAF traces [135] from the band-pass filtered EEG signal, and an example of BAF signal after orthogonalization (black stippled line), (**C**) comparison of spatial decay of linear amplitude correlations before [135] and after (blue) orthogonalization demonstrates that orthogonalization mainly removes the correlation at nearby electrodes.

Repeating the previous steps for all subjects in each group, $2 \times N_{subj}$ number of connectivity matrices are obtained where N_{subj} is the number of subjects in that group. In the next stage, a statistical testing will be conducted at both individual and group levels to investigate whether the connectivity matrix elements differ from the chance level [10].

Figure 4.3 demonstrates the EEG pre-processing workflow, extraction of BAF traces from a typical band-pass filtered EEG signal, and an example of BAF signal after orthogonalization. As the figure shows, comparison of spatial decay of linear amplitude correlations before and after orthogonalization demonstrates that orthogonalization mainly removes the correlation at nearby electrodes. The graph depicts Spearman correlation coefficient computed between all electrode pairs over the whole 5min EEG segment at frequency band 3-8 Hz.

4.3.5 Graph measures of eRSNs

Previous adult EEG studies have shown that EEG-based RSNs represent spatially overlapping and temporally mixing characteristics [157, 158]. This is far from what is observed in the BOLD effect-driven RSNs with spatially distinct and statistically independent behavior. Therefore, proper metrics need to be employed for investigating the dynamics of newborn eRSNs. Graph theoretical measures seem to be suitable candidates as they are widely used for quantifying the structural features of complex networks, such as those extracted out of multichannel EEG datasets [157-159]. To this end, each EEG channel (or fMRI's ROI) was considered as a node in the network and the pair-wise linear regression slopes between this node and other nodes were taken as its connected edges (see Figure 4.4). This is a common procedure which has been recently used in older children and adults studies [123, 132, 157, 160-162].

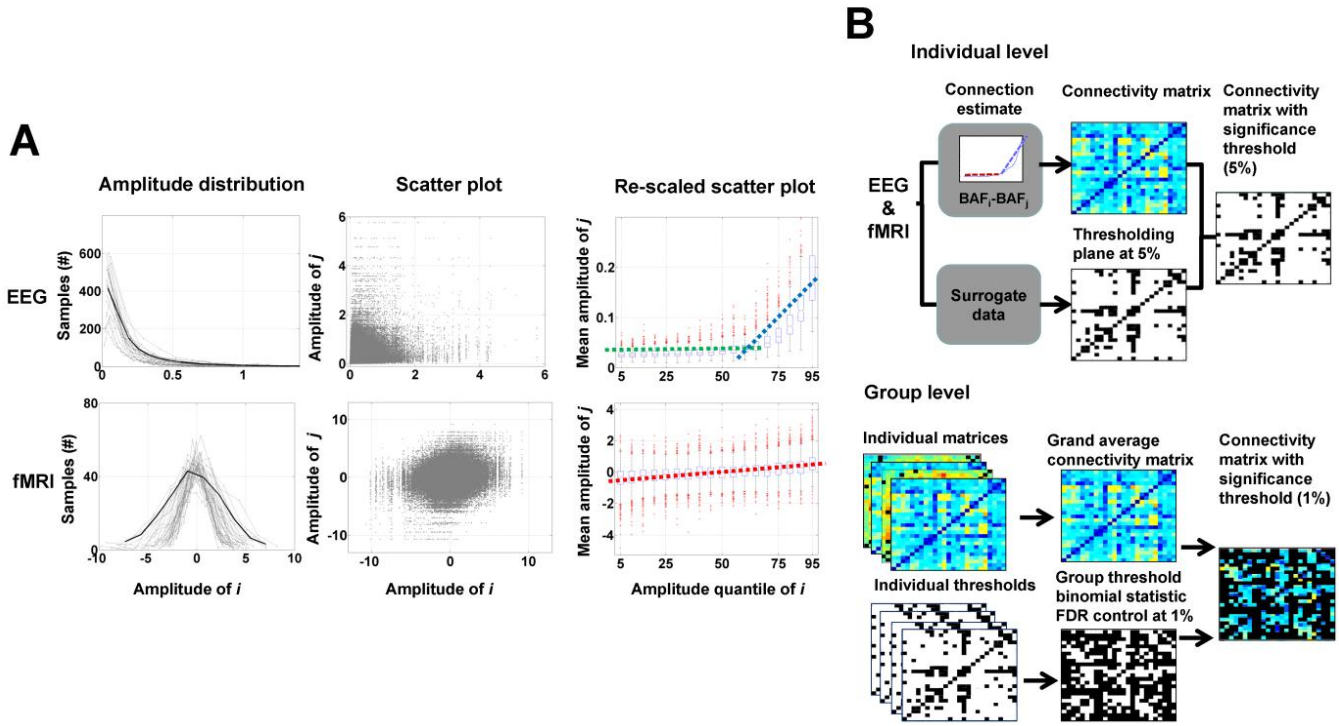

Figure 4.4: (A) amplitude distributions, scatter plots and re-scaled scatter plots of a preterm newborn EEG dataset and a typical fMRI time series. As panels suggest, a clear bimodality is observed for the EEG signals, while the fMRI signals represent unimodal behavior. (B) Detailed components of the eRSN analysis block in Figure 4.1 at the individual and group levels.

For the eRSN analysis described in this chapter, the weighted measures of clustering coefficient (CC), path-length and the Optimal Community Structure and Modularity (OCSM) were computed using freely available Brain Connectivity Toolbox [163]. The weighted clustering coefficient expresses the weighted likelihood that neighbors of a given node are connected. Averaging CC over all nodes results in an average, whole brain, weighted CC that reflects the level of local organization of the network. Average weighted CC was also examined separately from the precentral and postcentral brain regions to see if there is any structural difference between the occipital and frontal networks (see also [36, 164]). Global network's communication capacity was assessed by computing the weighted characteristic path length [19], namely a path for which summation of its inverse link weights is minimized. Network modularity - a key feature in early network development – was evaluated by computing OCSM [163, 165] quantifying the degree to what extent the network has been subdivided into clearly delineated sub-networks. Finally, small worldness (S = CC/PL; see [132]) was assessed to investigate whether this aspect is emerging in the brain at early ages of life. Before computing group level statistics or comparisons between groups, all graph measures were normalized at individual level through dividing the absolute graph value by the mean of 50 surrogate values obtained from random shuffling of the given network [132]. The normalization procedure facilitates a fair comparison between individuals, between modes and across age groups.

4.3.6 Thresholding and statistical analysis

In order to evaluate the significance of a phenomenon in a signal through hypotheses testing, many realizations of the null hypothesis with the same statistical similarities to the original signal are generated; while an appropriate set of features have been removed from it. To eliminate linear dependencies between EEG-BAF signals, one can shuffle the order of time samples or phase information [166]. In the case of spatial correlation analysis using EEG power signals, however, the shuffled BAF envelopes are too different from the original signals and may cause high false positive/negative error rates in the pair-wise comparisons. Therefore, surrogate connectivity measures were generated by keeping one signal (i.e. $BAF_i(t,f)$) in the electrode pair and time-shifting of the other one (i.e. $BAF_{j\perp i}(t,f)$) by 6 s steps (i.e. 1:50 of the whole 300-s signal) leading to 49 surrogates for a 300 s continuous BAF envelope. Then, the null distribution for statistical testing within each mode was constructed by computing the linear regression slopes between each BAF envelope and all time-shifted versions of each orthogonalized BAF envelope. Finally, a three-dimensional array of the size $CH \times CH \times 49$ was obtained under this scenario at each mode and its 95^{th} percentiles along the third dimension built a $CH \times CH$ thresholding map for each subject. The individual connectivity matrices were then thresholded with this 95% significance level. An averaging over subjects in each group (either healthy or IVH) gave two thresholded connectivity matrices for that group which represented all possible pair-wise grand mean slopes between channels for each mode. We also used 'reorder_matrix' function in Brain Connectivity Toolbox [163] to re-arrange the matrices such that their elements are squeezed around the main diagonal using a version of simulated annealing.

For connectivity analysis at the group level, a pool of binary masks was constructed based on the thresholded individual connectivity matrices and a binomial testing at the 5% probability of success. The pool can be considered as a gray-level matrix in which each element shows the number of successes for its corresponding electrode pair over all subjects. To minimize the error rates of multiple binomial comparisons ($CH \times (CH-1)/2$ simultaneous tests), false discovery rate (FDR) controlling at 5% level was applied leading to a group-level binary mask for thresholding the grand average of individual connectivity matrices. Another comparison was also conducted between two groups at high mode using pair-wise Wilcoxon rank sum test and FDR controlling at 5% significance level. Comparison between two modes at each group was also done using pair-wise two-sided sign tests at the same significance level. Figure 4.5 shows the schematic procedure of surrogate data generation for the eRSN analysis.

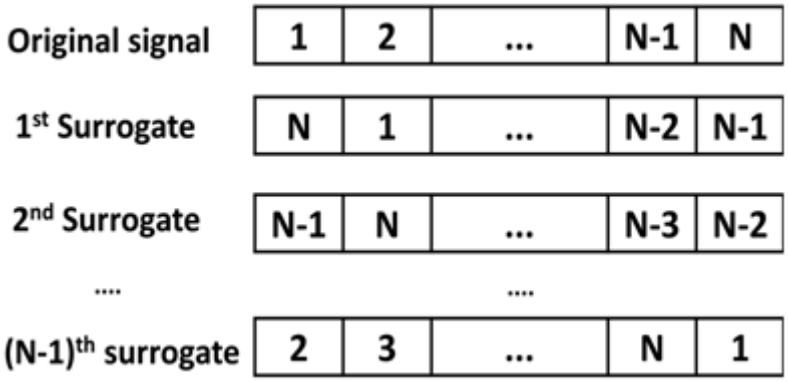

Figure 4.5: Generation of time shifting surrogates by splitting the signal into N segments ($N = 50$) and shifting one segment at a time from the end to the start of the signal. This yields 49 surrogate signals with temporal structure shifted but otherwise identical with the original signal (see also [128]).

4.3.7 Testing of global similarity with Mantel test

Mantel test [167] was used for assessing global similarity of connectivity matrices between the two age groups (preterm vs. fullterm) and functional modes (low vs. high). The test evaluates similarity of two matrices by measuring pair-wise relationships of matrix elements. The test is commonly used in ecology for estimating distances, for instance, between species and organisms [168]. Given two distance matrices X and Y with the diagonals filled with zero, the test statistic r is based on the cross-product of the matrix elements:

$$r = \frac{1}{n-1}\sum_{i=1}^{n}\sum_{j=1}^{n}\frac{(X_{ij}-\mu_X)}{\sigma_X}\frac{(Y_{ij}-\mu_Y)}{\sigma_Y} \tag{4.12}$$

where $n = N_{CH}(N_{CH}-1)/2$ is the number of elements in the distance matrices. Similar to other product-moment coefficients, r ranges from -1 to 1, and with larger number of elements (>40), r can be transformed to t statistic, as was done in the analysis of this chapter.

4.4 Results and discussion

This section represents the results of the proposed eRSN analysis on brain development as well as IVH abnormality assessment. The concept of newborn EEG bimodality is also investigated by conducting two experiments.

4.4.1 Bimodal functionality: a genuine behaviour of newborn EEG-BAFs

It is known that the amplitude distribution of a complex random variable with normal real and imaginary parts follows a Rayleigh distribution [169]. Since the BAF envelopes are generated by taking the amplitude of complex analytical signals, one may ask if their Rayleigh-like distributions arise from the adopted computational procedure only. To make sure that bimodality of newborn

EEG signals are their built-in behavior, two sets of experiments were conducted using random noise processes as well as randomized newborn EEG signals. In the first experiment, a uniformly distributed pseudorandom signal with 21 channels and 1200 samples (similar length with the down-sampled 5-min BAFs) was generated and underwent exactly the same procedure of EEG-BAF extraction. It was checked if the computational process imposes a bimodal nonlinear shape on the rescaled plot of random signals similar to what is observed for the BAF envelopes of each healthy preterm baby. As Figure 4.6-A illustrates, the rescaled traces are quite flat with no modality distinction. In the second experiment, it was tested if bimodality of the BAF envelopes is a subject-free feature and independent from the arrangement of EEG electrodes. A pool of single-channel BAFs was produced from EEG channels of all healthy preterm babies (length of 1200 samples, 11 subjects times 21 channels in total) and 21 channels were drawn from this pool randomly. The randomized multichannel EEG signal was then fed into the BAF extraction process (Figure 4.3) and the rescaled connectivity plots were obtained (see Figure 4.6-A). As the figure suggests, again the dominant trend of the plots is completely flat. It is therefore concluded that the bimodal behavior of healthy preterm newborn EEG datasets appears through the nature of the signals as well as the interconnections governing them. The most left panels of Figure 4.6-B depict the BAF amplitude histograms of all single channels for two typical EEG datasets from the healthy preterm group and the group of preemies with IVH. The general morphology of two sets of histograms is quite similar. It is also confirmed by the most right panel which shows the grand mean root mean squared estimates of two groups. However, the eRSN analysis results in the following sections can represent a clear difference between healthy preterms and preemies with IVH. This is also the case for the groups of healthy fullterms versus healthy preterms as well as newborn EEG signals versus fMRI time series (see also Figure 4.4).

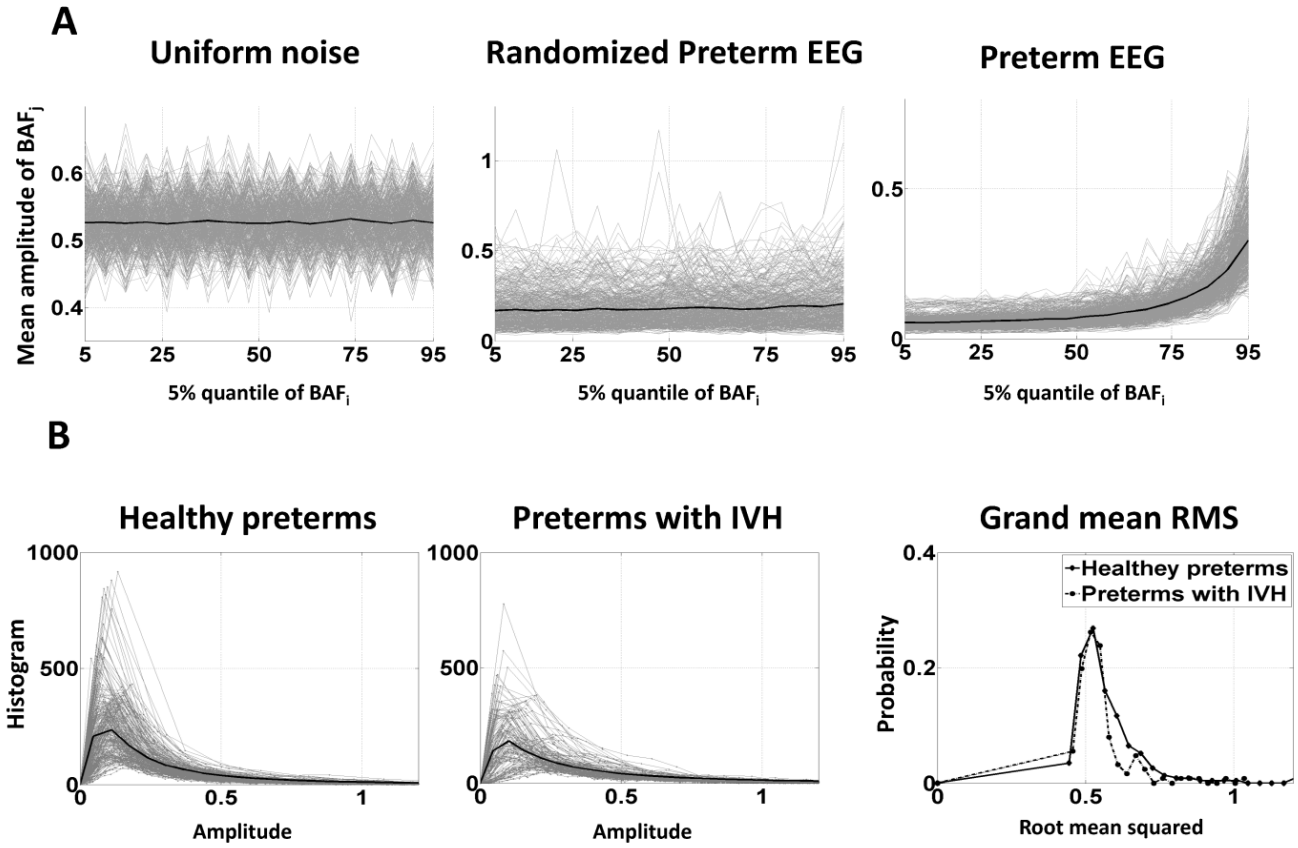

Figure 4.6: (**A**-from left to right) comparison of re-scaled scatter plots of a multichannel uniform noise, a randomized multichannel preterm EEG signal and a normal preterm EEG dataset. All signals contain 21 channels and 1200 samples. (**B**-from left to right) comparison of the BAF amplitude histograms and grand mean root mean squared estimates of healthy preterms and preemies with IVH.

4.4.2 Bimodality and newborn brain networks

In analogy to the adult EEG studies (e.g.; [121, 147]), BAF amplitudes at distinct frequency bands were obtained through a combined procedure of band-pass filtering and Hilbert transform (see Figure 4.3). This was done for BAFs within a broad frequency band (3-15Hz), as well as by using narrower frequency bands (3-8 Hz and 8-15 Hz) that were previously shown to represent relatively independent oscillations within SAT activity (see also [128]), the main component of high amplitudes in the proposed eRSN analysis. Figure 4.7 suggests that frequency spectra of BAF signals can be down-sampled at 4 Hz while still conveying its full time-domain behavior (see also [128]). Analysis of epoch durations after segmenting the EEG signals into low and high modes showed that over 80% of all epochs lasted more than 250 ms, and more than half of the epochs lasted more than 500 ms.

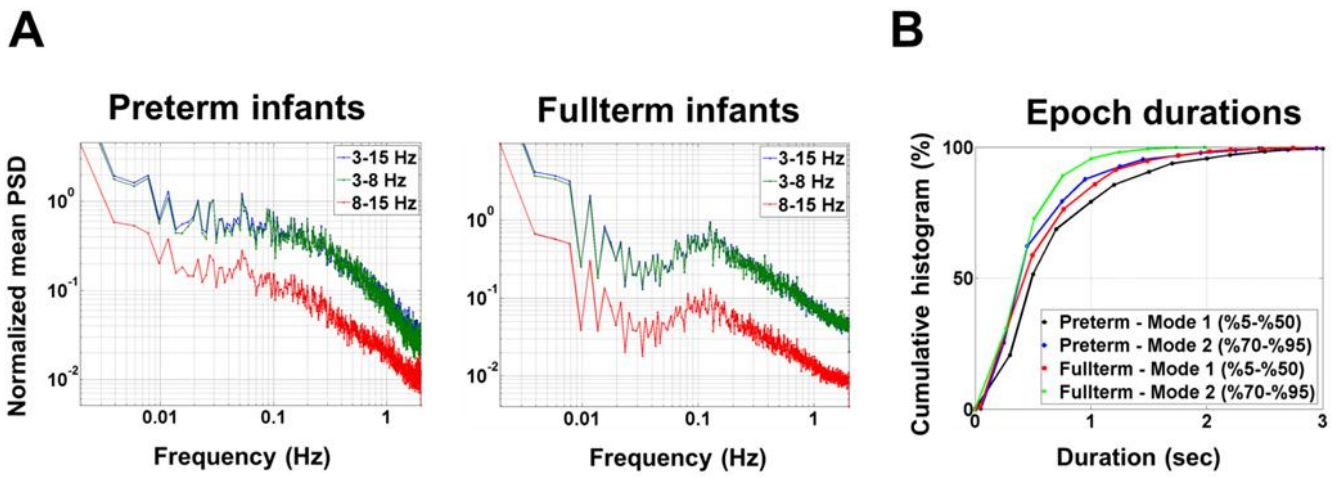

Figure 4.7: (**A**) Normalized mean power spectral density (PSD) of BAF signals in healthy preterm and full-term babies. (**B**) Durations of low and high modes in both age groups.

The common method in analyzing functional connectivity within or between different RSNs is based on computing pair-wise linear (Pearson product-moment) correlation coefficients between two fMRI time series or EEG/MEG power envelopes (also termed seed-ROI based correlation analysis), followed by group statistics using Fisher r-to-z-transformation [155]. This procedure builds on the assumption that the samples are comparable, independent, and belong to a bivariate normal distribution. None of these is the case with neonatal BAF signals where distributions are highly asymmetric with long tails towards higher amplitudes (see Figure 4.4 and Figure 4.6), resembling the Rayleigh distributions typically seen in power time series. Formal testing with Kolmogorov-Smirnov also confirmed non-normality of BAF distributions (K-S 0.51, $p<0.01$), while the rs-fMRI time series exhibited reasonably normal distribution (K-S 0.13; $p=0.09$). The heavy clustering of low amplitude values seen in the EEG-derived BAF scatter plots (Figure 4.4) implies an unavoidable bias in linear correlation analyses. A straightforward technical rejection of high amplitude values as "outliers" was precluded by the prior neurophysiological knowledge that the high values represent genuine and developmentally crucial brain activity, the SAT events [11, 128]. Therefore, the possibility of non-linear spatial relationships between BAF signals across the amplitude scale was tested. To test this hypothesis, the amplitude in each BAF signal pair was quantized into 20 quantiles (5% cumulative percentiles each). Inspection of such re-scaled scatter plots (Figure 4.4) suggests that the linear relationship between BAF amplitudes is negligible at the lower amplitude range (hereafter called "low mode": percentiles 5-50%), while there is a steep relationship at the upper amplitude range (hereafter called "high mode"; percentiles 70-95%). In full agreement with the prior neurophysiological literature [5-7, 17], this finding implies that functional network connectivity in the newborn brain is expressed as two different modes of neuronal communication with significantly different degree of amplitude dependence. A comparison of all available BAF signal pairs (25 channels, i.e. 300 comparisons in each baby) demonstrated that

bimodality in spatial correlations of this kind seemed to be a nearly global feature (Figure 4.8 and Figure 4.9).

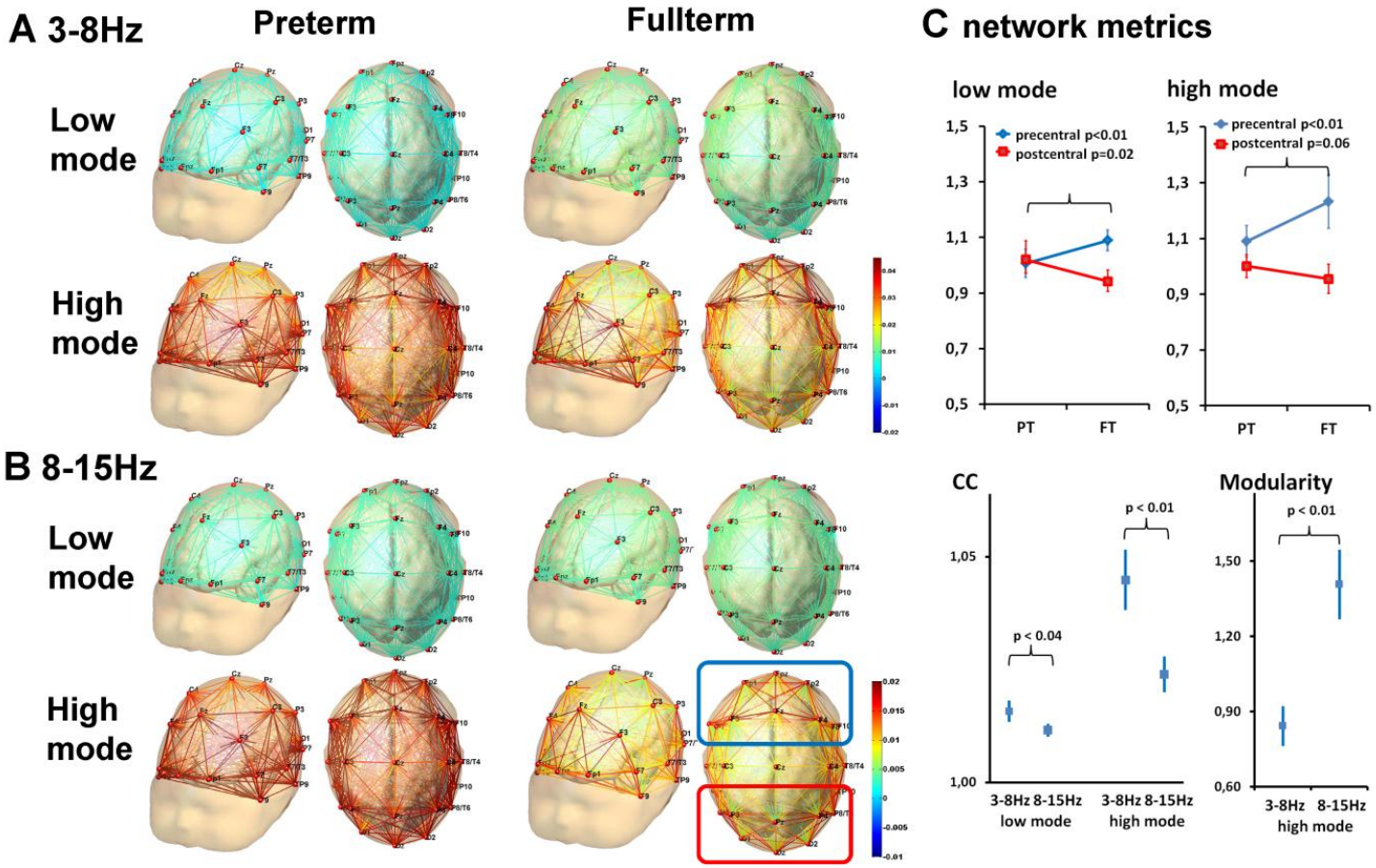

Figure 4.8: Topological visualization and metrics of emerging eRSN. A and B: The three-dimensional visualization of analysis of connectivity demonstrates a robust difference between activity modes, and suggests a developmental organization during late gestation at both lower (3-8 Hz; A) and higher (5-18 Hz; B) frequency oscillations. Each link between nodes depicts the connection strength, and the graphs within each frequency band are shown at the same scale. Note the virtual absence of networks in the low modes, the apparently random connectivity in the high activity mode in the preterm babies, as well as the visually conspicuous frontally and occipitally prominent clustering in the high activity mode in the fullterm newborns. The blue and red squares in the lower right figure depict the group of precentral (blue) and postcentral [135] nodes used in the spatial comparison in section C of this figure. (C) Graph analysis of network structure shows salient spatially selective developmental trajectories. Average clustering (CC) increases in the precentral and decreases in the postcentral areas, and it is stronger at lower frequencies, however is significantly stronger at the higher frequencies.

Strikingly, such bimodality was not observed in the fMRI data, which showed a remarkably monotonic, linear correlation across all amplitudes (Figure 4.4) and between all rs-fMRI time series (see Figure 4.9 including the results of the frequency band 3-8 Hz). Low mode activity in the electric domain (eRSN) shows very low levels of correlations, which dramatically increase when the brain shifts into high activity mode. The difference between modes is statistically significant in nearly all cells of both age groups. Notably, similar analysis with rs-fMRI demonstrates much less significant correlations and hardly any different between high and low regimes.

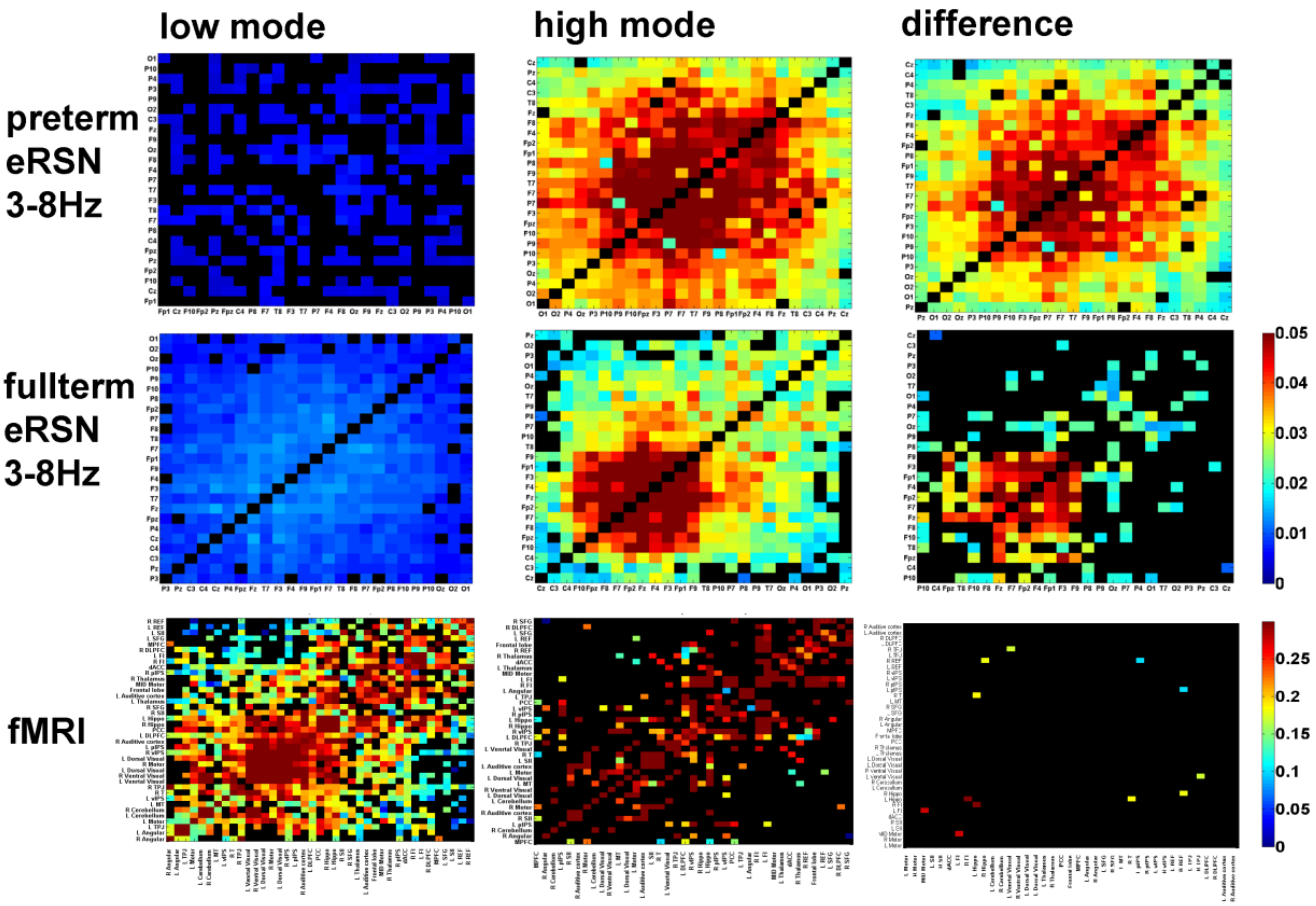

Figure 4.9: Group average of connectivity matrices demonstrate robust differences between low and high activity modes.
Each element in the connectivity matrix shows the grand average magnitude (slope) of linear relationships across the whole subject group, and the non-significant cells (at group level) are depicted with black cells.

Matrices are reorganized using a method based on simulated annealing to aid visual interpretation [163]. Figure 4.10 illustrates the results of the other two frequency bands 8-15 Hz and 3-15 Hz. Note how the overall finding is similar (see also Figure 4.9) at all frequencies, with the clear increase in connectivity strength in high mode, and clear statistical difference between modes. Notably, difference between modes is more widespread in the preterm babies.

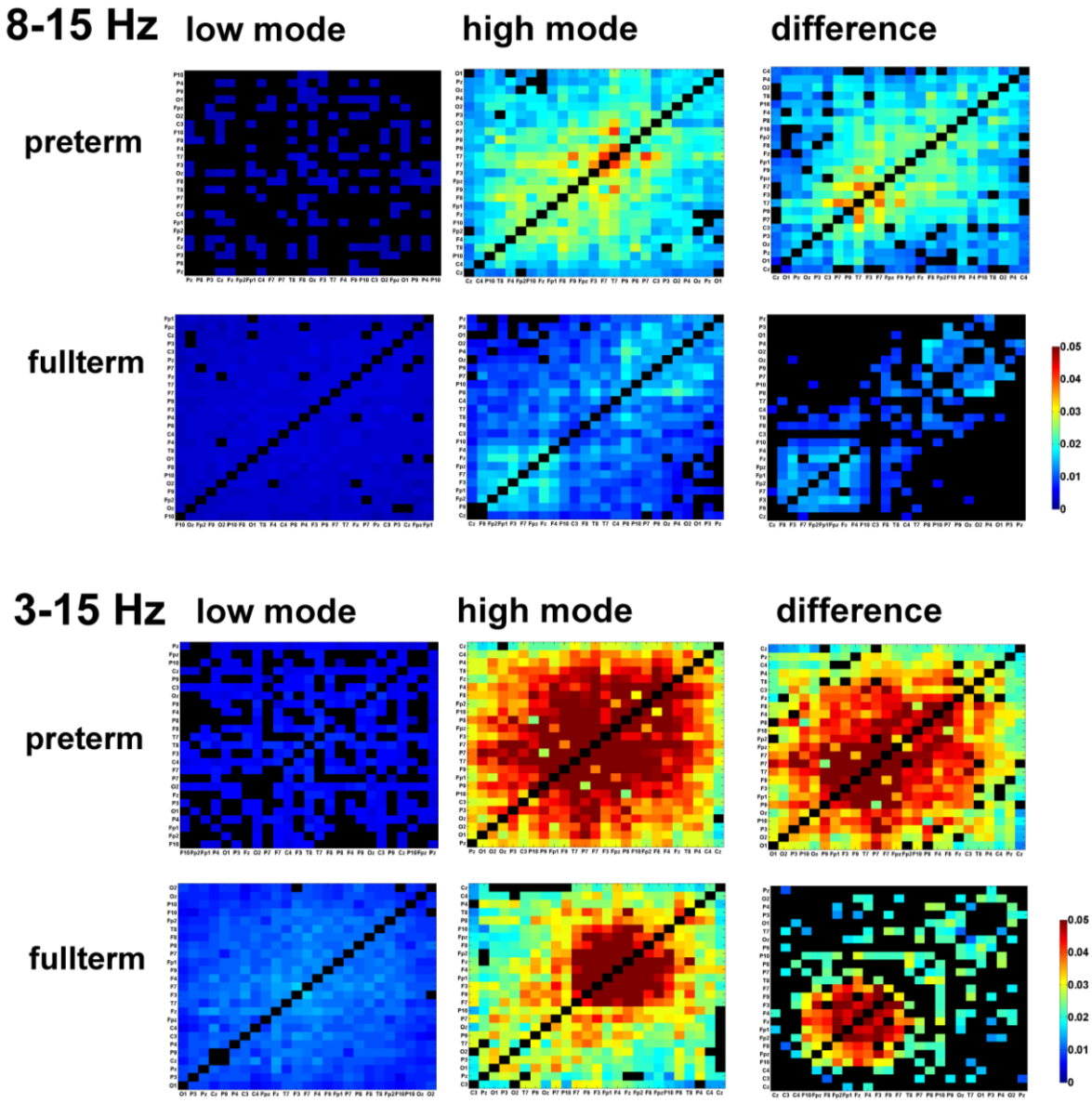

Figure 4.10: Comparison of connectivity matrices at the higher (8-15 Hz) and broad (3-15 Hz) frequency bands. The matrices have een thresholded (black cells) to show only those links that exceed statistical threshold at the group level (see Figure 4.4-B). For visual clarity, the matrices are reorganized using a method based on simulated annealing to squeeze the matrix elements along the main diagonal which results in somewhat different ordering of rows (channels/ROIs) between matrices [163].

In order to test whether the observed correlations are statistically significant, a conservative testing approach was employed using surrogate signals generated by repeated (*n=49*) time shifting of the same data. This procedure allows testing the null hypothesis that any BAF or fMRI signal with the given temporal behavior would give rise to comparable relationships between amplitudes, and group level testing using binomial statistics yielded connectivity matrices where each pair-wise relationship could be tested individually.

4.4.3 Comparison of low and high modes

The results revealed a significant difference between low and high modes of newborn eRSNs (Figure 4.8, Figure 4.9 and Figure 4.10). A detailed, pair-wise comparison of connectivity matrices showed that the levels of amplitude relationship were significantly higher in almost every signal pair during high mode activity (Figure 4.9 and Figure 4.10). Global assessment of similarity between connectivity matrix patterning indicated an overall change from low to high modes in the preterm infants (Mantel statistics -0.32; $p=0.99$), while the overall pattern was stable across modes in the fullterm babies (Mantel statistics 0.55; $p<0.01$). These observations are fully compatible with the existing idea [5-7, 9] that network communication in the preterm brain predominately relies on the bursts (or SATs) that are represented as the high mode in the analysis presented in this chapter.

4.4.4 Development of bimodality

The early development of network activity is thought to begin with the developmentally unique, intermittent activity patterns (i.e. the high mode) that will be gradually replaced by the continuous EEG oscillations [17]. Conceivably, this developmental trajectory should also be reflected in the spatial EEG correlations when the fetus develops from the preterm to fullterm age. Assessing next EEG recordings from ten fullterm newborns gave the possibility of studying developmental window that is characterized by a massive growth of long-range brain connections [170], hence providing the physical framework to support large scale neuronal interactions.

The results showed that the difference between low and high modes is markedly reduced when the babies approach full term age (Figure 4.9), however one third of the signal pairs (34%; at 3-15 Hz) still showed a significantly higher amplitude relationships during the high mode. Such developmental reduction of bimodality is fully compatible with the idea that the nearly silent periods (low mode) of early brain activity will become replaced by the more organized ongoing spontaneous activity near term age [17, 171]. A significant change in global patterning of connectivity was only seen in the low activity mode (Mantel test -0.14, $p=0.93$; high mode 0.57, $p<0.01$), which is compatible with the idea that the spontaneous brain activity during low mode (i.e. inter-SATs) undergoes a significant qualitative, spatial organization towards fullterm age [8, 172].

4.4.5 Spatial topology of correlated EEG activity

The spatial topology of the pair-wise signal correlations was then explored in more detail using a graph theoretical approach [163, 173]. This aimed to characterize differences in spatial network organization between low and high activity modes, and how they develop during the last months of pregnancy. To this end, the nodes in the network graphs were represented by the electrodes and the

links were defined by the strength association between the nodes, the slope of linear relationship. The graph metrics were rendered comparable between age groups by normalizing them using surrogate graphs, The network metrics within the dominant 3-8 Hz frequency band were firstly studies [8, 20, 128, 171].

As a first measure of local spatial eRSN organization, the normalized weighted clustering coefficients (CC) were compared between age groups. It was found that the CC measure during high mode is significantly increased during development (preterm: 1.02±0.01 (SD) vs. fullterm: 1.04±0.02; $p=0.001$). In addition, fullterm babies showed a significant increase in CC when they shifted from low to high activity mode (1.02±0.01 vs 1.04±0.02, $p<0.01$). The normalized characteristic path-length, however, was not significantly changed during development or between activity modes. Functional modularity was measured with the metric Optimal Community Structure and Modularity (OCSM) to assess presence of clearly delineated sub-networks within the brain [163]. Despite of the substantial difference in connectivity levels between activity modes (Figure 4.8), modularity was found to be comparable between low and high modes within both age groups (preterm: low mode 0.41±0.04 versus high mode 0.58±0.10, $p=0.19$; fullterm low mode 0.70±0.09 versus high mode 0.84±0.07, $p=0.29$). However, there was a significant developmental increase in modularity in both activity modes (low mode: preterm 0.41±0.04 vs. fullterm 0.70±0.09, p=0.01; high mode: 0.58±0.10 vs.0.84±0.07, $p=0.04$, Wilcoxon). Finally, evidence of small-worldness was searched as a proxy of shifting from random towards more ordered networks [163]. While there was no developmental change, small-worldness showed a trend-level increase in the fullterm brain when shifting from low to high activity mode ($p=0.07$).

While the above analyses are all global network measures, there is ample anatomical and functional evidence indicating a developmental fronto-occipital gradient [36, 91, 164]. Hence, potential topological differences in network clustering (CC) between pre-central and post-central regions were examined. It was found that pre-central CC increases while post-central CC decreases during late fetal development in both activity modes (Figure 4.8). A pre-centrally emphasized CC was also seen in the pair-wise comparisons (high mode: both preterm $p<0.04$ and fullterm $p<0.01$; low mode: fullterm $p<0.01$; Wilcoxon test). Finally, the pre-central CC was significantly increased in both age groups when they shifted from the low to high activity modes ($p<0.01$, Wilcoxon test). These findings together are strikingly compatible with the notion of distinct developmental trajectories, and in particular a protracted developmental window of frontal brain areas in humans [170].

4.4.6 eRSN at different frequency bands

Prior studies in adults have shown that long range correlations in the electric brain activity may take place at a wide range of oscillatory frequencies, but they exhibit frequency-specific spatial patterning [121-123, 147, 148]. Prior work on neonatal EEG has reported spatial differences and developmental changes [8, 171, 172] in the frequency composition of early bursts/SATs. Therefore, it was examined whether eRSN could be frequency-specific by repeating all above analyses after first filtering the EEG signal into two frequency bands (3-8 Hz and 8-15 Hz) that cover functionally independent oscillatory entities within the SATs [128, 171]. It was found that a functional bimodality can be observed at all frequencies in a qualitatively comparable manner (Figure 4.9 and Figure 4.10).

A detailed network analysis with graph metrics, however, revealed frequency-related differences. In contrast to the 3-8 Hz frequency band, the higher 8-15 Hz frequency band showed no differences in the mean CC between activity modes or between brain areas. Compared to the 3-8Hz frequency band, however, modularity at 8-15 Hz was more dynamic, and it was found to increase from low to high mode in both age groups (fullterm 0.67 ±0.08 vs. 1.41±0.13, $p<0.01$; preterm 0.34±0.05 vs. 0.85±0.15, $p<0.03$). There was also a significant developmental increase in modularity at both low and high activity modes ($p=0.01$ and 0.02, respectively). These shifts from relatively random to modular structures consisting of anterior and posterior network entities can be clearly observed in the weighted graph images in Figure 4.10.

4.4.7 Absence of bimodality in the newborn rs-fMRI data

Earlier studies have reported consistent and robust RSN in newborns using rs-fMRI [36-38], which as a method implicitly assumes a linear correlation between two signals. In the present analysis procedure, such linear correlation over the whole amplitude range means no difference between higher and lower amplitudes, i.e. 'unimodality' in the amplitude relationship (see also the rescaled scatter plots in Figure 4.4). Due to the lack of prior studies exploring how spatial fMRI correlations depend on instantaneous amplitudes (to the best of the author's knowledge), it is possible that bimodality of this kind has only been ignored because of the widely used analysis procedures. In light of the EEG observations reported in this chapter, it was hence aimed to see if the network correlations in the newborn fMRI time series are genuinely linear, or could they potentially exhibit such bimodality that was seen in the electric brain activity. As expected from the inspection of scatter plots of raw fMRI time series, the re-scaled fMRI time series showed a clear linear relationship and no evidence of inflection of the regression line at the upper amplitude range akin to that seen with BAF signals (Figure 4.4). Moreover, a statistical comparison of lower and higher

amplitude quantiles (5-50% and 70-95%) confirmed the visual observation: There were very few (0.9%; 7 out of 741 comparisons) pair-wise differences in regression slopes between lower and higher amplitude ranges in each signal pair, constituting a strong case against bimodality in the amplitude relationships between newborn rs-fMRI time series.

4.4.8 eRSNs of healthy preterms and preemies with IVH abnormality

The proposed eRSN analysis approach was conducted on the EEG database of 6 newborns with IVH and the results were compared with the outcome of 11 healthy preterms. Figure 4.11, Figure 4.12 and Figure 4.13 illustrate grand mean connectivity matrices and 3D maps of EEG electrodes at 3-8 Hz, 3-15 Hz and 38-15 Hz frequency bands, respectively. Each element in the connectivity matrices shows the grand average magnitude (slope) of linear relationships across the whole subject group, and the non-significant cells (at group level) are have been blacked out.

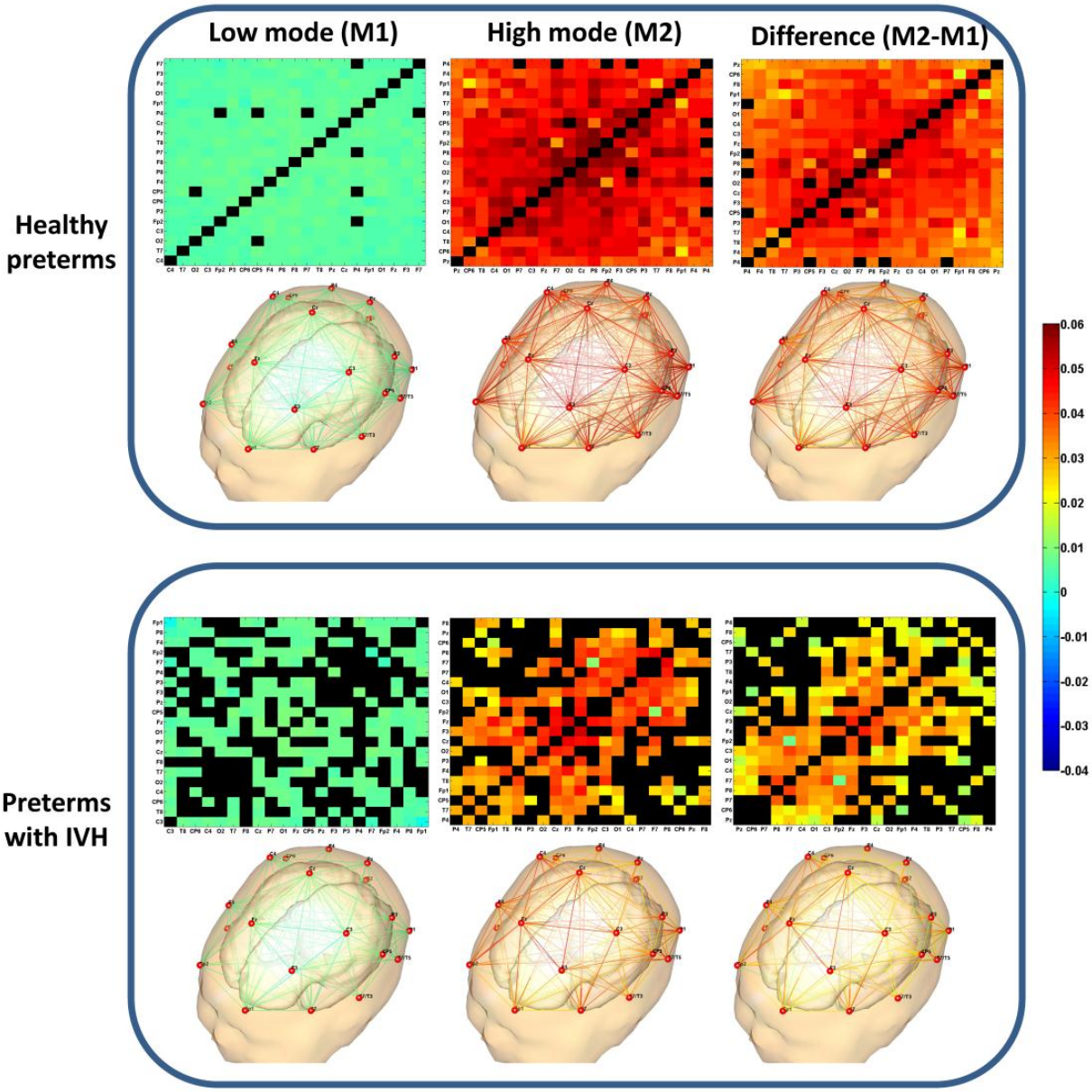

Figure 4.11: grand mean connectivity matrices and 3D maps of EEG electrodes at 3-8 Hz for the group of healthy preterms and preterms with IVH.

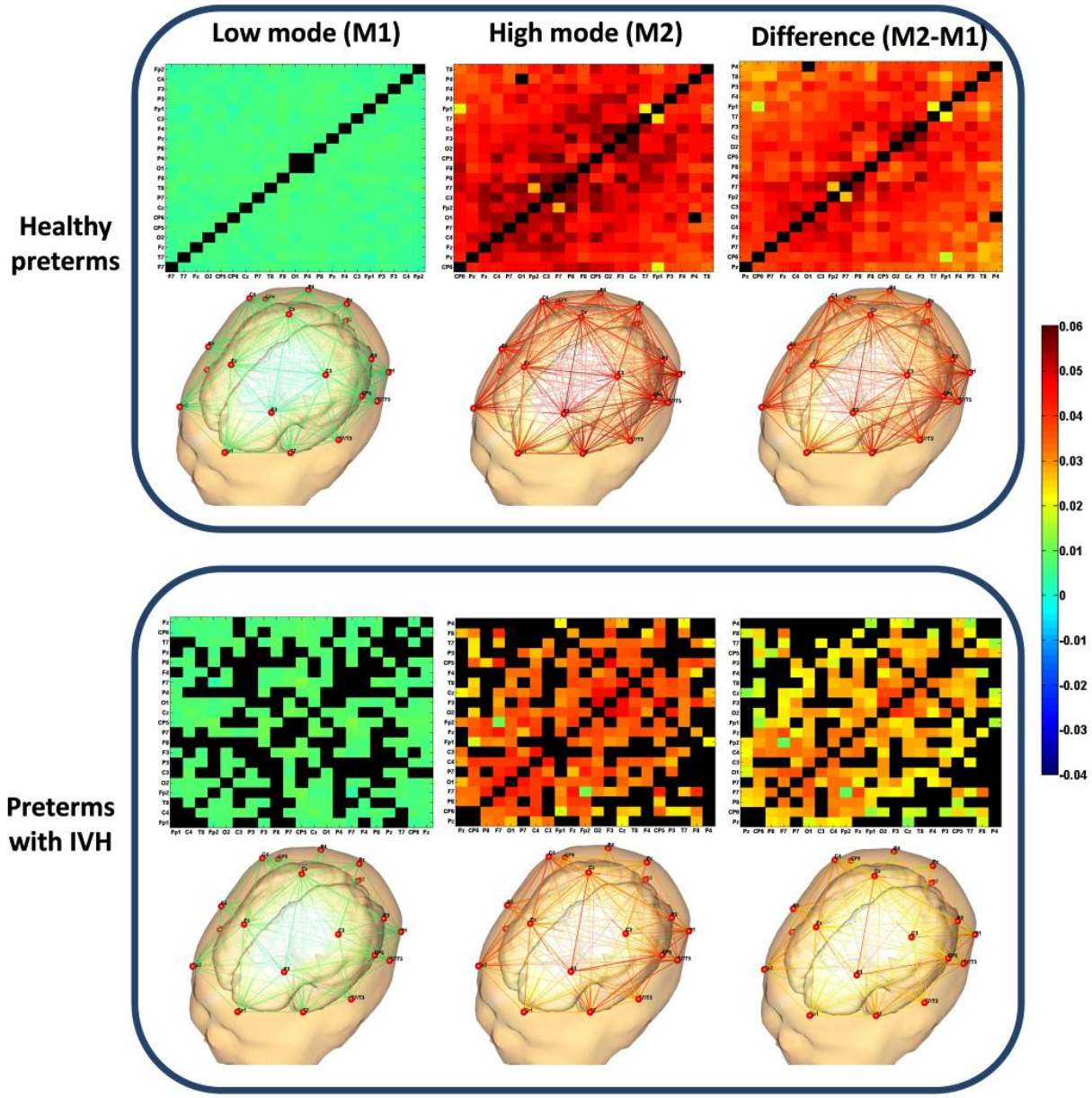

Figure 4.12: grand mean connectivity matrices and 3D maps of EEG electrodes at 3-15 Hz for the group of healthy preterms and preterms with IVH.

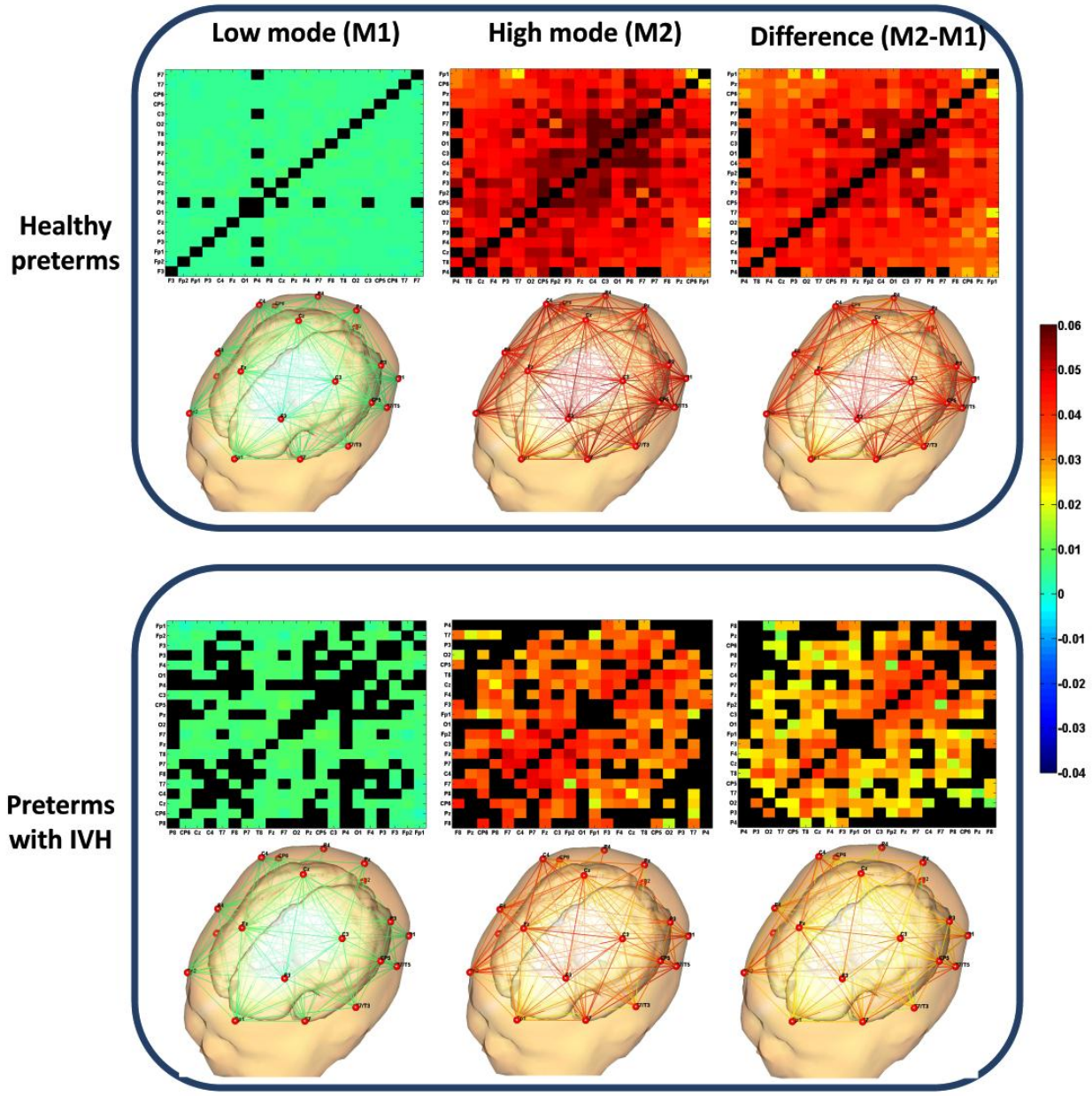

Figure 4.13: grand mean connectivity matrices and 3D maps of EEG electrodes at 8-15 Hz for the group of healthy preterms and preterms with IVH.

Figure 4.14, Figure 4.15 and Figure 4.16 represent high modes of two groups at three frequency bands and the difference map between them after backing out insignificant pairs. Box plots of the WD measures extracted from two groups are also illustrated in the figures.

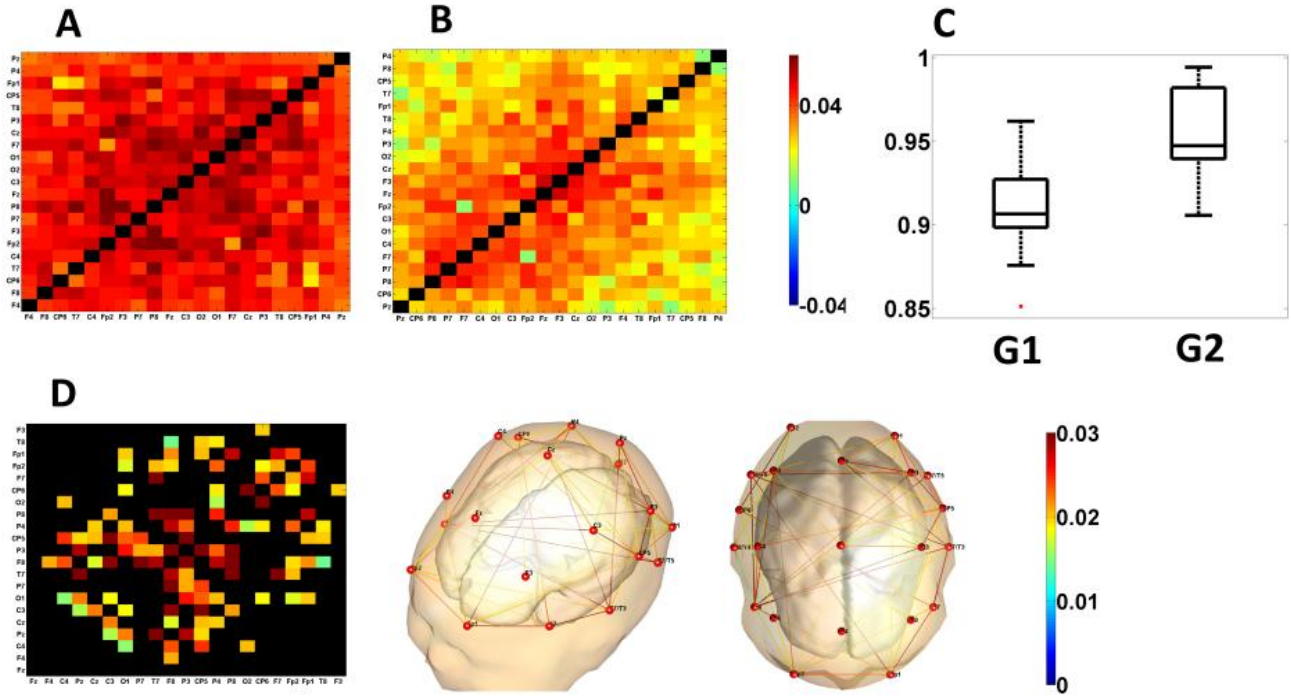

Figure 4.14: Comparison between healthy and IVH groups (G1 vs. G2) at 3-8 Hz. **A** and **B**: original (weighted) connectivity matrices of healthy babies and babies with IVH, respectively, **C**: statistical comparison of weight dispersion values extracted from two groups, **D**: difference map between two groups. Insignificantly different cells have been blacked out.

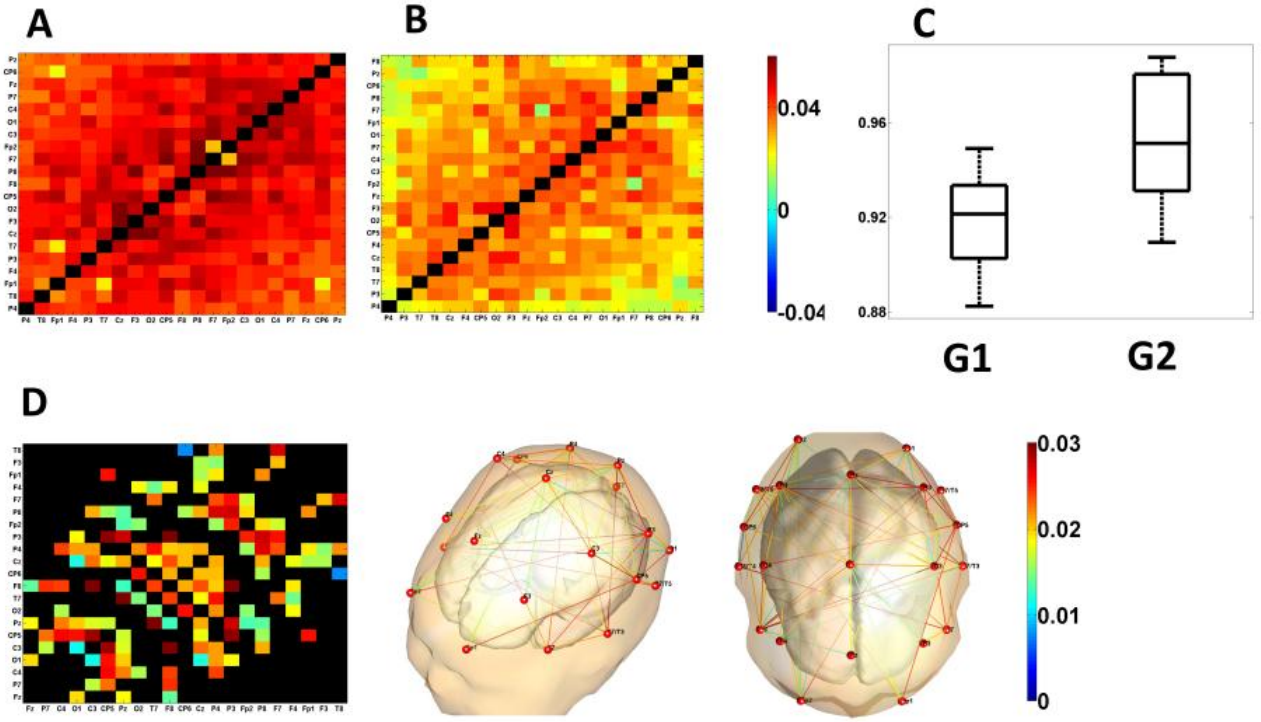

Figure 4.15: Comparison between healthy and IVH groups (G1 vs. G2) at 3-15 Hz. **A** and **B**: original (weighted) connectivity matrices of healthy babies and babies with IVH, respectively, **C**: statistical comparison of weight dispersion values extracted from two groups, **D**: difference map between two groups. Insignificantly different cells have been blacked out.

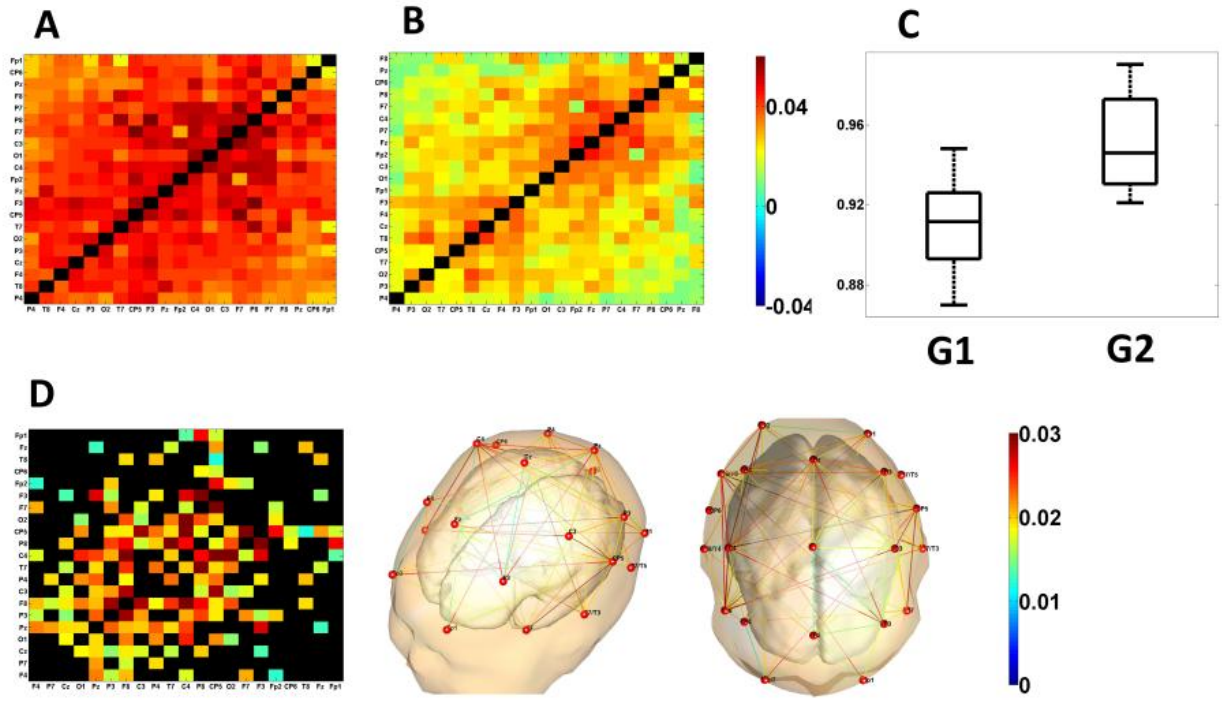

Figure 4.16: Comparison between healthy and IVH groups (G1 vs. G2) at 8-15 Hz. **A** and **B**: original (weighted) connectivity matrices of healthy babies and babies with IVH, respectively, **C**: statistical comparison of weight dispersion values extracted from two groups, **D**: difference map between two groups. Insignificantly different cells have been blacked out.

Based on the statistical analysis on the graph characteristics of connectivity matrices at two modes (high/low) and two groups (healthy/IVH), weight dispersion of eRSN networks in the group of healthy preterms was significantly lower ($\alpha = 5\%, p < 0.05$, Wilcoxon test) than the IVH group at high mode for three frequency bands. Increased weight dispersion (WD) in the group of babies with IVH implies that normal brain maturation is shifted towards more random functional networks in presence of IVH abnormality. Functional integration, quantified by shortest path length (PL) measure, significantly reduces in EEG high mode of healthy preterm babies compared to low mode at 3-15 Hz and 8-15 Hz frequency bands ($\alpha = 5\%, p < 0.05$, Wilcoxon test). No meaningful difference was observed between shortest PL extracted from the eRSNs of two modes for IVH group. It suggests that functional integration is less developed within the eRSNs of IVH group in contrast to the healthy infants. For both groups, the OCSM measure significantly increased from low mode to high mode at 3-15 Hz and 8-15 Hz bands suggesting that IVH may not have an important impact on the modularity of eRSNs. In other words, the degree to which eRSNs may be subdivided into separate modules does not statistically change with IVH.

4.5 Summary and conclusions

This chapter aimed to investigate spatial relationships between cortical areas of the newborn brain by analyzing linear correlations between power time series of the EEG signals. Due to the inherent

nature of neonatal EEG signals, a novel analysis framework was developed and the findings were compared with comparable characteristics of fMRI time series obtained from other cohort of newborns.

The spatial characteristic of eRSNs was studied through frequency-specific EEG fluctuations. The BAF envelopes of each subject were extracted for all EEG channels using Hilbert transform after band-pass filtering to a desired frequency band. A non-uniform segmentation was performed based on amplitude percentiles, and the pair-wise linear relationships between channels were computed. It led to a symmetric connectivity map (i.e. matrix) for each subject representing the amplitude correlations between EEG signals. To characterize the behavior of eRSNs during the brain maturation process, the proposed analysis paradigm was applied on all subjects in two EEG datasets of healthy babies (preterm, $N_1 = 10$ and fullterm, $N_2 = 11$) as well as a healthy fullterm fMRI database ($N_3 = 18$). In addition, the effects of IVH abnormality on eRSNs were explored by comparing the group of healthy preterms and a group of preterm infants with IVH ($N = 6$). Statistical significances at individual and at group levels were calculated using surrogate data method. Finally the connectivity matrices were evaluated using different graph measures.

The results suggested that two functionality modes can be observed in the spatial correlations in the preterm EEG datasets, and this dichotomic behavior fades towards fullterm age. Specifically, the preterm brain exhibits periods of “low mode” (low amplitude) without meaningful spatial correlations, and “high modes” (high amplitudes) with robust brain wide correlations. No bimodal functionality was detected in the fullterm fMRI time series. IVH group showed significantly higher weight dispersion in contrast to the healthy preterm suggesting that normal brain maturation is shifted towards more random functional networks in presence of IVH abnormality. It was also inferred from the shortest PL measure that functional integration is less developed within the eRSNs of IVH group in contrast to the healthy infants.

In conclusion, this chapter provides evidence of a dichotomic behavior of early developing brain networks, which as a concept is fully in line with the recently established ideas about early neuronal functions. It also shows that such behavior is not observed in the fMRI signal, which calls for a need to revisit the idea of a direct relationship between fMRI signal and neuronal activity. The significant impact of IVH on the preterm eRSNs can be used as a basis for developing EEG-based diagnosis tools for this brain abnormality.

Chapter 5

Conclusions and perspectives

5.1 Thesis summary

In this thesis, a novel methodology for analyzing cortical connectivity using scalp EEG was developed and its applications to newborn brain abnormality assessment were explored. The proposed approach accounts for three aspects of neonatal scalp EEG recordings: time-varying behavior, directional relationships between channels and frequency-specific fluctuations of amplitudes. This approach has the potential to lead to a more comprehensive insight into the interactions between the different newborn EEG channels when signals are represented in a joint time-frequency domain. In this way, a narrower perspective of the problem of newborn EEG connectivity analysis and relevant methods was avoided. Two types of newborn EEG abnormalities including EEG seizures and intra-ventricular hemorrhage (IVH) in conjunction with the connectivity between different EEG channels were investigated. The impact of IVH on the neonatal RSNs was studied using groups of healthy and sick babies. The proposed paradigm of electric resting state network (eRSN) analysis in this thesis revealed a bimodal functionality within the networks of cortical regions, gradually attenuating during the brain maturation process. The analysis also found a significantly higher level of generalized phase synchrony during periods of neonatal EEG seizure.

This research has made both theoretical and application-specific contributions to newborn scalp EEG assessment and connectivity analysis in the form of three novel methods:

- The first method, measuring GePS as discussed in Chapter 2, allows for the assessment of generalized phase synchrony within non-stationary multichannel signals in the time-frequency domain and provides a basis for quantifying global phase disruptions within newborn scalp EEG signals during ictal periods.

- The second method, discussed in Chapter 3, is based on a modified time-frequency version of the classical PDC function (called gOPDC) for estimating the partial and directed information flow between scalp EEG signals by taking the effect of volume conduction into consideration. The analysis of directional dependency within newborn EEG channels was based on the

assumption that multichannel EEG signals follow the general form of multivariate autoregressive (MVAR) models driven by Gaussian noise inputs. The appropriateness of this assumption was evaluated by studying propagation patterns of flash light-evoked EEG responses in a population of healthy term infants. The proposed method brings a key new perspective in effectively tackling the troublesome effect of volume conduction at the scalp level.

- The third method (discussed in Chapter 4) was the evaluation of functional bimodality within the eRSNs of the newborn brain during development as well as in the presence of IVH. Although the extent of IVH in the preterm brain can be accurately delineated by ultrasound imaging, its functional consequences are more likely associated with background and epileptiform EEG abnormalities. However, there is still disagreement over the capacity of scalp EEG monitoring as guidance for effective treatment of IVH and its complications. This study applied the proposed eRSN paradigm to EEG recordings of a group of healthy preterm babies and another group of preterm babies with IVH to measure cortical functional connectivity between the frequency-specific BAFs computed from scalp EEG signals. Whilst the EEG power envelopes of the two groups conveyed visually similar signatures, the underlying eRSNs were strikingly different. Distinctive characteristics of the neonatal eRSNs were found that differentiated preterm and term EEG.

5.2 Main conclusions

Using several simulations with feature dimensions relevant to neonatal EEG activity, it was shown that the proposed connectivity measures (i.e., GePS, and gOPDC) can quantify time-varying interactions in the joint time-frequency domain. These new metrics, along with the proposed paradigm of eRSN analysis, may provide a basis for development of diagnostic/prognostic non-invasive brain monitoring tools in NICUs. For example, the eRSN analysis may help to estimate the proper time of ventricular drainage during post-IVH ventricular dilatation in order to reduce the potential risk of further brain damage caused by increased ventricular pressure. Another example would be the potential use of the proposed GePS assessment method for newborn EEG seizure characterization. Prospectively, a combined outcome of the proposed connectivity methods during the first weeks after birth could be useful for predicting long-term neurological outcomes.

The development, implementation and evaluation of the algorithms in this thesis have led to several major conclusions as follows:

A. Generalized phase synchrony based on the level of cointegration between EEG phase signals increases significantly during neonatal ictal periods. This finding could be adapted to assist in characterizing and/or grading neonatal EEG seizures.

B. The effect of volume conduction affecting the newborn scalp EEG connectivity analysis can be mitigated by incorporating the ideas of orthogonalization at the level of MVAR coefficients and the imaginary part of the coherence function.

C. In line with fMRI studies, long-range spatial correlations are observed within the eRSNs of the newborn brain at both preterm and term ages.

D. Unlike the fMRI time series, BAFs of the newborn EEG signals behave in a bimodal manner alternating between a low mode of background activity and a high mode of spontaneous activity transients. This bimodality attenuates with brain maturation and in the presence of IVH.

E. Graph analysis of the eRSNs on two age groups (preterm/term) reveals a shift from random towards more ordered networks in healthy babies. In particular, during late fetal development there is a tendency for fronto-occipital gradients and nodes in the cortical networks to cluster together.

F. The group of preterms with IVH shows significantly higher weight dispersion in contrast to the healthy preterm suggesting that normal brain maturation is shifted towards more random functional networks in presence of IVH abnormality.

5.3 Suggestions for future work

There is plenty of room for research on newborn EEG abnormality assessment and connectivity analysis identified when developing the framework of this thesis. Areas for future work include:

- Improving the performance of the GePS measures in terms of time resolution to detect sub-second changes in EEG signals. This calls for non-parametric estimation of cointegrating relationships between multivariate phase signals without using MVAR models, which are known to have limitations in tracking fast changes in short-length time traces. Multichannel EMD methods also constitute a potential alternative to one dimensional EMD utilized in this study.

- Developing an integrated newborn EEG assessment system for NICUs by unifying different aspects of early brain dynamics and binding various features of neonatal EEG abnormalities together. A wide variety of clinical situations at different age conditions, ranging from

asymmetry, asynchrony, burst-suppression, neonatal seizures and clinical situations including IVH, periventricular leukomalacia and hypoxic-ischaemic and infective brain injury are known to be linked with later neuro-developmental disability. Further exploration of the EEG features in the outcome prediction of these abnormalities is needed. This system would have further application in defining the course of normal functional brain development, a step required before the development and clinical trialing of non-invasive interventions aimed at neonatal neurorehabilitation.

- There is no consensus among neurophysiologists on how to precisely define the morphology of bursts and inter-burst intervals in a single-channel EEG recording and its normal/abnormal situations in connection to the other channels. This yields a highly subjective diagnostic paradigm taken by EEG experts for evaluation of some newborn EEG abnormal patterns such synchrony/asynchrony or symmetry/asymmetry at certain ages. More rigorous mathematical descriptions of newborn EEG abnormalities with respect to the global features over the channels are required.

References

[1] K. Mevel, G. Telat, F. Eustache, and B. Desgranges, "The Default Mode Network in Healthy Aging and Alzheimer's Disease," *Int J Alzheimers Dis,* vol. 2011, 2011.

[2] J. J. Riviello, "Pediatric EEG Abnormalities," in *The Clinical Neurophysiology Primer,* A. Blum and S. Rutkove, Eds., ed: Humana Press, 2007, pp. 179-204.

[3] B. Boashash, *Time frequency signal analysis and processing: a comprehensive reference* Amsterdam; Boston: Elsevier, 2003.

[4] B. Boashash, G. Azemi, and J. M. O'Toole, "Time-Frequency Processing of Nonstationary Signals: Advanced TFD Design to Aid Diagnosis with Highlights from Medical Applications," *IEEE Signal Process Mag,* vol. 30, pp. 108-119, 2013.

[5] M. Colonnese and R. Khazipov, "Spontaneous activity in developing sensory circuits: Implications for resting state fMRI," *Neuroimage,* vol. 62, pp. 2212-2221, 2012.

[6] I. L. Hanganu-Opatz, "Between molecules and experience: role of early patterns of coordinated activity for the development of cortical maps and sensory abilities," *Brain Res Rev,* vol. 64, pp. 160-176, 2010.

[7] A. G. Blankenship and M. B. Feller, "Mechanisms underlying spontaneous patterned activity in developing neural circuits," *Nat Rev Neurosci,* vol. 11, pp. 18-29, 2010.

[8] W. Jennekens, H. J. Niemarkt, M. Engels, J. W. Pasman, C. van Pul, and P. Andriessen, "Topography of maturational changes in EEG burst spectral power of the preterm infant with a normal follow-up at 2 years of age," *Clin Neurophysiol,* vol. 123, pp. 2130-2138, 2012.

[9] W. Kilb, S. Kirischuk, and H. J. Luhmann, "Electrical activity patterns and the functional maturation of the neocortex," *Eur J Neurosci,* vol. 34, pp. 1677-1686, 2011.

[10] A. Omidvarnia, P. Fransson, M. Metsäranta, and S. Vanhatalo, "Functional Bimodality in the Brain Networks of Preterm and Term Human Newborns," *Cereb Cortex,* doi: 10.1093/cercor/bht120 2013.

[11] S. Vanhatalo, J. M. Palva, S. Andersson, C. Rivera, J. Voipio, and K. Kaila, "Slow endogenous activity transients and developmental expression of K+-Cl- cotransporter 2 in the immature human cortex," *Eur J Neurosci,* vol. 22, pp. 2799-2804, 2005.

[12] G. L. Holmes and C. T. Lombroso, "Prognostic Value of Background Patterns in the Neonatal EEG," *J Clin Neurophysiol,* vol. 10, pp. 323-352, 1993.

[13] B. J. Fisch, *Fisch & Spehlmann's EEG primer: Basic principles of digital and analog EEG*. Amsterdam: Elsevier, 2005.

[14] C. T. Lombroso, *Neonatal EEG polygraphy in normal and abnormal newborns. In Electroencephalography. Basic Principles, Clinical Applications and Related Fields*. Baltimore, Md, USA: Williams and Wilkins, 1993.

[15] CommitteeOnFetusAndNewborn, "American Academy of Pediatrics: Age Terminology During the Perinatal Period," in *Pediatrics* vol. 114, ed, 2004, pp. 1362-1364.

[16] K. Palmu, "Automatic detection of spontaneous activity transients in preterm electroencephalography," Licentiate of Science, Department of Biomedical Engineering and Computational Science, Aalto University School of Science, Helsinki, Finland, 2013.

[17] S. Vanhatalo and K. Kaila, "Development of neonatal EEG activity: from phenomenology to physiology," *Semin Fetal Neonatal Med,* vol. 11, pp. 471-478, 2006.

[18] K. J. Friston, "Functional and effective connectivity in neuroimaging: A synthesis," *Hum Brain Mapp,* vol. 2, pp. 56-78, 1994.

[19] M. D. Lamblin, M. André, M. J. Challamel, L. Curzi-Dascalova, A. M. d'Allest, E. De Giovanni, *et al.*, "Électroencéphalographie du nouveau-né prématuré et à terme. Aspects maturatifs et glossaire," *Clin Neurophysiol,* vol. 29, pp. 123-219, 1999.

[20] K. Palmu, S. Wikström, E. Hippeläinen, G. Boylan, L. Hellström-Westas, and S. Vanhatalo, "Detection of 'EEG bursts' in the early preterm EEG: visual vs. automated detection," *Clin Neurophysiol,* vol. 121, pp. 1015-1022, 2010.

[21] A. Omidvarnia, M. Mesbah, M. S. Khlif, J. M. O'Toole, P. Colditz, and B. Boashash, "Kalman filter-based time-varying cortical connectivity analysis of newborn EEG," presented at the Conf Proc IEEE Eng Med Biol Soc (EMBS), Boston, MA, USA, 2011.

[22] A. Omidvarnia, M. Mesbah, J. M. O'Toole, P. Colditz, and B. Boashash, "Analysis of the time-varying cortical neural connectivity in the newborn EEG: A time-frequency approach," presented at the IEEE Workshop Statist Sig Process Appl (WOSSPA), Algeria, 2011.

[23] B. Biswal, F. Zerrin Yetkin, V. M. Haughton, and J. S. Hyde, "Functional connectivity in the motor cortex of resting human brain using echo-planar mri," *Magn Reson Med,* vol. 34, pp. 537-541, 1995.

[24] P. Fransson, B. Skiöld, S. Horsch, A. Nordell, M. Blennow, H. Lagercrantz, *et al.*, "Resting-state networks in the infant brain," *Proc Natl Acad Sci U S A,* vol. 104, pp. 15531-15536, 2007.

[25] M. D. Fox and M. E. Raichle, "Spontaneous fluctuations in brain activity observed with functional magnetic resonance imaging," *Nat Rev Neurosci,* vol. 8, pp. 700-711, 2007.

[26] D. Zhang and M. E. Raichle, "Disease and the brain's dark energy," *Nat Rev Neurol,* vol. 6, pp. 15-28, 2010.

[27] J. S. Damoiseaux, S. A. R. B. Rombouts, F. Barkhof, P. Scheltens, C. J. Stam, S. M. Smith, *et al.*, "Consistent resting-state networks across healthy subjects," *Proc Natl Acad Sci U S A,* vol. 103, pp. 13848-13853, 2006.

[28] D. H. Weissman, K. C. Roberts, K. M. Visscher, and M. G. Woldorff, "The neural bases of momentary lapses in attention," *Nat Neurosci,* vol. 9, pp. 971-978, 2006.

[29] P. Fransson, "How default is the default mode of brain function?: Further evidence from intrinsic BOLD signal fluctuations," *Neuropsychologia,* vol. 44, pp. 2836-2845, 2006.

[30] M. Boly, E. Balteau, C. Schnakers, C. Degueldre, G. Moonen, A. Luxen, *et al.*, "Baseline brain activity fluctuations predict somatosensory perception in humans," *Proc Natl Acad Sci U S A,* vol. 104, pp. 12187-12192, 2007.

[31] R. Kluetsch, C. Schmahl, I. Niedtfeld, M. Densmore, V. Calhoun, J. Daniels, *et al.*, "ALterations in default mode network connectivity during pain processing in borderline personality disorder," *Arch Gen Psychiatry,* vol. 69, pp. 993-1002, 2012.

[32] Y. I. Sheline, D. M. Barch, J. L. Price, M. M. Rundle, S. N. Vaishnavi, A. Z. Snyder, *et al.*, "The default mode network and self-referential processes in depression," *Proc Natl Acad Sci U S A,* vol. 106, pp. 1942-1947, 2009.

[33] C. J. Lynch, L. Q. Uddin, K. Supekar, A. Khouzam, J. Phillips, and V. Menon, "Default Mode Network in Childhood Autism: Posteromedial Cortex Heterogeneity and Relationship with Social Deficits," *Biol Psychiatry,* vol. 74, pp. 212-9, 2013.

[34] M. D. Greicius, B. Krasnow, A. L. Reiss, and V. Menon, "Functional connectivity in the resting brain: A network analysis of the default mode hypothesis," *Proc Natl Acad Sci USA,* vol. 100, pp. 253-258, 2003.

[35] P. Fransson, "Spontaneous low-frequency BOLD signal fluctuations: an fMRI investigation of the resting-state default mode of brain function hypothesis," *Hum Brain Mapp,* vol. 26, pp. 15-29, 2005.

[36] P. Fransson, M. Metsäranta, M. Blennow, U. Aden, H. Lagercrantz, and S. Vanhatalo, "Early Development of Spatial Patterns of Power-Law Frequency Scaling in fMRI Resting-State and EEG Data in the Newborn Brain," *Cereb Cortex,* vol. 23, pp. 638-46, 2012.

[37] V. Doria, C. F. Beckmann, T. Arichi, N. Merchant, M. Groppo, F. E. Turkheimer, *et al.*, "Emergence of resting state networks in the preterm human brain," *Proc Natl Acad Sci U S A,* vol. 107, pp. 20015-20020, 2010.

[38] C. D. Smyser, T. E. Inder, J. S. Shimony, J. E. Hill, A. J. Degnan, A. Z. Snyder, *et al.*, "Longitudinal Analysis of Neural Network Development in Preterm Infants," *Cereb Cortex,* vol. 20, pp. 2852-2862, 2010.

[39] J. L. Y. Cheong and L. W. Doyle, "Increasing rates of prematurity and epidemiology of late preterm birth," *J Paediatr Child Health,* vol. 48, pp. 784-788, 2012.

[40] S. Beck, D. Wojdyla, L. Say, A. P. Betran, M. Merialdi, J. H. Requejo, *et al.*, "The worldwide incidence of preterm birth: a systematic review of maternal mortality and morbidity," *Bull World Health Org,* vol. 88, p. 31, 2010.

[41] Li Z, McNally L, Hilder L, and Sullivan EA, "Australia's Mothers and Babies 2009," Australian Institute of Health and Welfare, Sydney, Australia2011.

[42] Li Z, Zeki R, Hilder L, and Sullivan EA, "Australia's mothers and babies 2010," Australian Institute of Health and Welfare, Canberra, Australia2012.

[43] G. Ball, L. Srinivasan, P. Aljabar, S. J. Counsell, G. Durighel, J. V. Hajnal, *et al.*, "Development of cortical microstructure in the preterm human brain," *Proc Natl Acad Sci U S A,* vol. 110, 2013.

[44] Chiara Nosarti, Abraham Reichenberg, Robin M. Murray, Sven Cnattingius, Mats P. Lambe, Li Yin, *et al.*, "Preterm birth and psychiatric disorders in young adult life," *Arch Gen Psychiatry,* vol. 69, pp. 610-617, 2012.

[45] B. H. Walsh, D. M. Murray, and G. B. Boylan, "The use of conventional EEG for the assessment of hypoxic ischaemic encephalopathy in the newborn: A review," *Clin Neurophysiol,* vol. 122, pp. 1284-1294, 2011.

[46] W. Deburchgraeve, P. J. Cherian, M. De Vos, R. M. Swarte, J. H. Blok, G. H. Visser, *et al.*, "Neonatal seizure localization using PARAFAC decomposition," *Clin Neurophysiol,* vol. 120, pp. 1787-1796, 2009.

[47] H. Bassan, "Intracranial Hemorrhage in the Preterm Infant: Understanding It, Preventing It," *Clin Perinatol,* vol. 36, pp. 737-762, 2009.

[48] J. Dauwels, F. Vialatte, T. Musha, and A. Cichocki, "A comparative study of synchrony measures for the early diagnosis of Alzheimer's disease based on EEG," *Neuroimage,* vol. 49, pp. 668-693, 2010.

[49] K. J. Blinowska, R. Kusacute, and M. Kaminacuteski, "Granger causality and information flow in multivariate processes," *Phys Rev E,* vol. 70, p. 050902, 2004.

[50] F. Mormann, K. Lehnertz, P. David, and C. E. Elger, "Mean phase coherence as a measure for phase synchronization and its application to the EEG of epilepsy patients," *Physica D,* vol. 144, pp. 358-369, 2000.

[51] J. P. Lachaux, E. Rodriguez, J. Martinerie, and F. J. Varela, "Measuring phase synchrony in brain signals," *Hum Brain Mapp,* vol. 8, pp. 194-208, 1999.

[52] M. G. Rosenblum and A. S. Pikovsky, "Detecting direction of coupling in interacting oscillators," *Phys Rev E,* vol. 64, p. 045202, 2001.

[53] M. G. Rosenblum, L. Cimponeriu, A. Bezerianos, A. Patzak, and R. Mrowka, "Identification of coupling direction: Application to cardiorespiratory interaction," *Phys Rev E,* vol. 65, p. 041909, 2002.

[54] T. Koenig, D. Lehmann, N. Saito, T. Kuginuki, T. Kinoshita, and M. Koukkou, "Decreased functional connectivity of EEG theta-frequency activity in first-episode, neuroleptic-naïve patients with schizophrenia: preliminary results," *Schizophr Res,* vol. 50, pp. 55-60, 2001.

[55] D. Looney, C. Park, P. Kidmose, M. Ungstrup, and D. P. Mandic, "Measuring phase synchrony using complex extensions of EMD," presented at the IEEE Workshop Statist Sig Process, Cardiff, UK, 2009.

[56] A. Y. Mutlu and S. Aviyente, "Multivariate Empirical Mode Decomposition for Quantifying Multivariate Phase Synchronization," *EURASIP J Adv Signal Process,* vol. 2011, p. 615717 2011.

[57] D. Rudrauf, A. Douiri, C. Kovach, J. P. Lachaux, D. Cosmelli, M. Chavez, *et al.*, "Frequency flows and the time-frequency dynamics of multivariate phase synchronization in brain signals," *Neuroimage,* vol. 31, pp. 209-227, 2006.

[58] W. Chaovalitwongse, P. M. Pardalos, P. Xanthopoulos, and A. R. Kammerdiner, "Analysis of Multi-channel EEG Recordings Based on Generalized Phase Synchronization and Cointegrated VAR," in *Computational Neuroscience*. vol. 38, ed: Springer New York, 2010, pp. 317-339.

[59] A. Omidvarnia, B. Boashash, G. Azemi, P. Colditz, and V. Vanhatalo, "Generalised phase synchrony within multivariate signals: an emerging concept in time-frequency analysis," presented at the IEEE Intl Conf Acoustics, Speech, Sig Process (ICASSP), Kyoto, Japan, 2012

[60] M. S. Khlif, M. Mesbah, B. Boashash, and P. Colditz, "Detection of neonatal seizure using multiple filters," presented at the Intl Conf Inform Sci Sig Process Applications (ISSPA), Kuala Lumpur, Malaysia, 2010.

[61] A. D. Bakhshi, M. A. Maud, K. M. Aamir, and A. Loan, "Cardiac arrhythmia detection using instantaneous frequency estimation of ECG signals," presented at the International Conference on Information and Emerging Technologies Karachi, Pakistan, 2010.

[62] Q. Lunji and L. Gang, "Representation of ECG signals based on the instantaneous frequency estimation," presented at the Int Conf Sig Process, Beijing , China 1996.

[63] I. Orovic, S. Stankovic, T. Thayaparan, and L. J. Stankovic, "Multiwindow S-method for instantaneous frequency estimation and its application in radar signal analysis," *IET Sig Process*, vol. 4, pp. 363-370, 2010.

[64] F. Berizzi and G. Pinelli, "Maximum-likelihood ISAR image autofocusing technique based on instantaneous frequency estimation," *IEE Proc Radar, Sonar Navigat*, vol. 144, pp. 284-292, 1997.

[65] L. Xue Mei, T. Ran, and L. Yan Lei, "SAR autofocus based on the instantaneous frequency estimation," presented at the Asian-Pacific Conf Synth Aperture Radar, China, 2009.

[66] S. S. Abeysekera, "Instantaneous frequency estimation from FM signals and its use in continuous phase modulation receivers," presented at the Intl Conf Inform, Communic Sig Process, Macau, 2009.

[67] Y. Jiexiao, L. Kai Hua, and L. Peng, "A mobile RFID localization algorithm based on instantaneous frequency estimation," presented at the Intl Conf Comp Sci Edu (ICCSE), Singapore 2011.

[68] W. J. Williams, "Reduced interference distributions: biological applications and interpretations," *Proc IEEE*, vol. 84, pp. 1264-1280, 1996.

[69] N. Stevenson, M. Mesbah, and B. Boashash, "Quadratic time-frequency distribution selection for seizure detection in the newborn," presented at the Conf Proc IEEE Eng Med Biol Soc (EMBS), Vancouver, BC 2008.

[70] B. Boashash and V. Sucic, "Resolution measure criteria for the objective assessment of the performance of quadratic time-frequency distributions," *IEEE Trans Sig Process*, vol. 51, pp. 1253-1263, 2003.

[71] B. Boashash, "Estimating and interpreting the instantaneous frequency of a signal. I. Fundamentals," *Proc IEEE*, vol. 80, pp. 520-538, 1992.

[72] B. Boashash, "Estimating and interpreting the instantaneous frequency of a signal. II. Algorithms and applications," *Proc IEEE*, vol. 80, pp. 540-568, 1992.

[73] B. Boashash, P. O'Shea, and M. J. Arnold, "Algorithms for instantaneous frequency estimation: a comparative study," presented at the SPIE Advanced Signal Processing Algorithms, Architectures, and Implementations, San Diego, CA, USA, 1990.

[74] L. Stankovic, "A multitime definition of the Wigner higher order distribution: L-Wigner distribution," *IEEE Signal Process Lett,* vol. 1, pp. 106-109, 1994.

[75] B. Boashash and P. O'Shea, "Polynomial Wigner-Ville distributions and their relationship to time-varying higher order spectra," *IEEE Trans Signal Process,* vol. 42, pp. 216-220, 1994.

[76] S. Stankovic, N. Zaric, and C. Ioana, "General form of time-frequency distribution with complex-lag argument," *Electron Lett,* vol. 44, pp. 699-701, 2008.

[77] S. Stankovic and L. Stankovic, "Introducing time-frequency distribution with a `complex-time' argument," *Electron Lett,* vol. 32, pp. 1265-1267, 1996.

[78] I. Orovic, M. Orlandic, S. Stankovic, and Z. Uskokovic, "A Virtual Instrument for Time-Frequency Analysis of Signals With Highly Nonstationary Instantaneous Frequency," *IEEE Trans Instrum Meas,* vol. 60, pp. 791-803, 2011.

[79] P. J. Kootsookos, B. C. Lovell, and B. Boashash, "A unified approach to the STFT, TFDs, and instantaneous frequency," *IEEE Trans Sig Process,* vol. 40, pp. 1971-1982, 1992.

[80] E. Zandi and G. Azemi, "Estimating the Scattering Distribution of the Received Signal in Micro-Cellular Systems," presented at the Euro Sig Process Conf (EUSIPCO), Lausanne, Switzerland, 2008.

[81] N. E. Huang and S. S. P. Shen, "Chapter 1: Introduction To The Hilbert Huang Transform And Its Related Mathematical Problems," in *Hilbert-Huang Transform And Its Applications*, ed: World Sci. Pub. Co., 2005, p. 324.

[82] L. Rankine, M. Mesbah, and B. Boashash, "IF estimation for multicomponent signals using image processing techniques in the time–frequency domain," *Sig Process,* vol. 87, pp. 1234-1250, 2007.

[83] J. Lerga, V. Sucic, and B. Boashash, "An Efficient Algorithm for Instantaneous Frequency Estimation of Nonstationary Multicomponent Signals in Low SNR," *EURASIP J Adv Signal Process,* vol. 2011, p. 725189, 2011.

[84] N. E. Huang, Z. Shen, S. R. Long, M. C. Wu, H. H. Shih, Q. Zheng, *et al.*, "The empirical mode decomposition and the Hilbert spectrum for nonlinear and non-stationary time series analysis," *Proc Royal Soc London, Series A: Math, Phys Eng Sci,* vol. 454, pp. 903-995, 1998.

[85] N. J. Stevenson, M. Mesbah, and B. Boashash, "Multiple-view time--frequency distribution based on the empirical mode decomposition," *IET Sig Process,* vol. 4, pp. 447-456, 2010.

[86] P. Flandrin, G. Rilling, and P. Goncalves, "Empirical mode decomposition as a filter bank," *IEEE Sig Process Lett,* vol. 11, pp. 112-114, 2004.

[87] M. P. Murray, "A Drunk and Her Dog: An Illustration of Cointegration and Error Correction," *Am Stat,* vol. 48, pp. 37-39, 1994.

[88] S. Johansen, "Estimation and Hypothesis Testing of Cointegration Vectors in Gaussian Vector Autoregressive Models," *Econometrica,* vol. 59, pp. 1551-1580, 1991.

[89] Z. N. Karam, "Computation of the One-Dimensional Unwrapped Phase," Master of Science in Electrical Engineering, Masters thesis, Massachusetts Institute of Technology, 2006.

[90] H. Hytti, R. Takalo, and H. Ihalainen, "Tutorial on Multivariate Autoregressive Modelling," *J Clin Monit Comput,* vol. 20, pp. 101-108, 2006.

[91] Marco D. Brockmann, B. Pöschel, N. Cichon, and Ileana L. Hanganu-Opatz, "Coupled Oscillations Mediate Directed Interactions between Prefrontal Cortex and Hippocampus of the Neonatal Rat," *Neuron,* vol. 71, pp. 332-347, 2011.

[92] S. H. Strogatz, "From Kuramoto to Crawford: exploring the onset of synchronization in populations of coupled oscillators," *Physica D,* vol. 143, pp. 1-20, 2000.

[93] E. Niedermeyer and F. Lopes da Silva, *Electroencephalography: Basic Principles, Clinical Applications, and Related Fields* 5th ed.: Lippincott Williams & Wilkins, 2004.

[94] J. Altenburg, R. J. Vermeulen, R. L. M. Strijers, W. P. F. Fetter, and C. J. Stam, "Seizure detection in the neonatal EEG with synchronization likelihood," *Clin Neurophysiol,* vol. 114, pp. 50-55, 2003.

[95] S. I. Dimitriadis, N. A. Laskaris, A. Tzelepi, and G. Economou, "Analyzing Functional Brain Connectivity by Means of Commute Times: A New Approach and its Application to Track Event-Related Dynamics," *IEEE Trans Biomed Eng,* vol. 59, pp. 1302-1309, 2012.

[96] S. Haufe, R. Tomioka, G. Nolte, K. R. Muller, and M. Kawanabe, "Modeling Sparse Connectivity Between Underlying Brain Sources for EEG/MEG," *IEEE Trans Biomed Eng,* vol. 57, pp. 1954-1963, 2010.

[97] H. Bin, Y. Lin, C. Wilke, and Y. Han, "Electrophysiological Imaging of Brain Activity and Connectivity:Challenges and Opportunities," *IEEE Trans Biomed Eng,* vol. 58, pp. 1918-1931, 2011.

[98] L. Faes, S. Erla, and G. Nollo, "Measuring Connectivity in Linear Multivariate Processes: Definitions, Interpretation, and Practical Analysis," *Comput Math Methods Med,* vol. 2012, p. 18, 2012.

[99] L. Faes and G. Nollo, "Extended causal modeling to assess Partial Directed Coherence in multiple time series with significant instantaneous interactions," *Biol Cybern,* vol. 103, pp. 387-400, 2010.

[100] W. Hesse, E. Möller, M. Arnold, and B. Schack, "The use of time-variant EEG Granger causality for inspecting directed interdependencies of neural assemblies," *J Neurosci Methods,* vol. 124, pp. 27-44, 2003.

[101] B. L. P. Cheung, R. Nowak, L. Hyong Chol, W. Drongelen, and B. D. Veen, "Cross Validation for Selection of Cortical Interaction Models From Scalp EEG or MEG," *IEEE Trans Biomed Eng,* vol. 59, pp. 504-514, 2012.

[102] G. G. Supp, A. Schlögl, N. Trujillo-Barreto, M. M. Müller, and T. Gruber, "Directed Cortical Information Flow during Human Object Recognition: Analyzing Induced EEG Gamma-Band Responses in Brain's Source Space," *PLoS ONE,* vol. 2, p. e684, 2007.

[103] S. Yu, Z. Hong, F. Ting, Q. Yihong, Z. Yisheng, and T. Shanbao, "Early Cortical Connective Network Relating to Audiovisual Stimulation by Partial Directed Coherence Analysis," *IEEE Trans Biomed Eng,* vol. 56, pp. 2721-2724, 2009.

[104] K. Lehnertz, "Assessing directed interactions from neurophysiological signals-an overview," *Physiol Meas,* vol. 32, p. 1715, 2011.

[105] D. Marinazzo, W. Liao, H. Chen, and S. Stramaglia, "Nonlinear connectivity by Granger causality," *Neuroimage,* vol. 58, pp. 330-338, 2010.

[106] L. Astolfi, F. Cincotti, D. Mattia, F. De Vico, A. Tocci, A. Colosimo, *et al.*, "Tracking the Time-Varying Cortical Connectivity Patterns by Adaptive Multivariate Estimators," *IEEE Trans Biomed Eng,* vol. 55, pp. 902-913, 2008.

[107] C. W. J. Granger, "Investigating Causal Relations by Econometric Models and Cross-spectral Methods," *Econometrica,* vol. 37, pp. 424-438, 1969.

[108] J. Geweke, "Measurement of Linear Dependence and Feedback Between Multiple Time Series," *J Am Stat Assoc,* vol. 77, pp. 304-313, 1982.

[109] L. A. Baccalá and K. Sameshima, "Partial directed coherence: a new concept in neural structure determination," *Biol Cybern,* vol. 84, pp. 463-474, 2001.

[110] M. Kaminski and K. Blinowska, "A new method of the description of the information flow in the brain structures," *Biol Cybern,* vol. 65, pp. 203-210, 1991.

[111] L. A. Baccalá and F. de Medicina, "Generalized Partial Directed Coherence," presented at the International Conference on Digital Signal Processing, Cardiff, UK, 2007.

[112] A. Korzeniewska, M. Manczak, M. Kaminski, K. J. Blinowska, and S. Kasicki, "Determination of information flow direction among brain structures by a modified directed transfer function (dDTF) method," *J Neurosci Methods,* vol. 125, pp. 195-207, 2003.

[113] M. Winterhalder, B. Schelter, W. Hesse, K. Schwab, L. Leistritz, D. Klan, *et al.*, "Comparison of linear signal processing techniques to infer directed interactions in multivariate neural systems," *Sig Process,* vol. 85, pp. 2137-2160, 2005.

[114] L. Sommerlade, K. Henschel, J. Wohlmuth, M. Jachan, F. Amtage, B. Hellwig, *et al.*, "Time-variant estimation of directed influences during Parkinsonian tremor," *J Physiol Paris,* vol. 103, pp. 348-352, 2009.

[115] F. He, H. L. Wei, S. A. Billings, and P. G. Sarrigiannis, "A nonlinear generalization of spectral Granger causality," *IEEE Trans Biomed Eng,* vol. 61, pp. 1693-701, Jun 2014.

[116] D. Marinazzo, M. Pellicoro, and S. Stramaglia, "Nonlinear parametric model for Granger causality of time series," *Phys Rev E Stat Nonlin Soft Matter Phys,* vol. 73, p. 066216, Jun 2006.

[117] L. Rankine, N. Stevenson, M. Mesbah, and B. Boashash, "A Nonstationary Model of Newborn EEG," *IEEE Trans Biomed Eng,* vol. 54, pp. 19-28, 2007.

[118] T. Chee-Ming, S. H. Salleh, Z. Z. Zainuddin, and A. Bahar, "Spectral Estimation of Nonstationary EEG Using Particle Filtering With Application to Event-Related Desynchronization (ERD)," *IEEE Trans Biomed Eng,* vol. 58, pp. 321-331, 2011.

[119] G. Nolte, O. Bai, L. Wheaton, Z. Mari, S. Vorbach, and M. Hallett, "Identifying true brain interaction from EEG data using the imaginary part of coherency," *Clin Neurophysiol,* vol. 115, pp. 2292-2307, 2004.

[120] G. Gomez-Herrero, "Brain Connectivity Analysis with EEG," PhD, Doctoral dissertation, Tampere University of Technology, Finland, 2010.

[121] M. J. Brookes, M. Woolrich, H. Luckhoo, D. Price, J. R. Hale, M. C. Stephenson, *et al.*, "Investigating the electrophysiological basis of resting state networks using magnetoencephalography," *Proc Natl Acad Sci U S A,* vol. 108, pp. 16783-8, 2011.

[122] J. M. Palva, S. Monto, S. Kulashekhar, and S. Palva, "Neuronal synchrony reveals working memory networks and predicts individual memory capacity," *Proc Natl Acad Sci U S A,* vol. 107, pp. 7580-7585, 2010.

[123] J. F. Hipp, D. J. Hawellek, M. Corbetta, M. Siegel, and A. K. Engel, "Large-scale cortical correlation structure of spontaneous oscillatory activity," *Nat Neurosci.,* vol. 15, pp. 884-890, 2012.

[124] A. Neumaier and T. Schneider, "Estimation of parameters and eigenmodes of multivariate autoregressive models," *ACM Trans Math Softw,* vol. 27, pp. 27-57, 2001.

[125] A. B. Koehler and E. S. Murphree, "A Comparison of the Akaike and Schwarz Criteria for Selecting Model Order," *Appl. Statist.,* vol. 37, pp. 187-195, 1988.

[126] P. L. Nunez and R. Srinivasan, *Electric Fields of the Brain: The neurophysics of EEG*. New York: Oxford University Press, 2006.

[127] J. L. Rodgers, W. A. Nicewander, and L. Toothaker, "Linearly Independent, Orthogonal, and Uncorrelated Variables," *Am Stat,* vol. 38, pp. 133-134, 1984.

[128] A. Tokariev, K. Palmu, A. Lano, M. Metsäranta, and S. Vanhatalo, "Phase synchrony in the early preterm EEG: Development of methods for estimating synchrony in both oscillations and events," *Neuroimage,* vol. 60, pp. 1562-1573, 2012.

[129] A. Omidvarnia, G. Azemi, B. Boashash, J. O. Toole, P. Colditz, and S. Vanhatalo, "Orthogonalized Partial Directed Coherence for Functional Connectivity Analysis of Newborn EEG," presented at the Int Conf Neural Info Process (ICONIP), Doha, Qatar, 2012.

[130] S. Stjerna, J. Voipio, M. Metsäranta, K. Kaila, and S. Vanhatalo, "Preterm EEG: A Multimodal Neurophysiological Protocol," *J Vis Exp,* 2012.

[131] A. Delorme and S. Makeig, "EEGLAB: an open source toolbox for analysis of single-trial EEG dynamics," *J Neurosci Methods,* vol. 134, pp. 9-21, 2004.

[132] M. Boersma, D. J. A. Smit, H. M. A. de Bie, G. C. M. Van Baal, D. I. Boomsma, E. J. C. de Geus, *et al.*, "Network analysis of resting state EEG in the developing young brain: Structure comes with maturation," *Hum Brain Mapp,* vol. 32, pp. 413-425, 2011.

[133] S. Palva, K. Linkenkaer-Hansen, R. Näätänen, and J. M. Palva, "Early Neural Correlates of Conscious Somatosensory Perception," *J Neurosci,* vol. 25, pp. 5248-5258, 2005.

[134] E. A. Wan and A. T. Nelson, "Dual Extended Kalman Filter Methods," in *Kalman Filtering and Neural Networks,* ed: John Wiley & Sons, Inc., 2002, pp. 123-173.

[135] J. Dauwels, K. Srinivasan, M. Ramasubba Reddy, T. Musha, F.-B. Vialatte, C. Latchoumane, *et al.*, "Slowing and Loss of Complexity in Alzheimer's EEG: Two Sides of the Same Coin?," *Int J Alzheimers Dis,* vol. 2011, 2011.

[136] B. He, Y. Dai, L. Astolfi, F. Babiloni, H. Yuan, and L. Yang, "eConnectome: A MATLAB toolbox for mapping and imaging of brain functional connectivity," *J Neurosci Methods,* vol. 195, pp. 261-269, 2011.

[137] L. Faes, A. Porta, and G. Nollo, "Testing Frequency-Domain Causality in Multivariate Time Series," *IEEE Trans Biomed Eng,* vol. 57, pp. 1897-1906, 2010.

[138] D. Yasumasa Takahashi, L. Antonio Baccal, and K. Sameshima, "Connectivity Inference between Neural Structures via Partial Directed Coherence," *J Appl Stat,* vol. 34, pp. 1259-1273, 2007.

[139] S. Haufe, V. V. Nikulin, K.-R. Müller, and G. Nolte, "A critical assessment of connectivity measures for EEG data: A simulation study," *Neuroimage,* vol. 64, pp. 120-133, 2013.

[140] Z. Yan and X. Gao, "Functional connectivity analysis of steady-state visual evoked potentials," *Neurosci Lett,* vol. 499, pp. 199-203, 2011.

[141] R. Srinivasan, E. Fornari, M. Knyazeva, R. Meuli, and P. Maeder, "fMRI responses in medial frontal cortex that depend on the temporal frequency of visual input," *Exp Brain Res,* vol. 180, pp. 677-691, 2007.

[142] G. R. Burkitt, R. B. Silberstein, P. J. Cadusch, and A. W. Wood, "Steady-state visual evoked potentials and travelling waves," *Clin Neurophysiol,* vol. 111, pp. 246-258, 2000.

[143] P. L. Nunez, "Implications of white matter correlates of EEG standing and traveling waves," *Neuroimage,* vol. 57, pp. 1293-1299, 2010.

[144] M. Thoresen, L. Hellström-Westas, X. Liu, and L. S. de Vries, "Effect of Hypothermia on Amplitude-Integrated Electroencephalogram in Infants With Asphyxia," *Pediatrics,* vol. 126, pp. 131-139, 2010.

[145] T. Kontio, M. C. Toet, L. Hellström-Westas, M. van Handel, F. Groenendaal, S. Stjerna, *et al.*, "Early neurophysiology and MRI in predicting neurological outcome at 9–10 years after birth asphyxia," *Clin Neurophysiol,* vol. 124, pp. 1089-94, 2013.

[146] N. K. Logothetis, "What we can do and what we cannot do with fMRI," *Nature,* vol. 453, pp. 869-878, 2008.

[147] D. Mantini, M. G. Perrucci, C. D. Gratta, G. L. Romani, and M. Corbetta, "Electrophysiological signatures of resting state networks in the human brain," *Proc Natl Acad Sci U S A,* vol. 104, pp. 13170-13175, 2007.

[148] F. d. Pasquale, S. D. Penna, A. Z. Snyder, C. Lewis, D. Mantini, L. Marzetti, *et al.*, "Temporal dynamics of spontaneous MEG activity in brain networks," *Proc Natl Acad Sci U S A,* vol. 107, pp. 6040-6045, 2010.

[149] P. Fransson, B. Skiöld, M. Engström, B. Hallberg, M. Mosskin, U. Aden, *et al.*, "Spontaneous brain activity in the newborn brain during natural sleep--an fMRI study in infants born at full term," *Pediatr Res,* vol. 66, pp. 301-305, 2009.

[150] L. Myers and M. J. Sirois, "Spearman Correlation Coefficients, Differences between," in *Encyclopedia of Statistical Sciences*, ed: John Wiley & Sons, Inc., 2004.

[151] F. Perrin, J. Pernier, O. Bertrand, and J. F. Echallier, "Spherical splines for scalp potential and current density mapping," *Electroencephalogr Clin Neurophysiol,* vol. 72, pp. 184-187, 1989.

[152] M. Odabaee, W. J. Freeman, P. B. Colditz, C. Ramon, and S. Vanhatalo, "Spatial patterning of the neonatal EEG suggests a need for a high number of electrodes," *Neuroimage,* vol. 68, pp. 229-235, 2013.

[153] J. Kayser and C. E. Tenke, "Principal components analysis of Laplacian waveforms as a generic method for identifying ERP generator patterns: I. Evaluation with auditory oddball tasks," *Clin Neurophysiol,* vol. 117, pp. 348-368, 2006.

[154] A. Delorme and S. Makeig, "EEGLAB: an open source toolbox for analysis of single-trial EEG dynamics including independent component analysis," *J Neurosci Methods,* vol. 134, pp. 9-21, 2004.

[155] K. R. A. V. Dijk, T. Hedden, A. Venkataraman, K. C. Evans, S. W. Lazar, and R. L. Buckner, "Intrinsic Functional Connectivity As a Tool For Human Connectomics: Theory, Properties, and Optimization," *J Neurophysiol,* vol. 103, pp. 297-321, 2010.

[156] S. Vanhatalo and L. Lauronen, "Neonatal SEP – Back to bedside with basic science," *Semin Fetal Neonatal Med,* vol. 11, pp. 464-470, 2006.

[157] C. J. Stam, W. d. Haan, A. Daffertshofer, B. F. Jones, I. Manshanden, A. M. v. C. v. Walsum, *et al.*, "Graph theoretical analysis of magnetoencephalographic functional connectivity in Alzheimer's disease," *Brain,* vol. 132, pp. 213-224, 2009.

[158] C. J. Stam and E. C. W. van Straaten, "The organization of physiological brain networks," *Clin Neurophysiol,* vol. 123, pp. 1067-1087, 2012.

[159] E. Bullmore and O. Sporns, "Complex brain networks: graph theoretical analysis of structural and functional systems," *Nat Rev Neurosci,* vol. 10, pp. 186-198, 2009.

[160] M. Boersma, C. Kemner, M. De Reus, G. Collin, T. Snijders, D. Hofman, *et al.*, "Disrupted functional brain networks in autistic toddlers," *Brain Connect,* vol. 3, pp. 41-49, 2013.

[161] D. J. A. Smit, M. Boersma, H. G. Schnack, S. Micheloyannis, D. I. Boomsma, H. E. Hulshoff Pol, *et al.*, "The Brain Matures with Stronger Functional Connectivity and Decreased Randomness of Its Network," *PLoS ONE,* vol. 7, p. e36896, 2012.

[162] V. Tsiaras, P. G. Simos, R. Rezaie, B. R. Sheth, E. Garyfallidis, E. M. Castillo, *et al.*, "Extracting biomarkers of autism from MEG resting-state functional connectivity networks," *Comput Biol Med,* vol. 41, pp. 1166-1177, 2011.

[163] M. Rubinov and O. Sporns, "Complex network measures of brain connectivity: uses and interpretations," *Neuroimage,* vol. 52, pp. 1059-1069, 2010.

[164] I. Kostović, N. Jovanov-Milošević, M. Radoš, G. Sedmak, V. Benjak, M. Kostović-Srzentić, *et al.*, "Perinatal and early postnatal reorganization of the subplate and related cellular compartments in the human cerebral wall as revealed by histological and MRI approaches," *Brain Struct Funct,* [Epub ahead of print] 2012.

[165] M. E. J. Newman, "Finding community structure in networks using the eigenvectors of matrices," *Phys Rev E*, vol. 74, p. 036104, 2006.

[166] J. C. Sprott, *Chaos and Time-Series Analysis*: Oxford University Press 2003.

[167] N. Mantel, "The Detection of Disease Clustering and a Generalized Regression Approach," *Cancer Res*, vol. 27, pp. 209-220, 1967.

[168] M.-J. Fortin, M. R. T. Dale, and J. ver Hoef, "Spatial analysis in ecology," in *Encyclopedia of Environmetrics*. vol. 4, A. El-Shaarawi and W. Piegorsch, Eds., ed Chichester: John Wiley and Sons, 2002, pp. 2051–2058.

[169] A. Papoulis and S. U. Pillai, *Probability, Random Variables And Stochastic Processes*: McGraw-Hill Education (India) Pvt Limited, 2002.

[170] I. Kostović and M. Judas, "The development of the subplate and thalamocortical connections in the human foetal brain," *Acta Paediatr*, vol. 99, pp. 1119-1127, 2010.

[171] M. André, M. D. Lamblin, A. M. d'Allest, L. Curzi-Dascalova, F. Moussalli-Salefranque, T. S Nguyen The, *et al.*, "Electroencephalography in premature and full-term infants. Developmental features and glossary," *Clin Neurophysiol*, vol. 40, pp. 59-124, 2010.

[172] M. Tolonen, J. M. Palva, S. Andersson, and S. Vanhatalo, "Development of the spontaneous activity transients and ongoing cortical activity in human preterm babies," *j Neurosci*, vol. 145, pp. 997-1006, 2007.

[173] Q. K. Telesford, S. L. Simpson, J. H. Burdette, S. Hayasaka, and P. J. Laurienti, "The brain as a complex system: using network science as a tool for understanding the brain," *Brain Connect*, vol. 1, pp. 295-308, 2011.

[174] E. Hjalmarsson and P. Osterholm, "Testing for cointegration using the Johansen methodology when variables are near-integrated," Intl. Monetary Fund, Western Hemisphere Division2007.

[175] J. P. LeSage, "Econometrics Toolbox," *MATLAB functions, available at: http://www.spatial-econometrics.com*.

Appendix A: Empirical Mode Decomposition (EMD)

We used the following procedure to derive the EMD process [56, 81, 84] in this study:

1. Let $\tilde{s}[n] = r_i[n], r_1[n] = s[n], i = 1,2,3, ...$

2. Identify all the local maxima and minima of $\tilde{s}[n]$.

3. Connect all the local maxima together and all the local minima together by an interpolation method (e.g., spline) to obtain the upper envelope $e_{max}[n]$ and the lower envelope $e_{min}[n]$.

4. Update $\tilde{s}[n]$ as $\tilde{s}[n] = \tilde{s}[n] - 0.5(e_{min}[n] + e_{max}[n])$ and go to step 2.

5. Repeat steps 2-4 until a stoppage criterion is satisfied. s̃[n] will then become an IMF.

6. Separate the IMF $h[n]$ from the rest of the data by $r_{i+1}[n] = s[n] - \tilde{s}[n]$. The residue $r_{i+1}[n]$ is then treated as the updated signal $s[n]$ and fed into the sifting process again (steps 1-5).

The process is repeated until no more IMFs can be extracted, in other words, the residue becomes a monotonic function. Other predetermined criteria such as thresholding on the energy of the residue can also be used [81].

Appendix B: Multivariate Johansen test

The Johansen test is a procedure for testing the cointegrating relationships of several integrated processes of order zero or one [44]. Since the test evaluates more than one cointegrating relationship within the time series, it is applicable for multivariate signals such as multichannel EEG. The starting point of the test in this study is from an N-dimensional IF $f_z[n] \in \mathbb{R}^{N\times 1}$as an multivariate MVAR model of order p given by [58, 174]:

$$f_z[n] = \mu + \sum_{r=1}^{p} A_r f_z[n-r] + \varepsilon[n] \tag{B.1}$$

where $A_r \in \mathbb{R}^{N\times N}$ is the MVAR coefficient matrix at delay r, $\varepsilon[n] \in \mathbb{R}^{N\times 1}$ is the input white noise of the model and $\mu \in \mathbb{R}^{N\times 1}$ is a constant term. The assumption here is that the variables of $f_z[n]$ are integrated processes of either order one ($I(1)$) or order zero ($I(0)$ or a stationary process). The MVAR model described in (B.1) can be re-written in terms of the differences between its successive delayed values as:

$$\Delta f_z[n] = -\Pi f_z[n-1] + \sum_{r=1}^{p-1} \Gamma_r \Delta f_z[n-r] + \varepsilon[n] \tag{B.2}$$

where

$$\Pi = I - A_1 - \cdots - A_p \tag{B.3}$$

$$\Gamma_r = -\sum_{j=r+1}^{p} A_j \tag{B.4}$$

and $\Delta f_z[n-i] = f_z[n-i] - f_z[n-i-1]$ [58, 174]. Such transformed version of the MVAR models is called *Vector error correlation model* (*VECM*). If r is the rank of the coefficient matrix Π ($r < N$), then there exist two full-rank matrices α and β ($\alpha, \beta \in \mathbb{R}^{r\times N}$) such that $\beta^T f_z(n)$ is stationary and $\Pi = \alpha\beta^T$. The rank r determines the number of coefficient relationships between the dimensions of $f_z[n]$. Cointergarting vectors of the process are also obtained from the columns of β. Based on the maximum likelihood estimation of β for a given r, the Johansen method performs two different likelihood ratio tests: *the trace test* and *the maximum eigenvalue test*. The former one tests a hypothesis $\boldsymbol{H_0}$ against an alternative $\boldsymbol{H_1}$, where

$\boldsymbol{H_0}$: $there\ are\ r\ cointegrating\ relationships\ between\ variables,$

$\boldsymbol{H_1}$: $there\ are\ k\ cointegrating\ relationships\ between\ variables.$

For the latter one, the null and alternative hypotheses are defined as:

$\boldsymbol{H_0}$: $there\ are\ r\ cointegrating\ relationships\ between\ variables,$

$\boldsymbol{H_1}$: $there\ are\ r+1\ cointegrating\ relationships\ between\ variables.$

In the special case of $r = N$ (Π has full-rank), all variables of the process are stationary and there is no conintegrating relationship between them [174]. In this study, the MATLAB implementation of the multivariate Johansen test provided in the Econometrics toolbox [175] was used.